Master's thesis

2024

Torbjørn Bogen-Storø

NTNU
Norwegian University of
Science and Technology
Faculty of Natural Sciences
Department of Physics

Torbjørn Bogen-Storø

Design, Manufacturing and Mueller Matrix extracting FDTD Simulations of Polarimetric Beam-Splitting Metasurfaces

February 2024

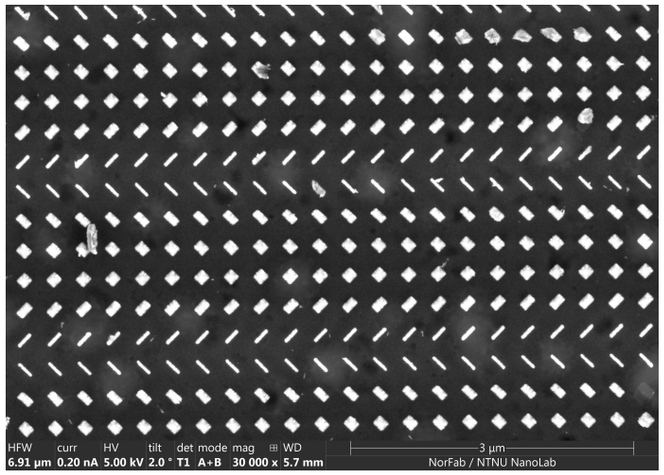

NTNU
Norwegian University of
Science and Technology

NTNU
Norwegian University of
Science and Technology

NTNU

Norwegian University of
Science and Technology

Design, Manufacturing and Mueller Matrix extracting FDTD Simulations of Polarimetric Beam-Splitting Metasurfaces

Torbjørn Bogen-Storø

Nanotechnology
Submission date: February 2024
Supervisor: Professor Morten Kildemo

Norwegian University of Science and Technology
Department of Physics

NTNU
Kunnskap for en bedre verden

Department of Physics

Design and Manufacturing of Polarization Beam-Splitting Metasurfaces, and FDTD Simulations of their Mueller Matrices

Author: Torbjørn Bogen-Storø

Supervisor: Professor Morten Kildemo

February, 2024

Abstract

This thesis investigates the design, fabrication, and Finite-Difference Time-Domain (FDTD) simulations of optical metasurfaces, with an emphasis on polarization beam splitting metasurfaces. The study primarily focuses on two types of metasurfaces: Gap Surface Plasmon (GSP) metasurfaces aimed at achieving a greater angle of refraction than previous work, and amorphous silicon (a-Si) pillar-based metasurfaces with an integrated aperture for camera integration.

The fabrication process of GSP metasurfaces was executed, despite some missing meta-atoms likely due to an incorrect ratio between resist and metallic layer thickness in the lift-off process. The design and preliminary stages of the a-Si pillar metasurfaces were completed, although full fabrication was not achieved due to time and equipment constraints. The integration of an aperture into the metasurface design was initiated and characterized with intensity measurements, indicating the necessity for further fine-tuning of process characteristics.

In addition to manufacturing, a methodology for extracting Mueller Matrices in FDTD simulations was developed and successfully implemented, providing a promising basis for further refinement. This approach is particularly beneficial for large, non-periodic metasurfaces, where FDTD offers advantages over Finite Element Method (FEM).

Sammendrag

Denne avhandlingen undersøker design, fabrikasjon og Finite-Difference Time-Domain (FDTD) simuleringer av optiske metasurfacer, med vekt på polarisasjon -splittende metasurfacer. Avhandlingen fokuserer hovedsakelig på to typer metasurfaces: Gap Surface Plasmon (GSP) metasurfacer rettet mot å oppnå en større brytningsvinkel, og amorfe silisium (a-Si) søylebaserte metasurfaces med en integrert blenderåpning.

Fabrikasjonsprosessen for GSP metasurfaces ble gjennomført, til tross for noen manglende meta-atomer, sannsynligvis på grunn av et feil forhold mellom resist og metallisk lagtykkelse i lift-off prosessen. Design og innledende stadier av a-Si søyle metasurfaces ble fullført, selv om full fabrikasjon ikke ble oppnådd på grunn av tid og utstyrsbegrensninger. Integreringen av en aperture i metasurface-designet ble igangsatt og karakterisert, noe som indikerer nødvendigheten av videre undersøkelse.

I tillegg til produksjon, ble en metode for å trekke ut Mueller Matrices i FDTD-simuleringer utvikley, noe som gir et lovende grunnlag for videre bruk. Denne tilnærmingen er spesielt gunstig for store, ikke-periodiske metasurfaces, der FDTD tilbyr fordeler over Finite Element Method (FEM).

Preface and Acknowledgements

I want to express my sincere thanks to my supervisor, Professor Morten Kildemo, for his unwavering support and guidance throughout the process of writing this thesis. Your mentorship and dedication to my project have been truly remarkable. I'm grateful for the opportunity to work on this exciting project. Your passion for the topics of optics and metasurfaces was contagious and pushed me to explore these areas in depth. I appreciate the extra time you spent helping me, often outside of regular hours, with measurements, simulations and discussions. I want to thank you for our insightful discussions and the valuable feedback you provided. Your constructive criticism and expert insights have greatly improved the quality of this thesis. This work would not have been possible without your support.

In addition, I extend my thanks to PhD candidates Nathan Hale and Victoria Bjelland, who have been instrumental in helping me understand and enhance my FDTD simulation results. I also appreciate the assistance of PhD candidates Ida Breivik and Marthe Linnerud. Ida's guidance in mastering Beamer was invaluable, and Marthe's help with measurements and obtaining high-quality SEM images in the NanoLab was uttermost helpful.

I am also grateful to the engineers at NTNU NanoLab. Their instruction in using various instruments and tools at NanoLab, along with their willingness to discuss process parameters, significantly contributed to my work.

Special thanks to Professor Ingve Simonsen for setting up the HP computer with Debian Linux and Lumerical, which was fundamental for the simulations in this thesis.

Finally, I want to express my deepest gratitude to my family for their constant encouragement and support throughout my education. A special mention to my late grandfather, Jon Bogen, whose passion for science has been a major inspiration in my pursuit of this field.

Contents

List of Figures

List of Tables

Introduction

Light, the fundamental element that illuminates our world, plays an instrumental role in gathering information about our surroundings. It is the critical component behind the operation of numerous devices, from simple mirrors to complex camera sensors. In recent years, the manipulation of light through metasurfaces has opened up new possibilities in various fields, including optics, telecommunications, and even invisibility cloaks.[1][2][3]

Metasurfaces, ultra-thin films structured at a sub-wavelength scale, have the ability to manipulate the phase, amplitude, and polarization of light. Previous research conducted at the Norwegian University of Science and Technology (NTNU), led by Professor Morten Kildemo, has delved into the design and characterization of such metasurfaces. Two examples of this are amorphous silicon (a-Si) based polarimetric beam-splitting metasurfaces operating in transmission[4] and gap-surface plasmon (GSP) based polarimetric beam-splitting metasurfaces operating in reflection[5]. The primary objective of these studies was to evaluate the quality of the metasurface and characterize the manufacturing process.

Both these metasurfaces ended up with a slight deviation from the designed structure. The a-Si pillars were manufactured with a slight conical shape, due to the etch process, while the GSP metasurface was manufactured with a SiO2 layer of 100 nm, in contrast to the designed 50 nm.

This thesis aims to build upon these previous studies and improve the design and manufacturing process of metasurfaces to enhance their integrability with devices such as sensors and camera chips. A significant part of this refinement process involves integrating the metasurface design with a camera chip. This presents a challenge for the a-Si pillar metasurface, as the illumination area considerably exceeds the metasurface area, leading to potential interference from "unaffected" light. To address this issue, the integration of an aperture into the existing design was proposed, necessitating further process characterization. As for the GSP, the integrability with a sensor is enhanced by a greater angle of refraction, such that the two polarisation states are reflected to a distance further away from the source

However, the research faced several challenges primarily related to the accessibility of necessary

manufacturing and analysis equipment. This led to a shift in focus towards the investigation of the GSP metasurfaces. The metasurfaces were redesigned to achieve a greater angle of reflection and correct the error in the thickness of the SiO2 layer.

Additionally, this thesis explores the implementation of Mueller Matrix calculation and extraction from Finite-Difference Time-Domain (FDTD) simulation software ANSYS. Compared to FEM simulations, FDTD scales better for memory intensive calculation. Thus, in order to simulate larger super-period such as for beam splitting polarising lenses, implementation of a function that extracts the Mueller Matrix in FDTD is an important step.

Despite the challenges faced, this thesis aims to make progress in the design and manufacturing of optical beam splitting metasurfaces, both by developing processes in the nano fabrication and by implementing a tool for simulating Mueller Matrices in FDTD.

Theory

2.1 Optics

2.1.1 Basic Principles of Light

Light is a fundamental entity among the natural forces, and is essential in natural sciences and the understanding of our universe. Light exhibits the wave-particle duality, as photons and electromagnetic waves respectively. To understand the fundamental properties and behavior of light, Maxwell's equations is the best starting point. Formulated by James Clark Maxwell in the 19th century, this set of four equations describe the interaction between electrical and magnetic fields, charges and currents. In their time dependent differential form, they are [6]:

Gauss law for electricity, which describes how an Electric field arises from a charge:

$$\nabla \cdot \mathbf{D}(\mathbf{r}, t) = \rho(\mathbf{r}, t) \tag{2.1}$$

Gauss law for magnetism, which describes that a magnetic field cannot arise from a single point (No magnetic monopole)

$$\nabla \cdot \mathbf{B}(\mathbf{r}, t) = 0 \tag{2.2}$$

Faraday's law of induction, which describes the an electric field arises from a temporal change in the magnetic field:

$$\nabla \times \mathbf{E}(\mathbf{r}, t) = -\frac{\partial \mathbf{B}(\mathbf{r}, t)}{\partial t} \tag{2.3}$$

Amperes circuital law with Maxwell addition, which describes the a magnetic field arises from a temporal change in the electric field, or a current:

$$\nabla \times \mathbf{H}(\mathbf{r}, t) = \mathbf{j}(\mathbf{r}, t) + \frac{\partial \mathbf{D}(\mathbf{r}, t)}{\partial t} \tag{2.4}$$

In these equations, the variables represent the following:

- $\mathbf{E}(\mathbf{r}, t)$: the electric field, a vector quantity that describes the electric force per unit charge experienced by a stationary charged particle.

- $\mathbf{D}(\mathbf{r}, t)$: the dielectric field, which describes the amount of electric field due to free charges. It is related to the electric field $\mathbf{E}(\mathbf{r}, t)$ by

$$\mathbf{D} = \varepsilon_0 \mathbf{E}(\mathbf{r}, t) + \mathbf{P}(\mathbf{r}, t) \tag{2.5}$$

  , where $\mathbf{P}(\mathbf{r}, t)$ is the macroscopic polarization of the medium in question.

- ρ: the electric charge density, which is the amount of charge per unit volume.

- $\mathbf{H}(\mathbf{r}, t)$: the magnetic field, a vector quantity that describes the magnetic force experienced by a moving charged particle.

- $\mathbf{B}(\mathbf{r}, t)$: the magnetic induction. It is related to the magnetic field $\mathbf{H}(\mathbf{r}, t)$ by

$$\mathbf{H}(\mathbf{r}, t) = \frac{1}{\mu_0}\mathbf{B}(\mathbf{r}, t) - \mathbf{M}(\mathbf{r}, t) \tag{2.6}$$

  , where $\mathbf{M}(\mathbf{r}, \mathbf{t})$ is the magnetization.

- $\mathbf{j}(\mathbf{r}, t)$: the current density, which is the amount of electric current per unit area.

Constitutive relations

In order to describe how the currents and charges are related to the electric and magnetic field, we need to introduce these material equations known as the constitutive relations [6]:

$$\mathbf{D} = \epsilon_0 \epsilon \mathbf{E} \qquad (\mathbf{P} = \epsilon_0 \chi_e \mathbf{E}) \tag{2.7}$$

$$\mathbf{B} = \mu_0 \mu \mathbf{H} \qquad (\mathbf{M} = \chi_m \mathbf{H}) \tag{2.8}$$

$$\mathbf{j_c} = \sigma \mathbf{E} \tag{2.9}$$

Here, the parameters χ_e and χ_m are introduced, as the electric and magnetic susceptibility, respectively. These relations account for inhomogeneous media, if the material parameters ϵ, μ and σ are spatially dependent. The medium is named temporal dispersive if the material parameters are functions of frequency, and spatially dispersive if the constitutive relations are convolutions over space [6]. In order to evaluate the time dependent displacement field $\mathbf{D}(\mathbf{r}, \mathbf{t})$, we first express the temporally dispersive displacement field

$$\mathbf{D}(\mathbf{k}, \omega) = \epsilon_0 \epsilon(\mathbf{k}, \omega) \mathbf{E}(\mathbf{k}, \omega) \tag{2.10}$$

$\mathbf{E}(\mathbf{k}, \omega)$ is the equivalent of the Fourier transform of a time dependent field $\mathbf{E}(\mathbf{r}, t)$, thus by applying the inverse Fourier transform to equation 2.10 we can express the relation between the displacement field $\mathbf{D}(\mathbf{r}, t)$ and the electric field $\mathbf{E}(\mathbf{r}, t)$ as [6]:

$$D(\mathbf{r}, t) = \int \int \tilde{\epsilon}(\mathbf{r}' - \mathbf{r}, t - t') E(, \mathbf{r}', t') d\mathbf{r}' dt' \tag{2.11}$$

Equation 2.11 describes that the displacement field at time t is dependent on the electric field at all times t' previous to t. Also, the displacement at location $\mathbf{r}$ is dependent on the neighboring points$\mathbf{r}'$. In most cases of interest, the spatial dispersion can be neglected, however the temporal dispersion is essential to accurately take into account[6].

A similar relation is valid for the magnetic field and the magnetic field strength, however since this thesis does not include magnetic materials, this is not further discussed.

The Wave Equation

The wave equation can be derived from the Maxwell equations, by combining Faraday's law and Amperes law, also using equation 2.5 and 2.6. To combine them, we first take the curl on each side of Faraday's law.

$$\nabla \times \nabla \times \mathbf{E} + \frac{1}{c^2}\frac{\partial^2 \mathbf{E}}{\partial t^2} = -\mu_0 \frac{\partial}{\partial t}(\mathbf{j} + \frac{\partial \mathbf{P}}{\partial t} + \nabla \times \mathbf{M}) \tag{2.12}$$

Here, the constant c is introduced as $c = \frac{1}{\sqrt{\epsilon_0 \mu_0}}$. The bracket on right hand side is simplified by introducing the total current density

$$\mathbf{j_t} = \mathbf{j_s} + \mathbf{j_c} + \frac{\partial \mathbf{P}}{\partial t} + \nabla \times \mathbf{M} \tag{2.13}$$

, where the four terms represent the source current density, the induced conduction current density, the polarization current density and the magnetisation current density respectively[6].

As the time dependency of the electric field can prove challenging in formulations, we can express the Maxwell equations in the spectral representation, where the relation between the time-dependent field $\mathbf{E}(\mathbf{r}, t)$ and the spectrum $\hat{\mathbf{E}}(\mathbf{r}, \omega)$:

$$\hat{\mathbf{E}}(\mathbf{r}, \omega) = \frac{1}{2\pi}\int_{-\infty}^{\infty} \mathbf{E}(\mathbf{r}, t) e^{i\omega t} dt \tag{2.14}$$

The Maxwell equations 2.1 to 2.3 then becomes:

$$\nabla \times \hat{\mathbf{E}}(\mathbf{r}, \omega) = i\omega \hat{\mathbf{B}}(\mathbf{r}, \omega) \tag{2.15}$$

$$\nabla \times \hat{\mathbf{H}}(\mathbf{r}, \omega) = -i\omega \hat{\mathbf{D}}(\mathbf{r}, \omega) + \hat{\mathbf{j}}(\mathbf{r}, \omega) \tag{2.16}$$

$$\nabla \cdot \hat{\mathbf{D}}(\mathbf{r}, \omega) = \hat{\rho}(\mathbf{r}, \omega) \tag{2.17}$$

$$\nabla \cdot \hat{\mathbf{B}}(\mathbf{r}, \omega) = 0 \tag{2.18}$$

By combining equation 2.15 and 2.16, we can again isolate the electric field dependency to

$$\nabla \times \mu^{-1} \nabla \times \mathbf{E} - \frac{\omega^2}{c^2}[\epsilon + i\omega/(\omega\epsilon_0)]\mathbf{E} = i\omega\mu_0 \mathbf{j}_s \tag{2.19}$$

Here, the expression in brackets is commonly replaced with the complex dielectric constant, $[\epsilon + i\omega/(\omega\epsilon_0)] = \epsilon$

$$\nabla \times \mu^{-1} \nabla \times \mathbf{E} - k_0^2 \epsilon \mathbf{E} = i\omega\mu_0 \mathbf{j}_s \tag{2.20}$$

with solution

$$(\nabla^2 + k^2)\mathbf{E} = -i\omega\mu_0\mu\mathbf{j} + \frac{\nabla\rho}{\epsilon_0\epsilon} \tag{2.21}$$

In free space, there are no free currents $\mathbf{j}$, and no charge densities ρ, such that equation 2.21 becomes

$$\nabla^2\mathbf{E} + k^2\mathbf{E} = 0 \tag{2.22}$$

where $k = \frac{\omega}{c}\sqrt{\mu\epsilon}$, with solution

$$\mathbf{E} = \mathbf{E}_0 e^{i(\mathbf{k}z - \omega t + \phi)} \tag{2.23}$$

This equation describes a wave propagating in time and space, and is given by a complex exponential, where the distance travelled by the wave is related to the wave vector $\mathbf{k}$, and the oscillation in time is described by the angular frequency ω. This equation is complex, meaning it has both a real and an imaginary part. The real part of this solution corresponds to the physical electric or magnetic field that we can measure, whereas the imaginary part is more of a mathematical construct that captures the wave's oscillatory behavior and propagation characteristics.

The phase shift ϕ describes the point in the oscillation where the wave begins at $t = 0$. It provides information about how the wave is shifted in space or time relative to some reference point. This phase shift is important when considering such as in diffraction and interference.

The wave vector $\mathbf{k}$ and the angular frequency ω are related to the phase velocity v_p of the wave. The phase velocity is defined as the rate at which the phase of the wave propagates in space, and it can be calculated by the equation $v_p = \frac{\omega}{|\mathbf{k}|}$.

2.1.2 Polarization Optics

Two waves with identical wavelength and irradiance, but different direction of their electric field, can behave differently[7]. This is explained by the introduction of polarization. Considering a wave that propagates in the z direction, we can decompose the electric field into two orthogonal directions, E_x and E_y. The expression of these two components then becomes[7]:

$$E_x = |E_x|e^{i(kz - \omega t + \delta_x)} \quad E_y = |E_y|e^{i(kz - \omega t + \delta_y)} \tag{2.24}$$

where δ_x and δ_y are the phases for the two components. The polarization-state is described by the difference in phase and the relative amplitude between the two orthogonal components.

In polarization optics, six basic polarization states are mainly discussed, as all other states can be constructed as a superposition of these states: linearly polarized light along x and y, linearly

polarized light along ±45 degrees and circular polarized light left handed and right handed. These are shown in figure 2.1

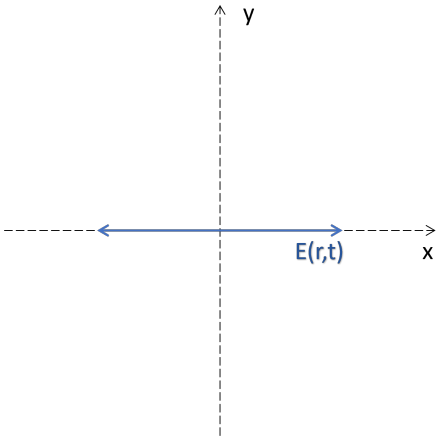

(a) x-linearly polarized light

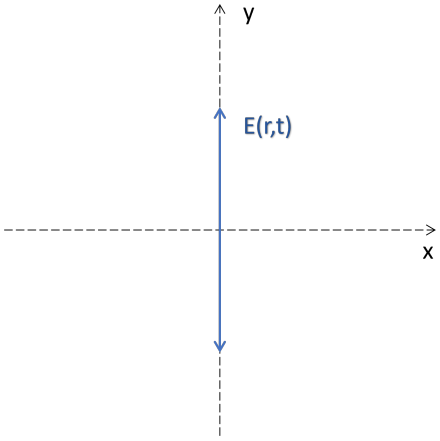

(b) y-linearly polarized light

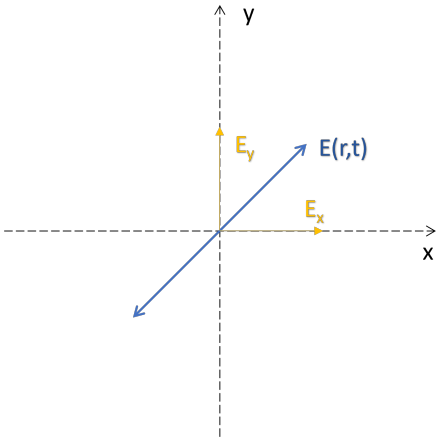

(c) +45°-linearly polarized light

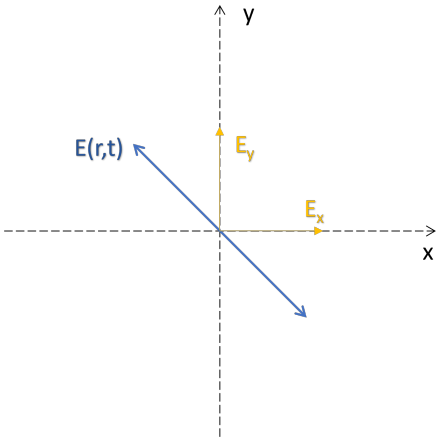

(d) -45°-linearly polarized light

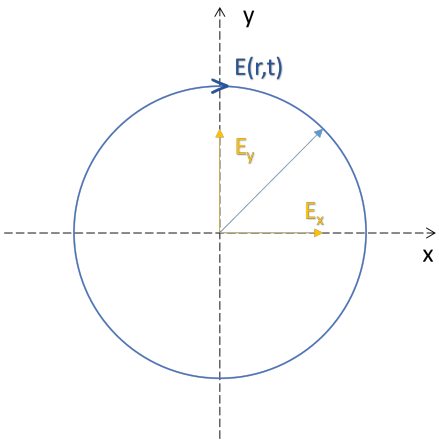

(e) Right-handed circular polarized light

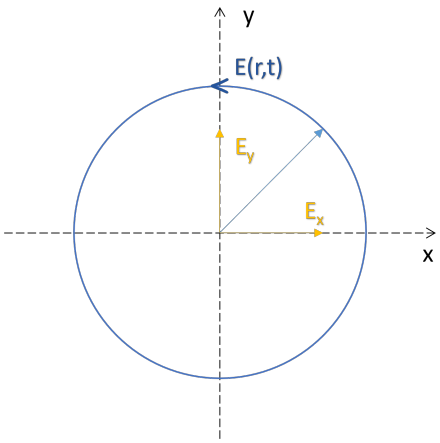

(f) Left-handed circular polarized light

Figure 2.1: 6 basic polarization states

When it comes to defining polarization, it is extremely important to define the two orthogonal components, s- and p- polarization, in relation the surface of interest. We first define the plane of incidence, which is the plane formed by the surface normal and the incoming wave direction. Then, electric field component is decomposed into two perpendicular directions, the p-polarization is the electric field parallel to the plane of incidence, and the s-polarization is the electric field perpendicular to the plane of incidence[8]. The "s" comes from the German word "senkrecht", which means perpendicular.

Similarly, we need to define the s and p polarization for the refracted wave. This is done by defining a scatter plane, which is the plane spanned by the incoming wave and the scattered wave. For the scattered wave, the p-polarization is again parallel to the scatter plane, and the s-polarization is perpendicular to this plane[8].

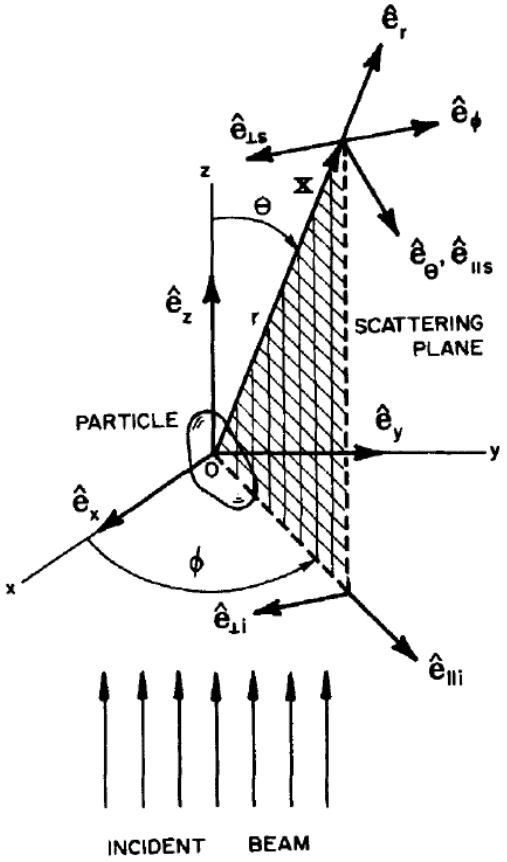

Figure 2.2: Scatter plane illustration from *Absorption and scattering of light by small particles* [8]. Here, the p- and s-polarisation are denoted $\parallel$ and $\perp$ respectively

Polarization States and Representations

There are different way to describe polarization mathematically, with the two most used formalism are the Jones formalism and the Stokes formalism. Additionally, a way of visualizing polarization is introduced here with the polarization ellipse.

Jones vector

The Jones representation decomposes the electric field in two perpendicular directions, and structures them in a vector known as the Jones vector[7]:

$$\mathbf{E} = \begin{bmatrix} E_x \\ E_y \end{bmatrix} \quad , \tag{2.25}$$

where E_x and E_y are the complex, time dependent amplitudes of the electric field in the x and y directions, i.e. $E_x = |E_x|e^{i\delta_x}$ and $E_y = |E_y|e^{i\delta_y}$.

Revisiting the six cases seen in figure 2.1, the Jones vector representation of these states are shown in table 2.1.

Table 2.1: Jones representation of the 6 basic polarization states

$\mathbf{E}_x$	$\mathbf{E}_y$
$\begin{bmatrix} 1 \\ 0 \end{bmatrix}$	$\begin{bmatrix} 0 \\ 1 \end{bmatrix}$
$\mathbf{E}_{+45}$	$\mathbf{E}_{-45}$
$\frac{1}{\sqrt{2}} \begin{bmatrix} 1 \\ 1 \end{bmatrix}$	$\frac{1}{\sqrt{2}} \begin{bmatrix} 1 \\ -1 \end{bmatrix}$
$\mathbf{E}_{rcp}$	$\mathbf{E}_{lcp}$
$\frac{1}{\sqrt{2}} \begin{bmatrix} 1 \\ i \end{bmatrix}$	$\frac{1}{\sqrt{2}} \begin{bmatrix} 1 \\ -i \end{bmatrix}$

Stokes formalism

Stokes representation describes the polarization state with four parameters (S_0, S_1, S_2, S_3)[7]. They are calculated using the intensity (I), amplitude and phase of the electric field in six different polarisation states:

$$S = \begin{bmatrix} S_0 \\ S_1 \\ S_2 \\ S_3 \end{bmatrix} \quad , \tag{2.26}$$

where

$$S_0 = I_x + I_y$$

$$S_1 = I_x - I_y$$

$$S_2 = I_{+45} - I_{-45}$$

$$S_3 = I_r cp - I_l cp$$

- I_x and I_y are the intensities in the x and y directions
- $I_r cp$ and $I_l cp$ are the intensities of light that are right and left circular polarized
- I_{+45} and I_{-45} are the intensities in the +45 and -45 directions relative to x and y

Compared to the Jones formalism, the Stokes formalism have the advantage that it also includes polarization states that are partially polarized and unpolarized states.

Polarization ellipse

The polarization ellipse is visual way of understanding the polarization state. The polarization ellipse are described by four parameters[7]:

- The amplitude $A = \sqrt{a^2 + b^2}$, where a and b, which are the major and minor axis of the ellipse, respectively.
- The azimuth angle θ, which is the angle between the major axis and the x-axis
- The phase difference δ, which here is defines as the angle between the major axis and the electric field direction at t=0
- The ellipticity angle, $\epsilon = arctan\frac{b}{a}$

These parameters are visualised in figure 2.3.

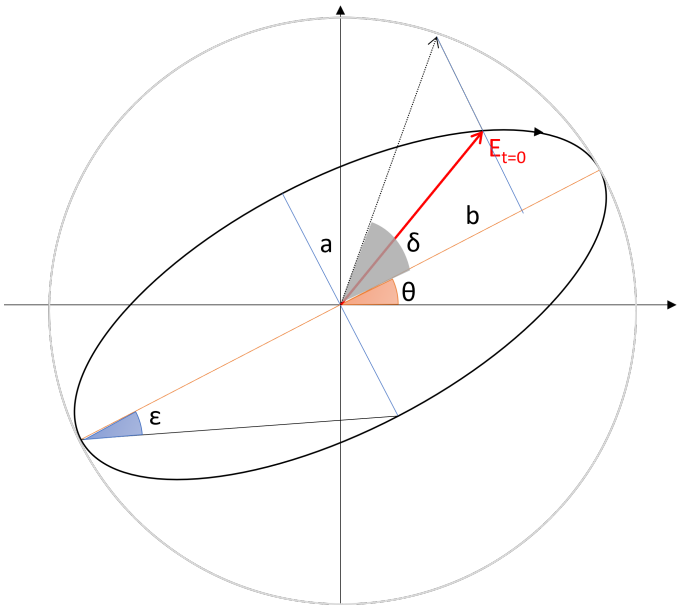

Figure 2.3: Polarization ellipse with is parameters illustrated

2.1.3 Polarizing Elements

When light traverses an optical system, its polarization state can be altered, transforming from its initial state to a new one upon exit. This transformation can be broadly classified into four fundamental categories: depolarizer, retarder, diattenuator, and polarizer[7].

Depolarizers decrease the degree of polarization in light, and is independent of the incoming light's polarization state. Depolarizers convert polarized light to unpolarized light by introducing random phase shifts on the p- and s-components of the light's electric field. This resulting light averages over time to an unpolarized state.

Retarders change the phase of the components of the incoming electric field, without any diattenuation.

Dittenuators change the amplitude of the components of the incoming electric field, without any retardance.

Polarizers are optical elements that transmits a specific polarization state, independent of the incident polarization state

Both the Jones formalism and the Stoke formalism have mathematical ways of describing how a polarizing element interact with light. In the Jones formalism, this is described by a Jones matrix.

A Jones matrix is a two by two matrix constructed such that

$$E_{out} = JE_{in} \tag{2.27}$$

where E_{out} and E_{in} are the Jones vectors before and after the polarizing element respectively, and J is the Jones matrix on the form

$$J = \begin{bmatrix} j_{11} & j_{12} \\ j_{21} & j_{22} \end{bmatrix} \tag{2.28}$$

It is thus possible to calculate the Jones matrix by knowing the optical response from a x linear polarization state and an y linear polarization state:

$$\begin{aligned} j_{11} &= \frac{E_{ox}}{E_{ix}}|E_{iy} = 0, \quad j_{12} = \frac{E_{ox}}{E_{iy}}|E_{ix} = 0 \\ j_{21} &= \frac{E_{oy}}{E_{ix}}|E_{iy} = 0, \quad j_{22} = \frac{E_{oy}}{E_{iy}}|E_{ix} = 0 \end{aligned} \tag{2.29}$$

Looking back at our basic states, ideal polarizers that creates these states can be described by the following Jones matrices:

$$\begin{aligned} J_x &= \begin{bmatrix} 1 & 0 \\ 0 & 0 \end{bmatrix} \quad J_y = \begin{bmatrix} 0 & 0 \\ 0 & 1 \end{bmatrix} \\ J_{+45} &= \frac{1}{\sqrt{2}} \begin{bmatrix} 1 & 1 \\ 1 & -1 \end{bmatrix} \quad J_{-45} = \frac{1}{\sqrt{2}} \begin{bmatrix} 1 & -1 \\ 1 & 1 \end{bmatrix} \\ J_{rcp} &= \frac{1}{\sqrt{2}} \begin{bmatrix} 1 & -i \\ i & 1 \end{bmatrix} \quad J_{lcp} = \frac{1}{\sqrt{2}} \begin{bmatrix} 1 & i \\ -i & 1 \end{bmatrix} \end{aligned}$$

In the same way, there exists a matrix that correlates the incoming and outcoming Stoke vector for a optical system, named the Mueller matrix.

$$S_{out} = MS_{in} \tag{2.30}$$

where S_{out} and S_{in} are the Stoke vectors before and after the polarizing element respectively, and M is the Mueller matrix on the form

$$M = \begin{bmatrix} m_{11} & m_{12} & m_{13} & m_{14} \\ m_{21} & m_{22} & m_{23} & m_{24} \\ m_{31} & m_{32} & m_{33} & m_{34} \\ m_{41} & m_{42} & m_{43} & m_{44} \end{bmatrix} \tag{2.31}$$

The Mueller matrix is more complex and harder to measure, but in return gives more information regarding the depolarization effects of the element. How to physically measure the Mueller Matrix will be presented in the Ellipsometry section. It is also possible to create a quasi Mueller Matrix from the Jones matrix, known as the Jones-Mueller Matrix.

$$M_J = A(J \otimes J^*)A^{-1} \tag{2.32}$$

where J^* is the complex conjugate of the Jones matrix, and A and A^{-1} are given by:

$$A = \begin{bmatrix} 1 & 0 & 0 & 1 \\ 1 & 0 & 0 & -1 \\ 0 & 1 & 1 & 0 \\ 0 & i & -i & 0 \end{bmatrix} \qquad A^{-1} = \frac{1}{2}\begin{bmatrix} 1 & 1 & 0 & 0 \\ 0 & 0 & 1 & -i \\ 0 & 0 & 1 & i \\ 1 & -1 & 0 & 0 \end{bmatrix} \tag{2.33}$$

The Mueller Matrix to generate the six basic states[7] are :

$$\begin{aligned} M_x &= \frac{1}{2}\begin{bmatrix} 1 & 1 & 0 & 0 \\ 1 & 1 & 0 & 0 \\ 0 & 0 & 0 & 0 \\ 0 & 0 & 0 & 0 \end{bmatrix} \qquad M_y = \frac{1}{2}\begin{bmatrix} 1 & -1 & 0 & 0 \\ -1 & 1 & 0 & 0 \\ 0 & 0 & 0 & 0 \\ 0 & 0 & 0 & 0 \end{bmatrix} \\ M_{+45} &= \frac{1}{2}\begin{bmatrix} 1 & 0 & 1 & 0 \\ 0 & 0 & 0 & 0 \\ 1 & 0 & 1 & 0 \\ 0 & 0 & 0 & 0 \end{bmatrix} \qquad M_{-45} = \frac{1}{2}\begin{bmatrix} 1 & 0 & -1 & 0 \\ 0 & 0 & 0 & 0 \\ -1 & 0 & 1 & 0 \\ 0 & 0 & 0 & 0 \end{bmatrix} \\ M_{rcp} &= \frac{1}{2}\begin{bmatrix} 1 & 0 & 0 & 1 \\ 0 & 0 & 0 & 0 \\ 0 & 0 & 0 & 0 \\ 1 & 0 & 0 & 1 \end{bmatrix} \qquad M_{lcp} = \frac{1}{2}\begin{bmatrix} 1 & 0 & 0 & -1 \\ 0 & 0 & 0 & 0 \\ 0 & 0 & 0 & 0 \\ -1 & 0 & 0 & 1 \end{bmatrix} \end{aligned} \tag{2.34}$$

2.1.4 Light-Matter interaction

Reflection and Transmission

Light, as described in equation 2.23, is a propagating wave through a medium. At any intersection between two medium, certain boundary conditions arises as a discontinuous field is physically impossible. Depending on the two media, the polarization of the light, the angle of incident and the wavelength of the light, the light can both be reflected and transmitted.

The law of reflection relates the incoming angle and the reflected angle on a smooth surface as [7]:

$$\theta_i = \theta_r \tag{2.35}$$

The angle of the transmitted wave is given by Snell's law, which is a result of change of velocity between the two materials[7]:

$$N_0 sin\theta_0 = N_1 sin\theta_1 \tag{2.36}$$

The generalised form of Snell's law also include a phase term, as we allow an abrupt phase shift

over the interface between the two media[9]:

$$N_0 sin\theta_0 - N_1 sin\theta_1 = \frac{\lambda}{2\pi}\frac{d\phi}{dx} \tag{2.37}$$

How much of the incoming light which is transmitted or reflected, is determined by the incoming angle and the two materials

The boundary condition that needs to be fulfilled are that the tangential components of the E and H field needs to be continuous across the intersection. This results in the reflection coefficient for s-polarized and p-polarized light[7]:

$$r_s = \frac{N_0 cos\theta_0 - N_1 cos\theta_1}{N_0 cos\theta_0 + N_1 cos\theta_1} \tag{2.38a}$$

$$r_p = \frac{N_1 cos\theta_0 - N_0 cos\theta_1}{N_0 cos\theta_0 + N_1 cos\theta_1} \tag{2.38b}$$

where N_0 and N_1 are the refractive indices of the originating and introduced medium respectively, and θ_0 and θ_1, are the angle of incidence and angle of reflection is given by the law of reflection2.35. The transmission coefficients for the two polarization states similarly becomes:

$$t_s = \frac{2N_0 cos\theta_0}{N_1 cos\theta_0 + N_0 cos\theta_1} \tag{2.39a}$$

$$t_p = \frac{2N_0 cos\theta_0}{N_1 cos\theta_0 + N_0 cos\theta_1} \tag{2.39b}$$

Here, θ_0 and θ_1, are the angle of incidence and angle of reflection given by Snell's law2.37

Two interesting angles of incidence can be deduced from these equations:

- **Principal angle** is the angle of incidence where a linearly polarized wave will be reflected as an elliptical polarized wave, due to a phase difference of $\frac{\pi}{2}$ between the s- and p- polarization.
- **Brewster angle**: When light is incident on a surface at the Brewster angle, the reflected light becomes completely polarized parallel to the surface. This phenomenon is known as Brewster's Law and the angle is given by:

  $$\tan(\theta_B) = \frac{n_2}{n_1},$$

  where θ_B is the Brewster angle, and n_1 and n_2 are the refractive indices of the first and second mediums, respectively.

Diffraction

When light passes through narrow slits and other geometrical structures, the transmitted light will scatter in a pattern depending on the geometric surface. This is known as diffraction, and is most famously described by Young's double-slit experiment which proves the duality of light. To

understand the wave nature of diffraction, we first introduce the Huygens-Fresnel principle, which consider each point on a wavefront as a secondary source of light.

For an aperture placed in a plane (ξ, η) and illuminated in the positive z-direction, the resulting wave field in a parallel plane (x, y) at a distance z is expressed in Goodman's Fourier Optics ch.4 as [10]:

$$U(x,y) = \frac{z}{j\lambda} \iint_{\Sigma} U(\xi,\eta) \frac{e^{jkr_{01}}}{r_{01}^2} d\xi d\eta, \tag{2.40}$$

where the distance r_{01} is given by

$$r_{01} = \sqrt{z^2 + (x-\xi)^2 + (y-\eta)^2} \tag{2.41}$$

When observing the diffraction at a distance comparable to the size of the aperture, the Fresnel approximation is used[10], which approximates r_{01} to

$$r_{01} \approx z[1 + \frac{1}{2}(\frac{x-\xi}{z})^2 + \frac{1}{2}(\frac{y-\eta}{z})^2] \tag{2.42}$$

This simplifies equation 2.43 to

$$U(x,y) = \frac{e^{jkz}}{j\lambda z} \iint_{\infty}^{\infty} U(\xi,\eta) e^{j\frac{k}{2z}[(x-\xi)^2+(y-\eta)^2]} d\xi d\eta \quad , \tag{2.43}$$

which is known as the Fresnel diffraction integral[10].

Further simplifications can be done if we consider the observation at a distance z far from the diffraction aperture, known as the Fraunhofer approximation[10].

$$z \gg \frac{k(\xi^2+\eta^2)_{max}}{2} \tag{2.44}$$

This leads to the Fraunhofer diffraction integral[10]:

$$U(x,y) = \frac{e^{jkz} e^{j\frac{k}{2z}(x^2+y^2)}}{j\lambda z} \iint_{\infty}^{\infty} U(\xi,\eta) e^{-j\frac{2\pi}{\lambda z}(x\xi+y\eta)} d\xi d\eta \quad , \tag{2.45}$$

Considering a single slit, the diffracted intensity can be expressed as [10]:

$$I(\theta) = I_0[sinc(\frac{\pi a}{\lambda} sin\theta)]^2 \tag{2.46}$$

This function has minima and maxima where

$$sin\theta_{minima} = \frac{n\lambda}{a} \qquad sin\theta_{maxima} = \frac{2n+1}{2}\frac{\lambda}{a} \quad , \tag{2.47}$$

where n=1 is the first zero of $I(\theta)$ in equation 2.46

For a generalised case of n-slits, the intensity function is a product of the diffraction expression, and an interference function[11]:

$$I(\theta) = I_0[sinc(\frac{\pi a}{\lambda} sin\theta)]^2 \left[\frac{sin(\frac{N\pi d}{lambda} sin\theta)}{sin(\frac{\pi d}{lambda} sin\theta)}\right]^2 \quad , \tag{2.48}$$

which is a modulated version of the single slit intensity 2.46, with the maximas located at

$$sin\theta_m = \frac{m\lambda}{d} \quad , \tag{2.49}$$

where d is the distance between the slits and θ_m is the angle of diffracted order m. Equation 2.49 gives the same result as Bragg's law of diffraction.

Propagation and loss

When light propagates through a medium, its intensity can decrease due to absorption. This is often described using the complex refractive index. The complex refractive index, $\tilde{n}$, can be expressed as[12]:

$$\tilde{n} = n + ik \quad , \tag{2.50}$$

where:

- n is the real part of the refractive index, often referred to as the refractive index. It accounts for the phase velocity of light and is used to describe refraction, as seen in equation 2.37
- k is the imaginary part of the refractive index, often referred to as the extinction coefficient. It accounts for the absorption of light in the medium.

The permittivity, $\tilde{\epsilon}$, of a medium is related to the refractive index. The complex permittivity, $\tilde{\epsilon}$, is given by[12]:

$$\tilde{\epsilon} = \varepsilon' + i\varepsilon'' \quad , \tag{2.51}$$

where:

- ε' is the real part of the permittivity, related to the storage of energy.
- ε'' is the imaginary part of the permittivity, related to the loss or dissipation of energy.

The relationship between the complex refractive index and the complex permittivity is given by:

$$\tilde{n} = \sqrt{\tilde{\epsilon}} \tag{2.52}$$

Materials, dipole moment and electric field

The interaction between a material and an applied electric field is described through the equation:

$$\mathbf{D} = \epsilon_0 \mathbf{E} + \mathbf{P} \tag{2.53}$$

where D is the dielectric field, E is the external electric field and P is the polarization of the medium. The polarization can also be written as a function of the applied electric field

$$\mathbf{P} = \epsilon_0 \chi \mathbf{E} \tag{2.54}$$

where χ is introduced as the dielectric susceptibility. As convention, this is baked into a simple expression for a material specific dielectric response to the applied electric field, 2.11. The relation between the material specific dielectric constant and the dielectric susceptibility is defined in the frequency domain as

$$\epsilon(\omega) = 1 - \chi(\omega) \tag{2.55}$$

Different models are developed to find this frequency dependent dielectric susceptibility function, as different models works for different material types. Most common are the Lorentz model and the Drude model, which will be introduced and briefly discussed here.

The Lorentz Model The Lorentz model describes each electron in a classical oscillator model, with the assumption that the atomic binding is the binding force, and the oscillating electric field is the driving force of movement. This result in the dielectric function [12]:

$$\epsilon(\omega) = 1 - \frac{\omega_p^2}{\omega^2 - \omega_0^2 + \frac{i\omega}{\tau}} \tag{2.56}$$

The Lorentz model is popular due to its relatively easy to understand and describe, and it works well for optical spectrum. However, it has some drawbacks due to a lack of inclusion of several physical forces in the derivation[12].

The Drude Model The Drude model assumes a free electron cloud, which is a fair assumption for several metals, such that there is no restoring force as with the Lorenz model. This results in the dielectric function [12]:

$$\epsilon(\omega) = 1 - \frac{\omega_p^2}{\omega^2 + \frac{i\omega}{\tau}} \tag{2.57}$$

2.1.5 Modelling of Optical medium

When modeling the transmission and reflectance of a single isotropic thin film, three different fields needs to be considered; the ambient field from which the wave originates, the field within the thin film layer and the field in the substrate. As the substrate is assumed to be much larger than the thin film, the light is assumed to only travel in one direction in this area. However, in the thin film and the ambient region, the wave can travel in both directions due to reflections. As per Arwin chapter 7.2 [7], the resulting total reflection and transmittance for s- and p-polarized light is expressed as

$$r_s = \frac{r_{01s} + r_{12s}e^{i2\beta}}{1 + r_{01s}r_{12s}e^{i2\beta}} \tag{2.58}$$

$$r_p = \frac{r_{01p} + r_{12p}e^{i2\beta}}{1 + r_{01p}r_{12p}e^{i2\beta}} \tag{2.59}$$

$$t_s = \frac{t_{01s}t_{12s}e^{i2\beta}}{1 + r_{01s}r_{12s}e^{i2\beta}} \tag{2.60}$$

$$t_p = \frac{t_{01p} + t_{12p}e^{i2\beta}}{1 + r_{01p}r_{12p}e^{i2\beta}} \tag{2.61}$$

$$\tag{2.62}$$

Here, the subscript 01 refers to the reflection from the interface between the ambient field and the thin film (layer 0 and 1) etc. The film thickness is introduced in the *film phase thickness* parameter β:

$$\beta = \frac{2\pi d}{\lambda} N_1 cos\theta_1 \tag{2.63}$$

To adapt this relation for an arbitrary number of layers, this methodology is further developed to use matrix algebra. This is done by introducing two matrices, the interface matrix and the layer matrix. The interface matrix describes how an interface reflect and transmit an incoming wave by

$$\begin{bmatrix} E_i^+ \\ E_i^- \end{bmatrix} = \begin{bmatrix} I_{11} & I_{12} \\ I_{21} & I_{22} \end{bmatrix} \begin{bmatrix} E_j^+ \\ E_j^- \end{bmatrix} \tag{2.64}$$

The layer matrix describes the effect of propagation through a layer of thickness d.

$$\begin{bmatrix} E_0^+ \\ E_0^- \end{bmatrix} = \begin{bmatrix} e^{-i\beta} & 0 \\ 0 & e^{i\beta} \end{bmatrix} \begin{bmatrix} E_d^+ \\ E_d^- \end{bmatrix} \tag{2.65}$$

The scattering matrix $\mathbf{S}$ is then a result of a multiplication of alternating interface matrices and layer matrices, defined for a system of m layers as[7]:

$$\mathbf{S} = \mathbf{I}_{01}\mathbf{L}_1\mathbf{I}_{12}...\mathbf{L}_m\mathbf{I}_{(m)(m+1)} \tag{2.66}$$

Such that the relation between the incoming and outgoing fields are $\mathbf{E}_1 = \mathbf{S}_{12}\mathbf{E}_2$

Considering a general case, taking into account anisotropic medium, this becomes more complicated. The approach is similar to that of an isotropic medium. A transfer matrix $\mathbf{T}$ is defined as

$$\begin{bmatrix} A_s \\ B_s \\ A_p \\ B_p \end{bmatrix} = \mathbf{T} \begin{bmatrix} F_s \\ G_s \\ F_p \\ G_p \end{bmatrix} \tag{2.67}$$

where A, B and F are the incident, reflected and transmitted fields respectively, and G is the back-reflected field, which for sufficiently absorbing systems or systems with back-side far is set to 0[7].

Angular spectrum

When analyzing and modelling propagation of light, the angular spectrum method is a powerful tool, as it is gives the optical field along any plane at a distance z from the plane of diffraction, and its results corresponds with the Fourier optics.

The following explanation is based on chapter 3.9 in Goodman's Fourier Optics[10]:

Using the Huygens-Fresnel principle, each point is considered a source of spherical waves. By defining the optical field along a plane where z=0, expressed as $U(x, y, 0)$, with an ultimate goal of finding the optical field $U(x, y, z)$ along any plane.

Starting with the Fourier transform of $U(x, y, 0)$:

$$A(f_X, f_y; 0) = \int_{-\infty}^{\infty}\int_{-\infty}^{\infty} U(x, y; 0)exp[-j2\pi(f_X x + f_Y y)]dxdy \tag{2.68}$$

such that the inverse Fourier transform is given by:

$$U(x, y; 0) = \int_{-\infty}^{\infty}\int_{-\infty}^{\infty} A(f_X, f_Y; 0)exp[j2\pi(f_X x + f_Y y)]df_X df_Y \tag{2.69}$$

From the inverse Fourier transform, it is easy to compare the optical field to a sum of plane waves. The term $exp[j2\pi(f_X x + f_Y y))]$ is analogue to a plane wave propagating in the direction given by the directional cosines $\alpha = \lambda f_X$ and $\beta = \lambda f_Y$. Here, $cos^{-1}\alpha$ is the angle in the x-z plane and $cos^{-1}\beta$ is the angle along the y-z plane. Thus, we can rewrite equation 2.68 to

$$A(\frac{\alpha}{\lambda}, \frac{\beta}{\lambda}; 0) = \int_{-\infty}^{\infty}\int_{-\infty}^{\infty} U(x, y; 0)exp[-j2\pi(\frac{\alpha}{\lambda}x + \frac{\beta}{\lambda}y)]dxdy \tag{2.70}$$

To find the Fourier transform at an arbitrary plane z = const, we use the fact that equation 2.69 must satisfy the Helmholtz equation, $\nabla^2 U + k^2 U = 0$

$$\frac{d^2}{dz^2}A(\frac{\alpha}{\lambda}, \frac{\beta}{\lambda}; z) + (\frac{2\pi}{\lambda})^2[1 - \alpha^2 - \beta^2]A(\frac{\alpha}{\lambda}, \frac{\beta}{\lambda}; z) = 0 \tag{2.71}$$

The elementary solution to this equation is

$$A(\frac{\alpha}{\lambda}, \frac{\beta}{\lambda}; z) = A(\frac{\alpha}{\lambda}, \frac{\beta}{\lambda}; 0)exp(j\frac{2\pi}{\lambda}\sqrt{1 - \alpha^2 - \beta^2}) \tag{2.72}$$

Finally, to obtain the optical field at any z, the inverse Fourier transform of 2.72 is taken, with an added circ function in order to limit the solution where $\alpha^2 + \beta^2 < 1$, for the directional cosines to be real.

$$U(x, y, z) = \int\int_{-\infty}^{\infty} A(\frac{\alpha}{\lambda}, \frac{\beta}{\lambda}; 0)exp(j\frac{\pi}{\lambda}\sqrt{1 - \alpha^2 - \beta^2}) \times circ(\sqrt{\alpha^2 + \beta^2})exp][j2\pi(\frac{\alpha}{\lambda}x + \frac{\beta}{\lambda}y)]d\frac{\alpha}{\lambda}d\frac{\beta}{\lambda} \tag{2.73}$$

2.1.6 Optical Metasurfaces

The advances in the last decades regarding manufacturing of micro and nano structures, has allowed for devices previously only theoretically possible. By decreasing the feature size down to a size comparable to the wavelength of light, metasurfaces can be designed to specific purposes such as focusing, splitting and, polarization of light. An optical metasurface is a arrangement of sub-wavelength structures, designed to manipulate and or control the properties of light. Compared to regular optical elements such as lenses, metasurfaces achieve the control of light through the layout of the structures, instead of curvature of materials. The sub-wavelength structures are often referred to as meta-atoms, can be designed to control the phase, amplitude and polarization of light, through engineered choice of geometry and material composition. One of these applications are polarimetric beam splitting devices. These devices allow for a splitting of the incoming beam, whereas two different types of polarization states are directed towards an opposite angle.

In general, a metasurface must be able to generate a phase-shift of 2π using a single meta-atom, otherwise known as a unit cell. One possible way of achieving this phase-shift is to use a dielectric, preferable with a high refractive index. This dielectric meta-atom will then generate modes of electric and or magnetic dipole modes, which will generate a phase shift. This phase shift is again controlled by the physical dimensions of the meta-atom, such as the width and eight of a rectangle, or the diameters of an ellipse.

These electric and magnetic modes can also be generated in metallic meta-atoms on a insulating surface such as glass (SiO2). However, this significantly reduces the transmission coefficient of the system, as the structure absorbs much of the light. Another approach, which has proved very efficient, is using metallic patches and placing them over an optical mirror, separated by an insulating layer such as SiO2. This will create a coupling between the metallic patches and the mirror, inducing gap surface plasmons(GSP).

The summarizing paper by Ding et. al. [1] describes the different types of beam splitting metasurfaces created in the recent years. Here, optical metasurfaces are classified into the following sub-categories:

1. Metasurfaces featuring electric dipole response. This is the simplest metasurface, which in is simplest form consists of a sub-wavelength periodic array of meta-atoms with a pure electric response. If the metasurface has an isotropic response, the phase control is limited to $-\pi/2 \leq \phi_t \leq \pi/2$, and a direct relation between the phase and the transmission as $|t| = cos\phi_t$. However, introducing anisotropy in the meta-atoms allows for cross-polarization of light, giving a full 2π control of the phase ϕ_t. Additionally, the transmission coefficient can now be separated to cross polarized transmission and co polarized transmission, t_{xy} and t_{xx}, with the constraint $|r_{xx}|^2 + |r_{xy}|^2 + |t_{xx}|^2 + |t_{xy}|^2 = 1$. It can be shown that the maximum theoretical efficiency of such a metasurface is 25%. The value of t_{xy} is maximised at an

rotation of $\pi/4$, which is utilized when splitting $\pm 45^\circ$ polarization states[1].

2. Geometric metasurfaces, which separates circular polarized light by a geometric induced phase gradient, known as a Pancharatnam-berry phase. Using a rotation of the meta-atom such as $\theta(x) = \pi\lambda/\Lambda$, where Λ is the periodicity, the associated plane wave in the far-field will gain a vector component of $k_x = \pm 2\pi/\Lambda$. This means that right handed polarized light and left handed polarized light will propagate whit an opposite angle in respect to the surface normal[1].

3. Metasurfaces near a metal screen. A perfect electric conductor (PEC) is introduced at a distance $h \ll \lambda$, separated by a spacer with similar optical properties as the surrounding medium. This allows for electrostatic image theory to be applied, to draw an equivalent to a system with two identical metasurfaces separated by a distance $2h$ with an equal but out of phase electric dipole response. These metasurfaces allow for control of both circular and linear polarization states, operating in reflection[1].

4. Metasurfaces featuring electric and magnetic dipole responses. These are often refereed to as Huygens metasurfaces, and these metasurfaces can be engineered to reach zero transmission or reflection[1].

5. Metasurfaces featuring magneto-electric coupling. These metasurfaces include the possibility of a magnetic field inducing a electric response, and an electric field inducing a magnetic response. Some additional possibilities from this includes a reflection coefficient depending on the incident angle, and the possibility to design narrow frequency bands of reflection[1].

2.2 Nanofabrication

In order to accurately manufacture the designed metasurfaces for this thesis, nanofabrication techniques such as lithography, etching and thin film deposition are essential. The theory behind the used and considered processes are discussed in this section.

2.2.1 Lithography

Lithography is the process of writing patterns of scales from micrometers to nanometers onto a substrate, using either light or electrons. The basic principle is that a reactive chemical (resist) is applied to the substrate, and the exposure by electrons or light, depending on the resist, will either harden or soften the chemical. Using a high resolution light beam, this can give the resolution of hundreds of nanometers. Using electron beams instead, which have a much smaller beam radius, can give resolutions down to a couple of nanometers. After exposure, the substrate is subsequently developed by submerging in a resist-specific chemical, such that only the hardened pattern remains

from the resist remains. Thus the sample is ready for further processes, such as thin film deposition or etching, to transfer the pattern from the resist to the substrate itself. The steps in this process are explained in the 8 steps of lithography.

The 8 steps of lithography

1. **Vapor priming** The purpose of this step is to remove all contamination from the substrate, and improve adhesion of the photoresist if necessary. The common procedure for this is done with an acetone bath, followed by a rinse with either ethanol or isopropanol (IPA), as residual acetone leaves a thin layer which will contaminate the substrate. This is followed by ozone cleaning, which is done in an oxygen enriched chamber with UV-lamps, as the UV light will create ozone from oxygen. Finally a dehydration bake is performed to evaporate any liquids remaining after on the substrate. This is done by placing the substrate on a hotplate keeping an elevated temperature around 150 °C for a few minutes. Other options include piranha etch and plasma cleaning, for dirtier samples. If required, an adhesion layer can be applied through spin-coating, if the adhesion of the photoresist to the substrate is poor.

2. **Spin coat** The photoresist is applied to to substrate as a thin layer by spin coating. The substrate is placed on a spinner, and held in place with vacuum. The selected photoresist is applied in liquid state to the substrate by the use of a pipette, and the subsequent spinning distributes the photoresist evenly. Spin speed, acceleration and duration are parameters that decide the resulting thickness of the layer. After applying the photoresist, the backside and edges of the substrate is cleaned with acetone on a q-tip, as build-up of photoresist on the back-side will lead to a tilt of the sample in the exposure process, which is bad.

3. **Soft bake** In order to improve the adhesion of the photoresist to the wafer, as well as to evaporate off solvents in the photoresist, the substrate is placed on a hotplate at a given temperature and time. This step is known as a soft bake. The temperature and time parameters of the soft bake is found in the data sheet of the relevant photoresist.

4. **Alignment and exposure** Transfer of the desired pattern to the photoresist is done by illuminating the photoresist with light or electrons, depending on the photoresist and desired resolution. This can be done with a physical mask, which covers the areas that should not be illuminated, and a mask-less aligner (MLA), which uses an internal optical system to produce UV light that only illuminates the desired portions of the photoresist. Although highly flexible, the MLA illuminates the photoresist sequentially – a time consuming process. Thus, MLA is common in research where only a few prototype devices are created, while physical masks are much more commonly found in mass production. The wavelength of the light and its dose are parameters that vary with the individual photoresist. The data sheet of the photoresist will give rough recommended values, but experimental dose tests are often required to ensure best results.

5. **Post exposure bake (optional)** The post exposure bake is an optional heat treatment performed to catalyse reactions from light exposure, hardening or softening the exposed pattern, depending on the photoresist. It may help improve adhesion between photoresist and the wafer. As for the soft bake, the temperature cycle of the post exposure bake is normally found in the data sheet of the photoresist.

6. **Development** Developing is the process of removing the sections of photoresist that is not hardened following light exposure, by exposing the photoresist to a developer, a photoresist specific chemical that dissolves the originally soft or softened areas. The time of development needs to be adjusted such that all the unhardened photoresist is dissolved, and none of the hardened photoresist is dissolved. To stop the developing process, the coated wafer is removed from the developer, placed in water, and dried with nitrogen.

7. **Hard bake (optional)** A final optional heat treatment known as a hard bake may be performed, to further improve photoresist-substrate adhesion, prepare the coated wafer for further processing and remove any remaining solvents. If required, the temperature cycle is available in the photoresist data sheet.

8. **Sample inspection** The final step entails inspection of the sample and classification of the results of the photolithography process. Optical microscopes are commonly used for this purpose. An ideal result is achieved when no defects or contamination are present in the structure, and the structure looks as intended.

Electron Beam Lithography (EBL)

Electron Beam Lithography is similar in operation to optical lithography, with some fundamental some more unobvious differences. The resist reacts to electrons, and an electron beam is controlled to expose the pattern. The electron beam has a much smaller diameter compared to light, giving a much higher resolution on he resulting pattern.

An electron beam can achieve a lot smaller focal radii compared to light, and following will give a higher resolution. The radii of the electron beam is dependent on the current used, and with the ELLIONIX at NanoLab can be as low as 1.8 nm.

Steps for using EBL:

1. **Select beam configurations**

2. **Load sample** The exposure is performed in vacuum, and in order to safely and efficiently do this, there is a strict loading procedure that must be followed. There are two chambers, one main chamber where the exposure happens and a loading chamber where the sample is inserted and retrieved. To transfer the sample to the main chamber, the sample must be

placed on a cartridge in loading chamber, and the chamber must be pumped to vacuum. Then, the valve between the two chambers can be opened, and the sample can be moved to the main chamber by a handling rod controlled from the outside.

3. **Adjust electron beam** The current of the electron beam should first be measured in a Faraday cup in the EBL, to verify that the actual beam current is the same as set in the settings. If this deviates, it can be adjusted. Next, the electron beam must be focused to the sample, to achieve the best resolution possible. Both focus and stigma in x and y direction must be adjusted. This is done with visual feedback, as the EBL has SEM detectors, and the beam is adjusted until a good SEM image is achieved. Then, the beam current needs to be verified again, to make sure the change in focus and stigma did not affect the current.

4. **Add exposure file to system** The desired exposure pattern is uploaded to the EBL software, and the write fields are assigned. Write fields tells the system which are to scan in which order. The electron beam can be shifted without moving the sample or electron source, by applying an electric field. However, there is a limit to how far the beam can be shifted, especially without affecting the focus. Thus, the EBL moves the electron beam mechanically to a write field, and whitin the write field the beam is only controlled by applying electromagnetic fields. The system automatically splits the design into such write field, based on the desired size of each write field inputted by the user.

5. **Calculate and set dose** Utilizing the desired beam current and the required dose of the resist, the dose time is calculated and applied to each desired layer.

6. **Check for tilt** The tilt of the sample is measured, and if the tilt is greater than one mRad in any direction, the sample needs to be adjusted. This emerges from the fact that the electron beam is calibrated and focused at a spesific working distance from the electron source, in order to get the desired resolution. A tilt will imply a change in height when the electron beam scans across the sample, and the electron beam will interact with the sample with a higher radii and thus lower dose. This would cause both worse resolution and potentially underexposed samples.

7. **Field alignment correction** As mentioned, the system creates write fields in order to optimize write speed. The features at the edges of these write fields and those who overlap several write fields are suspectible to misaligment, as the errors increase from the center of the write field. Thus, before each exposer, it is importante to calibrate the alignemnt of the write fields, which the EBL does itself.

Compared to light, electrons scatter more extensively within the resist. This leads to an exposure wider than the electron beam, and an undercut in the resist walls after development. Conversely, light doesn't penetrate as deeply into the resist, resulting in overcut walls. This is illustrated in figure 2.4

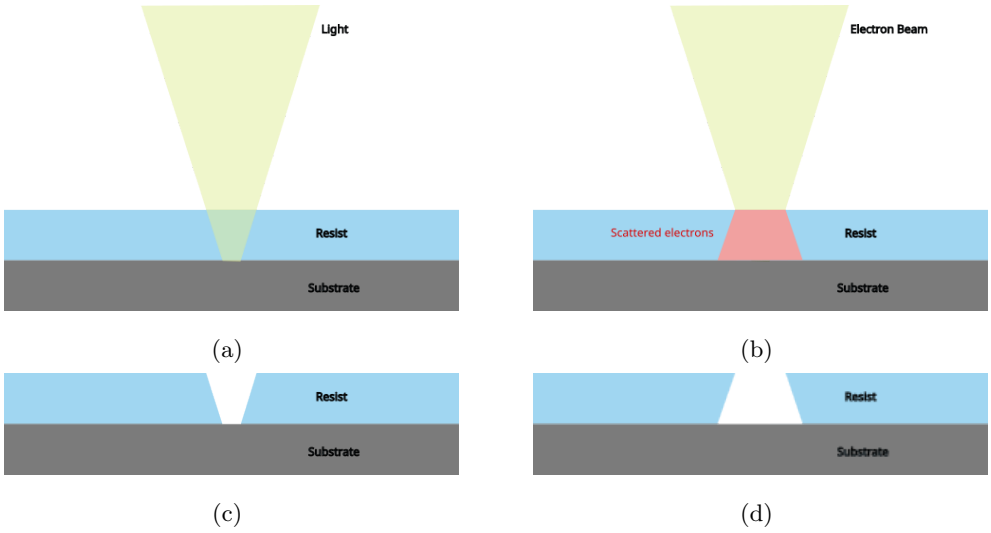

Figure 2.4: The different result using a positive resist for photolithography(a & c) and electron beam lithography(b & d).

This scattering effect also causes neighbouring spots of illumination leading to a higher dose on the neighbouring spots. This is a factor that influences the resolution of electron beam lithography, named the proximity effect [13]. This is counteracted by a proximity effect correction (PEC). A PEC simulates the electron trajectory in the simulated material stack using Monte Carlo simulations, and calculates a correction factor of the dose for each point in the exposure file. At NanoLab, the software Tracer is used to calculate the effect, and the software Beamer is used for data preparation for electron beam lithography, including a PEC using the data from tracer.

Figure 2.5: Workflow of creating layout files for EBL with Beamer and ELLIONIX

2.2.2 Etching

Etching is the process of removing materials using chemical and or physical reactions. Depending on the desired use-case, different etching techniques may be viable. When it comes to etching with respect to nanoscale fabrication, the following are properties that needs to be considered:

- **Anisotropy**: Some etching techniques etches equally fast in all directions. This is called isotropic etching. However, if features such as straight walls in a nanostructure is desired, it is desired that the etch only etches in one direction, leaving behind straight walls. This is called aniostropic etching.
- **Etch rate**: The etch rate determines how fast the etch process removes matter, and in turn decides how controllable the etch is. If the etch rate is fast compared to the feature size, it is

hard to get the desired etch depth. On the other hand, if the etch rate is too slow compared to the desired feature size, the etching will take unnecessary much of your time.

- **Selectivity**: The selectivity states how fast the target is etched compared to other materials, which likely is undesired to be etched. As an example, a selectivity of 3:1 states that for each three micron of the target that is etched away, one micron of the other material will also be etched.

In order to control the process, etch rate must be calculated before to know the etch time needed.

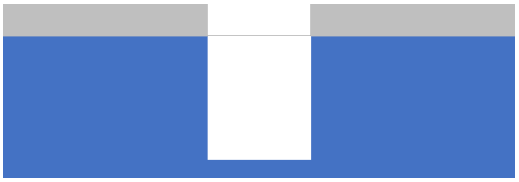

(a) Illustration of anisotropic etching. The etch only works in one direction, in this case downwards.

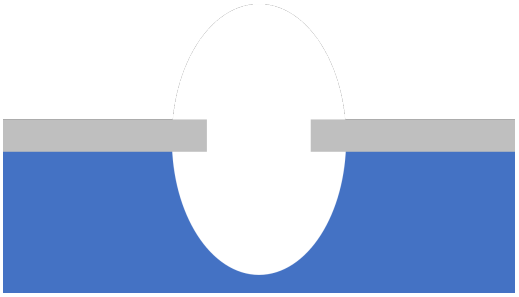

(b) Illustration of isotropic etching. The etch works equally in all directions, creating a spherical void

ICP-RIE

Inductively Coupled Plasma Reactive Ion Etching (ICP-RIE) is an etching technique that utilizes a combination of inductively coupled plasma (ICP) and reactive ion etching (RIE), which results in a controlled and highly anisotropic etch of a wide selection of targets. Inductively coupled plasma has a high electron density, which results in a high ionization degree without reaching high temperatures. Reactive gases are subsequently added, which will be ionized by the ICP, which in turn makes the reactive gases more reactive. The reactive gases flow towards the sample, effectively sputtering away matter from the substrate in an anisotropic way.

The main advantages of ICP-RIE is that it yields a highly anisotropic etching profiles, and it have a high selectivity. It also has controlled etch rates, which is of high importance when etching on a nanometer scale.

2.2.3 Thin film deposition

PECVD

Plasma Enhanced Chemical Vapor Deposition is a thin film deposition technique, which uses plasma to accelerate deposition reaction from precursor gases. PECVD begins with introducing the precursor gases, which through a chemical reaction will create the desired target material for the thin film. The reaction is subsequently enhanced by applying and RF field which turns the precursor gases into plasma. Since plasma has a high electronic density, it is highly ionizing which in turn enhances chemical reactions.

The resulting deposition rate can accurately be controlled by tweaking parameters such as gas composition, temperature, pressure and RF frequency. The deposition process is performed in a vacuum chamber, to ensure no pollution from chemicals and particles from the environment, leading to precise, uniform and high quality thin films.

PECVD also allows the user to control stress and strain in the resulting thin film, as well as uniformity and refractive index. Table show relation between process parameters and resulting thin film properties for SiN.

Some advantages of PECVD is

- Uniform thickness and conformal coating, even on irregular surfaces
- Low operating temperatures, which allows deposition on substrates that are temperature sensitive
- A wide range of materials to deposit, specifically which are hard to deposit using other deposition techniques.
- Deposition rate is relatively fast, compared to techniques such as ALD.

E-beam evaporation

Electron beam evaporation is a deposition technique mostly used for metals. An electron beam is directed towards a bulk of metal, referred to as the target?, with the use of a magnetic field. The metal is vaporized by the electrons, with the acceleration voltage needed to vaporize the metal being proportional to the melting point of the metal. The deposition rate is determined by the current used with the electron beam. The sample is covered by a protective "blanket" while the deposition rate is stabilizing, with a different sensor measuring the deposition rate. When the rate is stable, the blanket is removed, and the deposition runs until the desired thickness is reached, which is measured by a laser. The deposited layer will be uniform, since the vaporized metal atoms travels randomly through the vacuum and onto the substrate,.

Atomic layer deposition(ALD)

Atomic Layer Deposition (ALD) is a thin film deposition technique using sequential gas reactions in an alternating manner. ALD usually utilises two precursors, which react with the material surface in a self-limiting way, meaning that the reaction stops once all reactive sites on the substrate surface have created bond to the new layer. By repeating the deposition cycle, a thin film grows vertically, one atomic layer at a time.

Some advantages of ALD includes precise control of thickness, a wide range of possible materials to grow, and the ability to create thin-films with excellent uniformity, even on top of more complex structured substrates.

Spin Coating

By applying a fluid to a substrate, and rotating the substrate, the fluid will be exposed by a centripetal force which will distribute the fluid uniformly across the substrate. The thickness of the fluid is dependent of the rotation speed, as the total forces are the centripetal force by rotation, surface friction between fluid and substrate and internal inertia in the fluid. Using a aqueous solution of the desired material, one may easily evaporate the liquid using a hot plate or an oven, and the remaining material forms a uniform layer.

2.3 Characterization Techniques

2.3.1 Scanning Electron Microscopy (SEM)

Scanning Electron Microscopy (SEM) is an imaging technique that uses an electron beam to image the sample. This gives good information on surface morphology, topography and composition of materials on the sample.

Working operations: An electron beam is sequentially scanned across the sample, producing an image by measuring the reflected, scattered and re-emitted electrons. The image are assembled by an electron detector, which can detect two types of electrons: secondary electrons (SE) or back scattered electrons (BSE).

Back-scattered electrons are of high intensity, and are scattered with a small angle compared to the incident beam. BSE have a high interaction volume in the sample, which in turn allows this signal to carry information on sample composition deeper down in the sample.

Secondary electrons are electrons that scatter inside the sample before they are scattered out to the detector. These have a small interaction volume, and give rise to topological imaging, as they

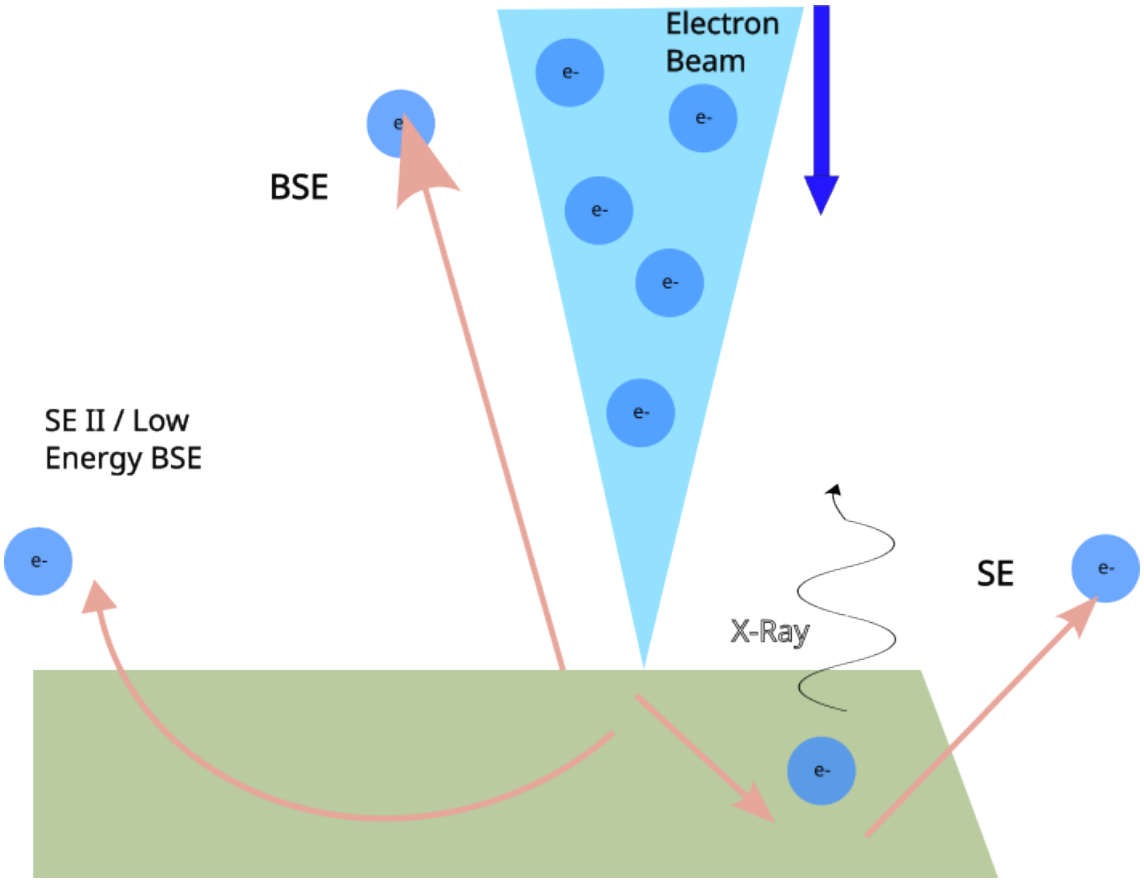

Figure 2.7: Different signals from SEM: Back scattered electrons are of the highest energy, secondary electrons are more present at edges, giving rise to contrast at topological features. X-rays are emitted as electrons scatter through the sample, giving material dependent wavelengths.

have a larger possibility to escape from the sample and scatter to the detectors at the edges.

As electrons scatter inside the sample, they may lose energy which is released as x-ray radiation. This radiation can also be captured and interpreted as a signal, resulting in information regarding material composition.

2.3.2 Reflectometer

The reflectometer at NanoLab, more specifically the F20, maps the reflection coefficient at an normal angle of incidence to a spectrum of wavelengths. Comparing this to theoretically calculated results, the software fits the measured data while adjusting one or several film thicknesses of the model, resulting in the best possible fit, with the resulting thicknesses of the model.The models used are calculated as described in section 2.1.5. This result in both the thickness of the layer, and the optical constants n and k of the thin-film

Spectral reflectance measures the amount of light reflected from a thin film over a range of wavelengths, with the incident light normal to the sample surface. Ellipsometry is similar, ex-

cept that it measures reflectance at non-normal incidence and at different polarization states

2.3.3 Ellipsometry

Ellipsometry is an optical analysis technique used to characterize thin films, surfaces and interfaces between materials. It can characterize material properties such as refractive index, and optical properties such as polarization state and wavelengths, both in reflection and in transmission through a sample.

In general, Ellipsometry relates the incoming polarization state to the outgoing polarization state, either by reflection or transmission, and results in a mathematical description on how the polarization-state is affected by the sample. Ellipsometry can measure the change in polarization state for a single wavelength, for a continuous spectrum of wavelengths, at different incident angles, at different scattered angles, or a combination of these parameters. Ellipsometry is categorized into several subcategories based on the variables of the measurement, including:

- **Variable angle of incidence**: The angle of incidence is changed at each measurement, with constant wavelength.
- **Spectroscopic**: The wavelength is changed for each measurement, with the angle of incidence held constant.
- **Variable angle and Spectroscopic**: Both angle of incidence and wavelength is varied.

Depending on spatially dependent optical properties of the analysed sample, different parameters are required to fully describe the how the sample affects the polarization state of the light. Ellipsometry can be modified to fit both a simple and more complex models of the samples, categorized into four subgroups, with different output as a sample description:

- **Standard**: Measures two parameters ψ and Δ, and outputs r_s and r_p, which are reflection coefficients (or transmission) for s and p polarized light respectively. Used for samples where there are no coupling between the p- and s- polarized states.
- **Generalized**: Measures at least six parameters; ψ_{ss}, Δ_{ss},ψ_{sp}, Δ_{sp},ψ_{ps} and Δ_{ps}. These are the same parameters as for standard ellipsometry, but there are separate parameters which describes how p-polarized states are transformed to s-polarized and vice versa. The output is the Jones matrix as described in section **??**. This is used for samples which couples s- and p- polarized states.
- **Mueller Matrix**: Measures all 16 parameters of a Mueller Matrix, as described in equation 2.76. By doing this, one can also describe the depolarizing effect of a sample.

- **Scattering**: Same amount of parameters as MM, but measures at scattered angles. Results in a bidirectional reflectance distribution function Mueller matrix (BRDF Mueller matrix).

Mueller Matrix Ellipsometry

As the method used in this thesis is a Spectroscopic Mueller Matrix in transmission, that will be further described.

In reflection ellipsometry, the polarization state is described by

$$\rho = \frac{r_p}{r_s} = tan\psi_r e^{i\Delta_r} \quad , \tag{2.74}$$

where r_p and r_s are the reflection coefficient for p and s- polarized light respectively, and Ψ_r and Δ_r are experimentally determined parameters, refereed to at the ellipsometric angles [7].

For generalised ellipsometry, the reflection coefficient is given by

$$r = \begin{bmatrix} r_{pp} & r_{ps} \\ r_{sp} & r_{ss} \end{bmatrix} \quad , \tag{2.75}$$

where r_{ps} describes how much of the p-state is converted to a s-state etc. To measure all these parameters, the incident light is fully polarized in one state, say s-state, and r_{sp} and r_{ss} is measured. Subsequently, the incoming light is a pure p-state, and r_{ps} and r_{pp} are measured.

In Mueller matrix ellipsometry, the 16 parameters that are measured are similar to the generalized case, but in addition to doing measurements with only s- and p- polarized light, polarization states

such as +45, -45, LCP and RCP. The Mueller Matrix elements are calculated as follows:

$$m_{11} = \frac{1}{2}(|r_{pp}|^2 + |r_{ss}|^2 + |r_{sp}|^2 + |r_{ps}|^2) \tag{2.76a}$$

$$m_{12} = \frac{1}{2}(|r_{pp}|^2 - |r_{ss}|^2 - |r_{sp}|^2 + |r_{ps}|^2) \tag{2.76b}$$

$$m_{13} = Re(r_{pp}r*_{sp}) + r_{ss}r*_{ps}) \tag{2.76c}$$

$$m_{14} = Im(r_{pp}r*_{sp}) + r_{ss}r*_{ps}) \tag{2.76d}$$

$$m_{21} = \frac{1}{2}(|r_{pp}|^2 - |r_{ss}|^2 + |r_{sp}|^2 - |r_{ps}|^2) \tag{2.76e}$$

$$m_{22} = \frac{1}{2}(|r_{pp}|^2 + |r_{ss}|^2 - |r_{sp}|^2 - |r_{ps}|^2) \tag{2.76f}$$

$$m_{23} = Re(r_{pp}r*_{sp}) - r *_{ss} r_{ps}) \tag{2.76g}$$

$$m_{24} = Im(r_{pp}r*_{sp}) - r *_{ss} r_{ps}) \tag{2.76h}$$

$$m_{31} = Re(r_{pp}r*_{ps}) + r *_{ss} r_{sp}) \tag{2.76i}$$

$$m_{32} = Re(r_{pp}r*_{ps}) - r *_{ss} r_{sp}) \tag{2.76j}$$

$$m_{33} = Re(r_{pp}r*_{ss}) + r *_{ps} r_{sp}) \tag{2.76k}$$

$$m_{34} = Im(r_{pp}r*_{ss}) - r *_{ps} r_{sp}) \tag{2.76l}$$

$$m_{41} = -Im(r_{pp}r*_{ps}) + r *_{ss} r_{sp}) \tag{2.76m}$$

$$m_{42} = -Im(r_{pp}r*_{ps}) - r *_{ss} r_{sp}) \tag{2.76n}$$

$$m_{43} = -Im(r_{pp}r*_{ss}) + r *_{ps} r_{sp}) \tag{2.76o}$$

$$m_{44} = Re(r_{pp}r*_{ss}) - r *_{ps} r_{sp}) \tag{2.76p}$$

Components of the system

The following components is also essential in an ellipsometer system:

- **Source**: A xenon lamp is used for a broad range of wavelengths.
- **PSG**: The Polarization state generator consist of a linear polarizer and a rotator. The linear polarizer generates linearly polarized light in in a specified direction. The rotator delays the phase of the s- or p- polarization, giving the possibility to create elliptical polarized light. With these two combined, it is possible to generate any desired polarization state.
- **PSD**: Polarization state detector works the same way as the PSG, but in opposite order. This allows the detection of the polarization state
- **Detector**: Can only measure the intensity, thus the need for a PSD to determine the intensity of each polarization state.

Advantages of ellipsometry is that it is comprehensive in its characterization, it is non-destructive and is very precise.

2.4 Simulations

2.4.1 Finite Difference Time Domain (FDTD)

Finite Difference time domain is a numerical technique used to simulate how electromagnetic radiation propagates through medium, such as reflection, transmission, scattering and refraction. It excels in simulating complex structures and meta-surfaces, with the drawback that it is much more computational demanding compared to methods such as RCWA and FEM.

FDTD discretizes both time and space, and for each time step every point in space will update its electric and magnetic field based on Maxwell's equations2.1 to 2.4. Derivatives are approximated using the central difference approximation. The update procedure can be described as follows:

1. **Update for Electric Field** (**E**):
$$\mathbf{E}_{i,j,k}^{t+1} = \mathbf{E}_{i,j,k}^{t} + \frac{\Delta t}{\varepsilon} (\nabla \times \mathbf{H})_{i,j,k}^{t+1/2}$$
2. **Update for Magnetic Field** (**H**):
$$\mathbf{H}_{i,j,k}^{t+1/2} = \mathbf{H}_{i,j,k}^{t-1/2} + \frac{\Delta t}{\mu} (\nabla \times \mathbf{E})_{i,j,k}^{t} \, quad,$$

where

- n is the current time step
- ε and μ are the permittivity and permeability of the material at the respective grid points. In this equation, they are simplified to a constant, but this is not the general case. A detailed explaining of how the dielectric permittivity is moddeled in FDTD thorugh the constitutive relations can be found in *Understanding the Finite-Difference Time-Domain Method*, chapter 10.2[14]
- i, j, k are the indices representing the spatial grid points
- Δt is the time step

This also takes advantages of a concept named Yee lattice. This is apparent in the 1/2 notation, as the lattice for the magnetic field values are shifted with 1/2 compared to the electric field lattice. In practise this allows for the electric and magnetic field to be updated simultaneously [14].

Courant-Friedrichs-Lewy (CFL) condition

The time-step (Δt) and the spatial resolution (number of grid-cells) are important parameters in FDTD simulations,and they are connected through the Courant-Friedrichs-Lewy (CFL) stability condition. This condition ensures the simulation is numerically stable:

The CFL stability criterion is given by[14]:

$$\text{CFL} = \frac{c \cdot \Delta t}{\Delta x}$$

where: - c is the speed of light in the medium. - Δt is the time-step. - Δx is the spatial resolution (grid cell size).

To obtain numerical stability, the CFL value should be less than or equal to a certain threshold, typically the square root of the number of dimensions, i.e. $\sqrt{3}$ for three-dimensional FDTD simulations. Therefore, the time-step (Δt) is constrained by the spatial resolution (Δx) through the CFL condition.

2.4.2 Analyzing FDTD Data

FDTD can return field values at every point at every time-step. However, this is a lot of data and often not every point and or time-step is of interest, so to reduce memory requirements and improve readability and insight, there are several ways of processing the data. ANSYS have many of these features built in. To save memory, one need to place specific types of monitors at desired location to retrieve and analyze the data from the simulation.

Far Field analysis

The far field domain is where the distance from the object of interest is much larger than the wavelength of light. In this area, the expressions and calculus tends to be much easier. As it is computational demanding to calculate the wave propagation to such distances, it is convenient to calculate the far-field from a measured near-field. This is done by performing a spatial Fourier transform on the measured field, then traversing numerically the wave in the Fourier space to the far field. This resembles the angular spectrum method covered in section 2.1.5. The intensity for each wavelength is then conserved, along with intensities along each polarization direction orthogonal to the direction.

$$E_{\text{far}}(\theta, \phi, r) = \frac{e^{ikr}}{r} \int_S \left[n \times H(r', t - r/c) - \frac{1}{c} \frac{\partial}{\partial t} (n \times E(r', t - r/c)) \right] e^{-ikr' \cdot \hat{r}} ds' \tag{2.77}$$

Finding the Mueller Matrix of the system

The Mueller matrix is found by doing the far field transform on the time domain signal from a monitor in the near field area. This is done in spherical coordinates, to find the diffracted angles of interest. Furthermore, at each diffracted order, equation 2.29. Since this equation requires data for both a x-polarized incoming wave and a y-polarized incoming wave, the simulation is run twice.

One time with x-polarized input, and one time with y-polarized input. Then, equation **??** is used to find the Mueller Matrix

Experimental Method

In previous research conducted at the Norwegian University of Science and Technology (NTNU), the Optics group led by prof. Morten Kildemo have designed and characterised amorphous silicon (a-Si) based polarimetric beam splitting metasurfaces[15]. The primary objectives of these studies were to characterise the manufacturing process and evaluate the quality of the metasurface [4] using ellipsometry. The initial goal of this thesis was to improve this design and manufacturing process to improve integrability with devices such as sensors and camera chips.

A key aspect of this refinement process was the integration of the metasurface design with a camera chip. This integration presented a challenge, as the illumination area considerably exceeded the metasurface area. Consequently, "unaffected" light could potentially interfere with the measurements. To address this issue, the integration of an aperture into the existing design was proposed, necessitating further process characterisation. An aperture for use with the existing samples were also manufactured.

However, the execution of this research was impeded by several challenges in the fall of 2023, primarily related to access to the necessary manufacturing and analysis equipment. The Inductively Coupled Plasma Reactive Ion Etching (ICP-RIE) equipment at NTNU NanoLab was removed for replacement during this period, rendering it unavailable for the duration of the thesis. Consequently, the a-Si process characterisation had to be concluded after the lithography step.

These circumstances led to the investigation of Gap Surface Plasmon (GSP) design, using the samples and processing steps developed at NTNU in 2018 by Walmsness et. al.[5] as a starting point. The metasurfaces was redesigned to achieve a greater angle of refraction and to correct a manufacturing error in the thickness of the dielectric layer to match the simulations used for the design. The greater angle of refraction would help with a sensor integration, to help separate the 1st order of refraction from the 0th order of reflection. Figure 3.1 illustrates how this integration with a camera could look like.

The replacement of the ICP-RIE also affected the availability of the Plasma Enhanced Chemical Vapor Deposition (PECVD) equipment, which was not accessible until January 2024. This lead

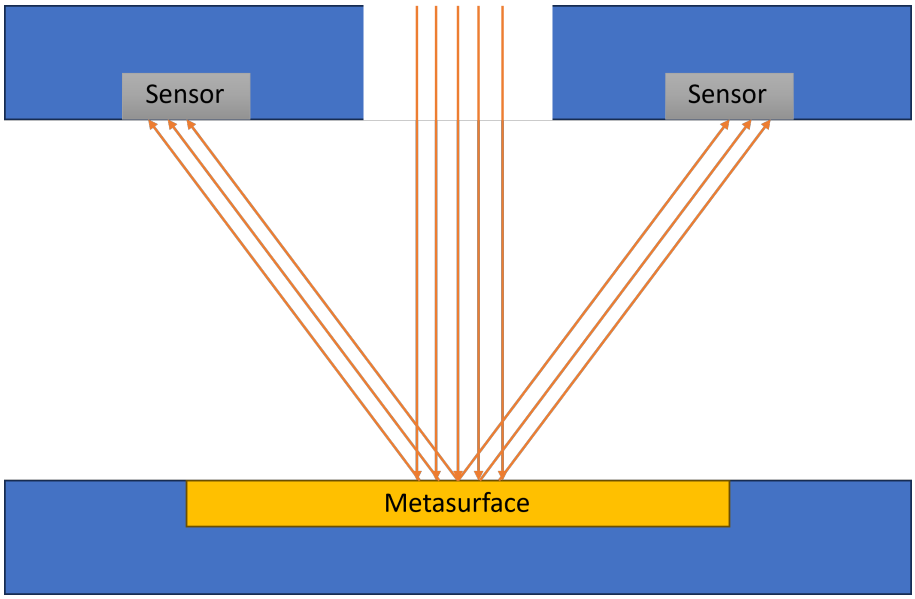

Figure 3.1: A possible layout for including the GSP metasurface with a camera sensor

to a delay in the GSP manufacturing process, which necessitated the exploration of an additional goal: the implementation of Mueller Matrix calculation and extraction from Finite-Difference Time-Domain (FDTD) simulation software ANSYS. This function was was implemented and verified by comparing the measured Mueller Matrices from [4], as well as simple wire grid polarizers. This function provides a valuable tool for both the design and analysis of optical metasurfaces. In particular, it allows for simulations of large, non-periodic structures. One future case of this is a polarisation splitting lens, which would require phase gradient spanning over many more meta-atoms, removing the periodicity of the structure.

It's also worth noting that the ellipsometer was also unavailable for a period of time, which unfortunately coincided with the critical stages of the project. In practice, this lead to no Mueller Matrix Ellipsometry measurements of the fabricated samples, as well as using a reflectometer for growth rate verification. Despite these challenges, the research made significant strides in the exploration of GSP samples and the use of FDTD simulations in the design process.

3.1 Metasurface Design

The focus of this thesis is the exploration of two types of metasurfaces: amorphous silicon (a-Si) based polarimetric beam splitting metasurfaces operating in transmission, and Gap Surface Plasmon (GSP) metasurfaces operating in reflection. The design of these metasurfaces have three primary considerations: the phase shift (δ_s, δ_p), the transmitted or diffracted angle and the transmission / reflection coefficient $(|t|^2/|r|^2)$. Both metasurfaces are a repetition of n-different meta-atoms, referred to as a super-period, and by adjusting the geometry of this superperiod we can control these parameters.

In order to achieve the polarisation state splitting, control of the phase shift of each meta-atom is essential. This phase shift can be tuned by adjusting the geometric parameters of the meta-atoms, and the materials of the metasurface. For polarization state splitting in opposing directions, this phase shift must trace a sawtooth wave pattern across each superperiod, with each sawtooth pointing in their respective direction.

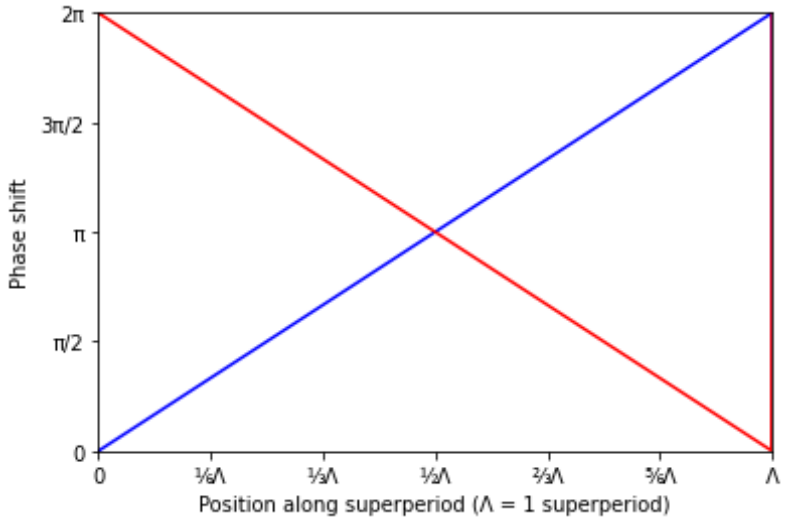

Figure 3.2: Illustration of a sawtooth phase shift, where each two lines represent the phase-shit in p-polarization δ_{pp} and in s-polarization δ_{ss}, which are of opposite direction.

The reflected or transmitted angle of light is controlled by the length of the superperiod and the phase shift across this superperiod. This length of the superperiod is controlled by either the number of meta-atoms in each super-period, or the distance between the meta-atoms. The diffracted angle from the metasurface is a result of both generalised Snell's law 2.37 and elemental diffraction theory, and is given by:

$$\theta = asin\left(\frac{\lambda \cdot \Delta\phi}{\Lambda \cdot 2\pi}\right) \quad , \tag{3.1}$$

and when considering a phase shift of $\Delta\phi = 2\pi$ in the superperiod becomes

$$\theta = asin\left(\frac{\lambda}{\Lambda}\right) \tag{3.2}$$

The optimization of the geometrical shapes of the meta-atoms within each superperiod was conducted for several different numbers of meta-atoms. This optimization was achieved using numerical simulations performed with the COMSOL Multiphysics software, with the aim of obtaining a correct phase shift (sawtooth profile across the superperiod) and an optimal transmission coefficient. These simulations were conducted by Morten Kildemo.

Both metasurfaces - techniques displays three different polarisation splitting metasurfaces, following the notation of Pors et. al. [16]. MS1 splits x and y linear polarized light, MS2 splits +45 and

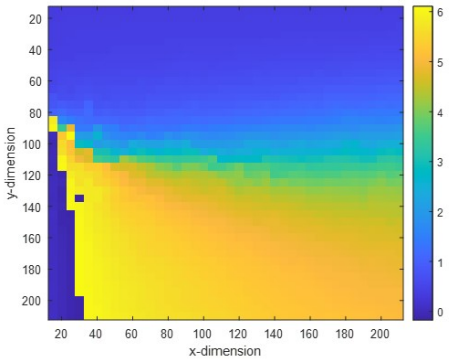

(a) Phase shift δ_p for different dimensions x,y of the gold blazed meta-atoms

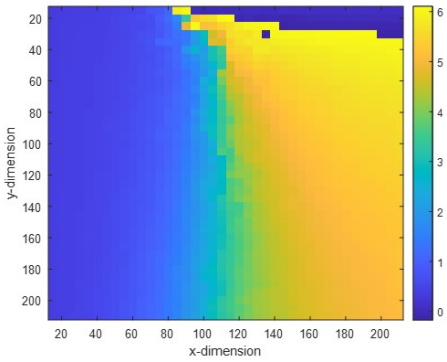

(b) Phase shift δ_s for different dimensions x,y of the gold blazed meta-atoms

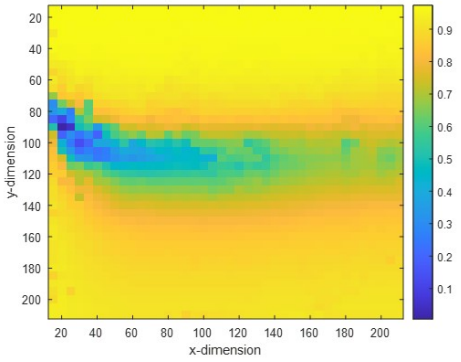

(c) Reflection coefficient r_p for different dimensions x,y of the gold blazed meta-atoms

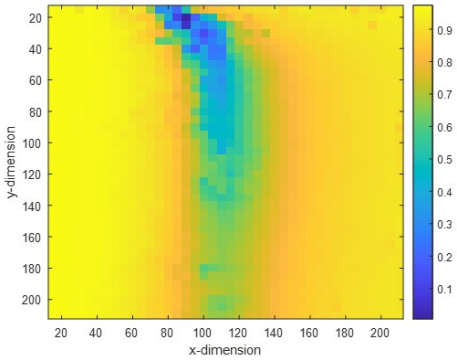

(d) Reflection coefficient r_s for different dimensions x,y of the gold blazed meta-atoms

Figure 3.3: Simulations of the phase shift and reflection coefficients for the meta-atoms of the GSP metasurface from COMSOL

-45 linear polarized light, and MS3 splits left circular polarized light and right polarized circular light.

MS3 function in a different way than MS1 and MS2. MS3 uses a Pancharatnam-Berry phase, also named a geometric phase. This phase is altered by a geometrical rotation, which leads to a movement of the polarisation state along a latitude in the Poincaré sphere. Thus, in MS3 the geometric shape of each meta-atom is the same, but in a super-period each meta-atom is subsequently rotated by π/n such that each super-period has a π rotation [17].

3.1.1 GSP

The gap surface plasmon (GSP) metasurface design is fundamentally separated into two key objectives: reflecting light to a specific diffracted angle θ, and splitting two distinct polarisation states to the $\pm\theta$ angle. This angle theta is given by equation 3.2.

To differentiate the two polarisation states, the metasurface requires a phase profile that presents a saw-tooth pattern in their designated direction. The GSP facilitates the independent manipulation of phase profiles in the x and y directions by adjusting the dimensions of the metasurface rectangles. The optimal dimensions were determined through COMSOL simulations, which provided the ideal geometry for metasurfaces with 5 (5P) and 6 (6P) meta-atoms per super-period. These geometries are summarised in table 3.1. Keep in mind that MS2 is rotated by an angle of 45 °, and MS3 has the same dimension for each meta-atom, where each meta atom is rotated $\frac{\pi}{n}$ from the previous meta-atom, where n is the number of meta-atoms per super-period. Each meta-atom is distanced by 320 nm, resulting in a total period of 1600 nm and 1920 nm, and thus calculated reflected angles of 30° for 5P and 24.6° for 6P, for the designed wavelength of 800 nm by the use of equation 3.2.

Table 3.1: Dimensions of each meta atoms for MS1, MS2 and MS3 in GSP metasurfaces with 5 and 6 meta-atoms per super-period

Meta Surface	**Meta Atom**	**X Dimension (nm)**	**Y Dimension (nm)**
5P MS1 & MS2	1	45	190
	2	100	155
	3	125	125
	4	155	100
	5	190	45
6P MS1 & MS2	1	40	195
	2	95	165
	3	120	135
	4	135	120
	5	165	95
	6	195	40
MS3 5P	*	100	195
MS3 6P	*	100	195

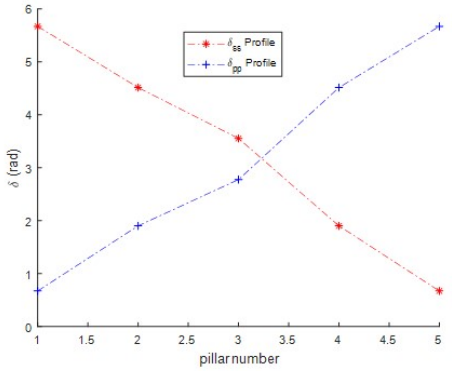

(a) Simulated phase shift δ_{ss} and δ_{pp} for the 5P GSP metasurface

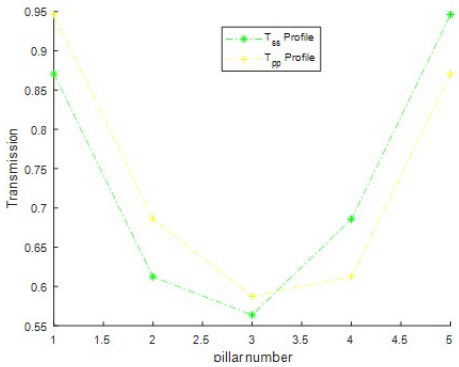

(b) Simulated transmission T_{ss} and T_{pp} for the 5P GSP metasurface

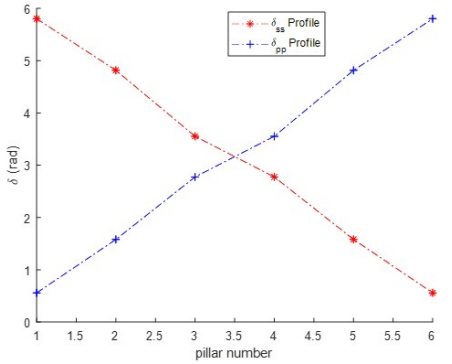

(c) Simulated phase shift δ_{ss} and δ_{pp} for the 6P GSP metasurface

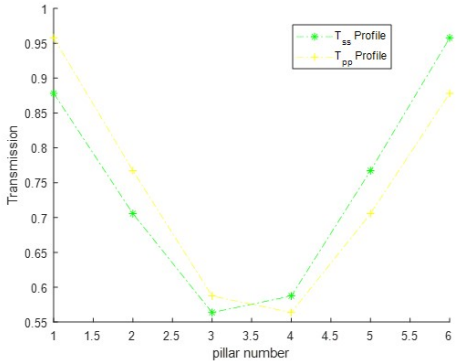

(d) Simulated transmission T_{ss} and T_{pp} for the P GSP metasurface

Figure 3.4: Simulated phase shifts and transmission coefficient for the 5P and 6P metasurfaces

The fabrication of these structures started with the deposition of a gold layer, serving as an optical mirror. Gold exhibits good optical properties, ideal for generation of GSP. However, gold's adhesion to the available crystalline wafer substrate and SiO2 (which acts as a transparent, separating insulator) is subpar. To improve adhesion, a 5 nm layer of titanium (Ti) is deposited both before and after the gold layer. Ti readily oxidises to TiOx, providing a smooth transition from SiO2 to Ti. Ti adheres well to both silicon and gold, with minimal impact on the layer's conductivity.

The SiO2 layer thickness is set at 50 nm, which ensures the layers are separate yet close enough for the induced plasmons to interact. A 50 nm distance has proven effective in previous studies, so it is used here as well.

The geometry of the meta-atoms in the final layer is shaped using lithography. A positive resist is employed to carve out the structures, followed by gold deposition and a lift-off, leaving behind the meta-atoms. A 5 nm Ti layer is inserted between the SiO2 layer and the gold layer to enhance adhesion, which is crucial to prevent the meta-atoms from being removed during the lift-off process if the adhesion is insufficient. This manufacturing process is illustrated with figure 3.6.

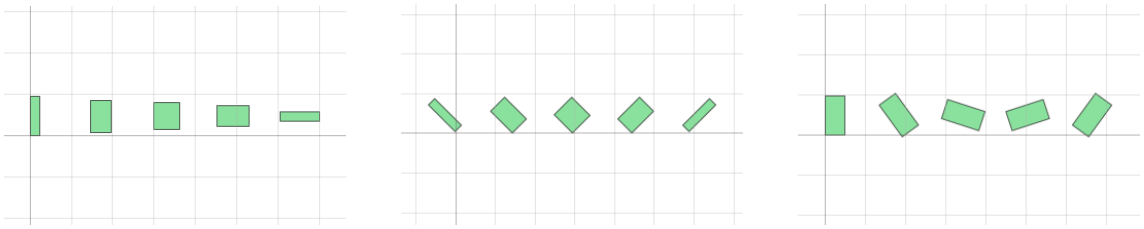

(a) Illustration of the MS1 superperiod for 5 meta-atoms (5P)

(b) Illustration of the MS2 superperiod for 5 meta-atoms (5P)

(c) Illustration of the MS3 superperiod for 5 meta-atoms (5P)

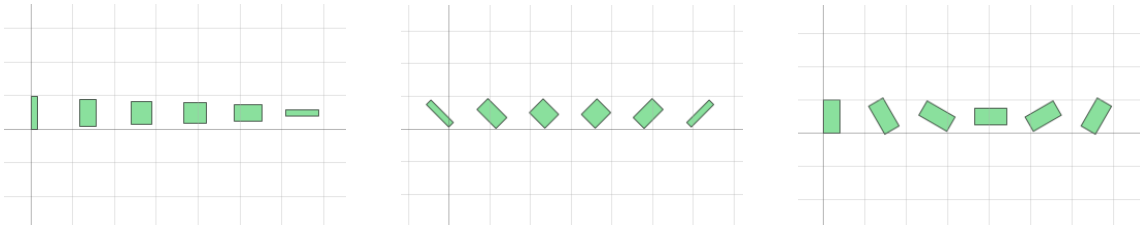

(d) Illustration of the MS1 superperiod for 6 meta-atoms (6P)

(e) Illustration of the MS2 superperiod for 6 meta-atoms (6P)

(f) Illustration of the MS3 superperiod for 6 meta-atoms (6P)

Figure 3.5: Illustrations of the GSP superperiod of MS1, MS2 and MS3 for 5P and 6P samples

3.1.2 a-Si Pillars

The design of these pillars uses the foundation of the previously manufactured samples, and tries to correct the thickness of the a-Si layer, and adding an aperture. Chromium was selected for the aperture material, as it is not transparent at the designed wavelengths, and it is resistant to the ICP-RIE etch used in the manufacturing process, as it is specifically used as a hardmask in the process. Chromium is also cheap compared to Au, Ti and other suitable metals. The thickness of this aperture layer needs to be sufficient to prevent oxidisation of the entire layer, as CrO becomes transparent for the wavelengths in question. 200 nm was determined thick enough to prevent total oxidisation.

The geometries of the elliptical pillars are summarised in table 3.2 and each super-period is illustrated with figure 3.7. Keep in mind that MS2 is rotated by an angle of 45 °, and MS3 has the same dimension for each meta-atom, where each meta atom is rotated $\frac{1}{n}\pi$ from the previous meta-atom, where n is the number of meta-atoms per super-period. Each meta-atom is distanced by 500 nm, resulting in a total period of 6 μm, thus a calculated diffracted angle of 8.7° for the designed wavelength of 915 nm by the use of equation 3.2.

The substrate used to manufacture the metasurfaces are fused silica (SiO2), as it is transparent for the wavelengths the device is designed for. To create the pillars of a-Si, a 715 nm layer of a-Si are grown on top of the fused silica substrate, and then the pillars are etched out. To etch the pillars, a lithography process is performed to create the geometrical structure of the pillars, and a Cr hard

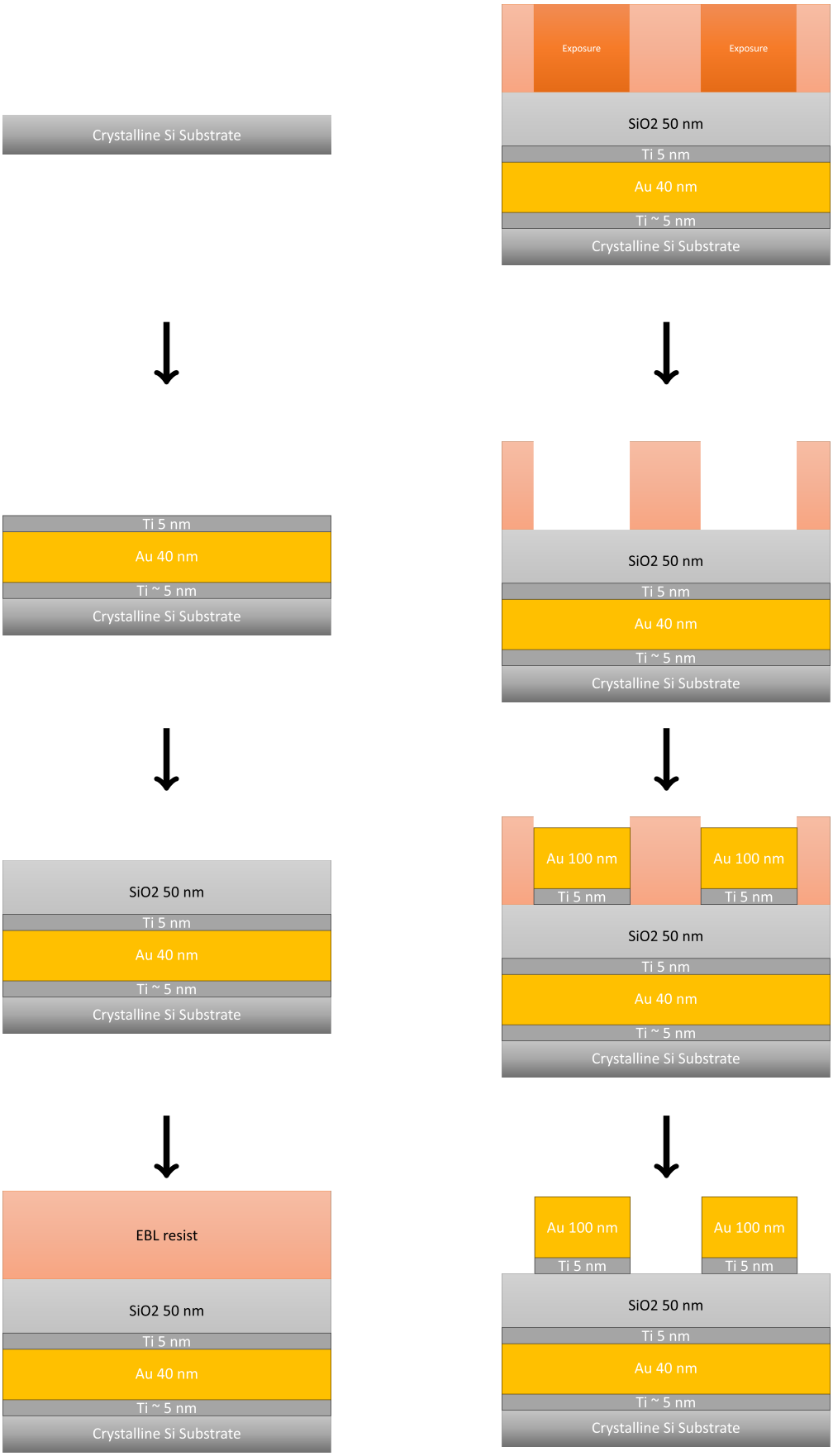

Figure 3.6: Illustrative overview of the manufacturing process to create the GSP samples. Not to scale

Table 3.2: Elliptical radii of each meta atoms for MS1, MS2 and MS3 in the a-Si pillar metasurface with 12 meta-atoms per super-period

Meta Surface	**Meta Atom**	**X - elliptical radii (nm)**	**Y - elliptical radii (nm)**
12P MS1 & MS2	1	230	195
	2	250	185
	3	135	215
	4	155	200
	5	170	190
	6	175	185
	7	185	175
	8	190	170
	9	200	155
	10	215	135
	11	185	250
	12	195	230
12P MS3	*	165	250

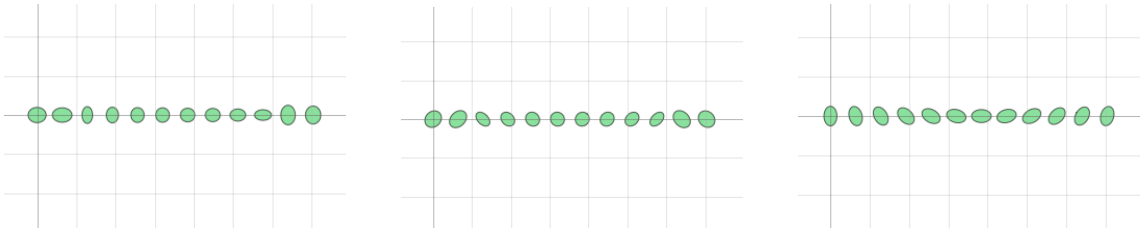

(a) Illustration of the MS1 superperiod

(b) Illustration of the MS2 superperiod

(c) Illustration of the MS3 superperiod

Figure 3.7: The designed superperiods for all three MS for the a-Si pillars.

mask of 13 nm is deposited. Then, another lithography process is performed, to create an aperture around the existing ellipses, to block out all light that does not pass through this device, for device integration purposes. Then the sample is etched to create the pillars. The manufacturing process are described in figure 3.8

Different materials to replace the a-Si were also considered. TiO2 is an attractive choice due to its high refractive index and excellent transparency in the visible spectrum. These properties make it particularly suitable for designing metasurfaces that operate in the visible range. However, one drawback of TiO2 is its relatively complex fabrication process, which may pose challenges in terms of cost and scalability. A manufacturing process using TiO2 is proposed and tested by Khorasaninejad et al. [18], which involves growing the pillars in an ALD, instead of etching out the pillars. This has its advantages as it is easier to create straight walls, but the ALD available

at NTNU does not allow photoresist inside the chamber, and NTNU also currently lack expertise in using the ALD for training and assistance.

Crystalline silicon (c-Si), on the other hand, offers a high refractive index and is widely used in the semiconductor industry, making it a well-understood and easily accessible material. However, unlike a-Si, c-Si is not transparent in the visible spectrum, which can limit its use in applications that require visible light transmission.

Zinc sulfide (ZnS) is another potential alternative. ZnS has a wide bandgap and is transparent across a broad spectrum, from the visible to the infrared range. This makes it a versatile material for metasurface design. However, the fabrication of high-quality ZnS metasurfaces can be challenging, and ZnS is also less compatible with standard semiconductor fabrication processes compared to a-Si or c-Si, and sulphur is generally not favoured due to heath concerns.

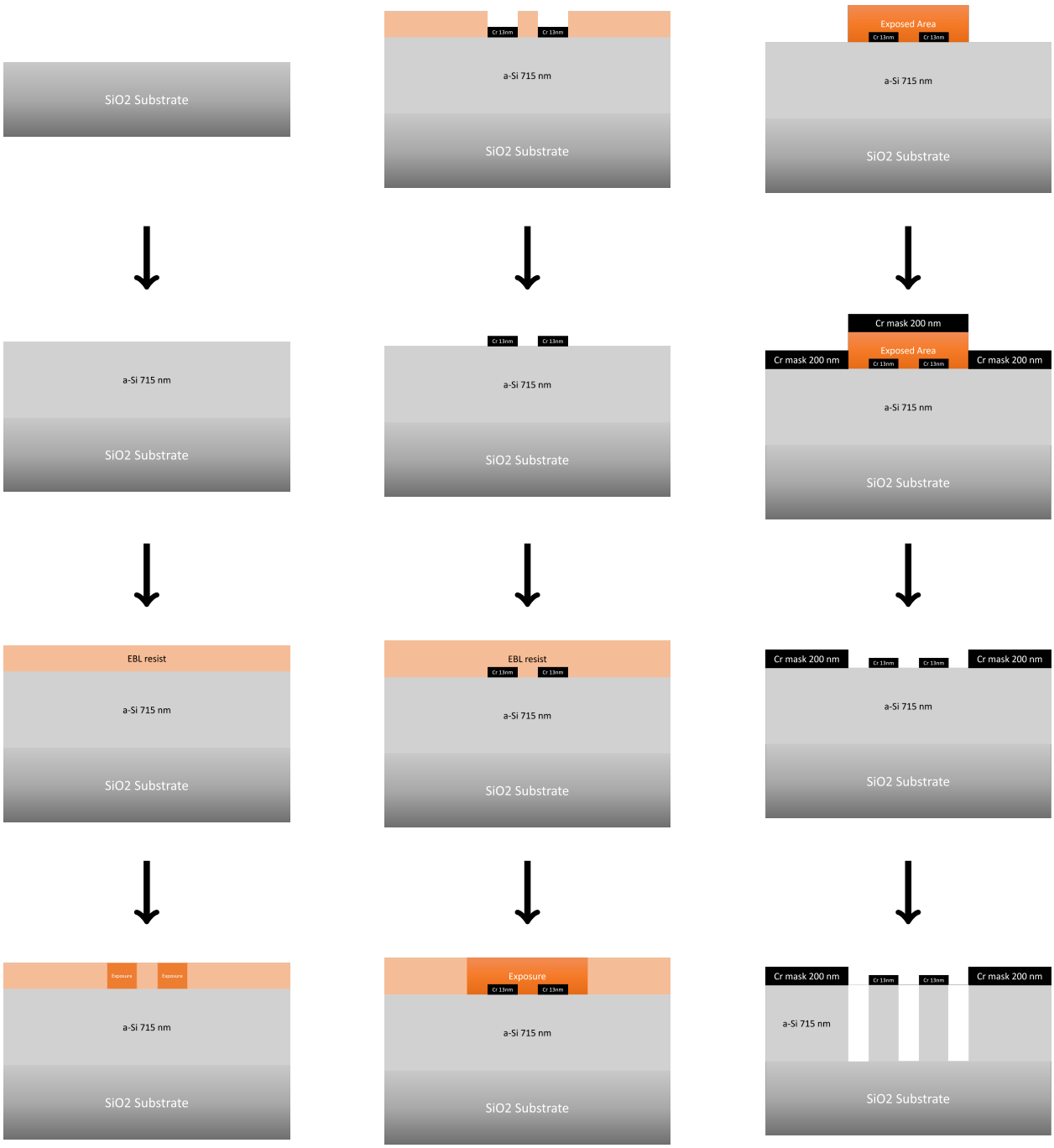

Figure 3.8: Overview of the manufacturing process of the a-Si pillar metasurface, with an aperture

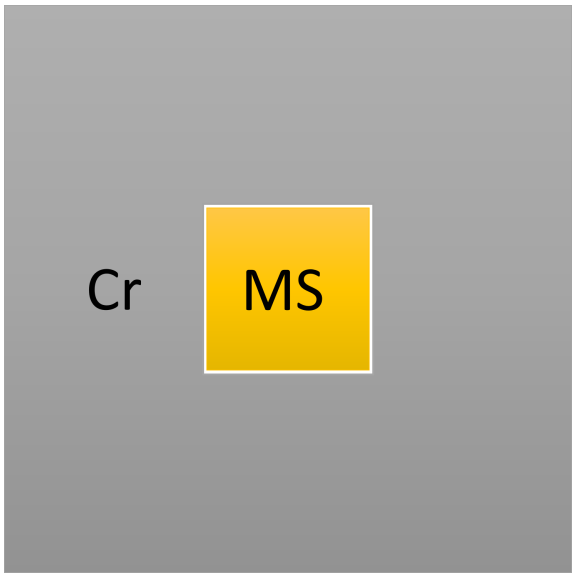

Figure 3.9: Illustration of the a-Si metasurface design with an integrated aperture, seen from above

3.2 Fabrication

3.2.1 Process characterization

To ensure comprehensive control over the manufacturing process and to mitigate potential errors, thereby achieving an optimal outcome, each process step was independently tested and characterized. This approach facilitated hands-on practice with the instruments and enabled the optimization of process parameters. Moreover, it minimized the potential for wasted effort, as an error in a complex structure process could necessitate the complete discard of all samples, requiring a restart from the beginning. By isolating each step, we were able to identify and rectify issues in a targeted manner, thus enhancing the overall efficiency and quality of the manufacturing process.

Dose test of CSAR 62.09

The CSAR 62 is a positive resist used for electron beam lithography, and will be used for both the a-Si metasurfaces and the GSP metasurfaces. CSAR 62.09 is a pre-diluted version of CSAR 62 with a 9% solids content[19]. There are several parameters such as thickness and dose that determines the final resolution, and these parameters were characterized here:

Following the eight steps of lithography, the procedure for using the positive resist CSAR 62.09 were as follows:

1. **Vapor priming**: The substrate is cleaned with acetone, followed by isopropanol, and drying using nitrogen. Then the substrate is exposed with UV-light for 5 min, before 1 min of

dehydration on a hotplate at 150 °C

2. **Spin Coating**: The resist used is the *ALLRESIST AR-P 6200.09*(CSAR 62), which is a postive EBL resist is used. This resist is spincoated for 60 seconds, with an acceleration of 1000 rpm/s and a max rotation of 4000 rpm, in order to reach a thickness of 200 nm.
3. **Soft bake**:The resist is soft baked at 150 °C for one minute on a hotplate.
4. **Exposure**:Exposed using the EBL. Dose test firs, then deside dose. Beam current?
5. **Post exposure bake is not needed**
6. **Development**: Using Allresists developer AR 600-546, one minute development in this followed by 30 sec in isopropanol bath to stop the development. Drying using nitrogen and 1 min hotplate bake at 130 °C follows.
7. **Sample inspection**

The process is first tested on a Si wafer, with a design of a 9 by 9 grid of ellipses ranging from width 50 nm to 250 nm in both elliptical axis. This pattern is again repeated on a 4 by 4 grid, rendering 16 identical areas, where each area will be exposed to a different dose time, in order to find the optimal dose. The sample is subsequently developed, and examined with an SEM to look for overexposure and underexposure. The beam current is set to 500 pA, which results in a beam diameter of 2.1 nm, and a step size of 0.5 nm with a feed and scan pitch of 4.

Dose test of ma-N 2405 on SiO2, for additional Cr apperture

In order to create an aperture, a negative resist is desired. This process was not included by Niklas et al [15], and is an entirely new addition to the a-Si metasurface manufacturing process. The only negative resist available for EBL were the ma-N 2405[20], and following is the lithography process for finding the optimal dose.

1. **Vapor priming**: The substrate is cleaned in an acetone bath, followed by an isopropanol rinse when the substrate is lifted from the acetone, to prevent the acetone to dry and form a thin layer on the sample. The sample is then dried using nitrogen, followed by ozone cleaning by exposure of UV light in an oxygen enriched environment. Finally a 1 minute dehydration on a hotplate at 150 °C is performed to evaporate all remaining humidity on the substrate.
2. **Spin Coating**: The negative resist used is the *ma-D 2405*, which is a negative resist both for UV lithography and electron beam lithography. This provides some challenges, as the EBL is located outside the lithography area of NanoLab which has special lighting to avoid exposure of UV sensitive resist. Bringing the resist to normal light as in the EBL area exposes the entire resist, leading to no pattern transfer. Another issue encountered here was that the

substrate used for the testing was SiO2, which is non-conductive and causes a charge build up during the electron beam exposure. This decreases the resolution of the pattern transfer, and may also deflect the electron beam leading to no pattern transfer at all. The solution to both these problems is to add a protective and conductive coating on top of the resist. This both protects the resist from UV light and makes the surface conductive, preventing charge build-up on the surface.

3. The ma-N 2405 was spincoated at 3000 rpm for 30 s, with an acceleration of 1000 rpm/s, giving a thickness of about 500 nm.

4. The resist is soft baked at 90 °C for 90 seconds on a hotplate.

5. Then the protective coating *Protective Coating Electra 92*(AR-PC 5092) was spincoated at 2000 rpm for 60s, with an acceleration of 500 rpm/s, followed by a bake at 90 degrees for two minutes.

6. Due to the larger feature size required when using a negative photoresist, the beam current were set to 10 nA, which gives an beam size of 10 nm. The write field were set to 1000 um, with 500 000 dots. The feed pitch and scan pitch were both set to 4, and the dose test revealed and optimal dose of 350 uC/cm^2, giving a calculated dose time of 0.0136 us/dot.

7. **Post exposure bake is not needed**

8. **Development**: Due to the protective coating Electra 92, the development consists of two parts; first to remove the protective coating and then to develop the resist. The coating Electra 92 is removed by one minute bath in DI water. The development of the resist was then determined to one minute in the developer ma-D 332, followed by a 2 minute bath in DI water.

9. **Sample inspection** Again due to the large feature size of the samples, the result could be inspected in an optical microscope.

Metal deposition

Given the deposition techniques accessible at NTNU, electron-beam evaporation was selected as the method of choice. for metallic thin-film deposition. This decision was driven by the excellent uniformity of the produced thin-films, the sub-nanometer control over the thickness, and the relative rapid deposition rates.

200 nm of chromium, which later will be used as both a hardmaskand the aperture, were deposited on a crystalline Si wafer. The resulting thin film were inspected in both SEM and with optical profilometry, in order to determine surface roughness and to verify the thickness of the thin film.

Deposition thickness and surface roughness were also tested for titanium on crystalline silicon, gold on crystalline silicon, and titanium followed by gold on crystalline silicon. The desired titanium thin film thickness was 5 nm, and the desired gold thin film thickness was 20 nm. Both the resulting thickness and surface roughness of these thin films were measured with an ellipsometer, including a cleaned crystalline silicon wafer for reference.

All deposition was performed on cleaned crystalline silicon wafers. The cleaning procedure was an acetone bath followed by IPA rinse, as acetone can leave contamination if allowed to dry on a sample. Ozone cleaning with additional oxygen was then performed for three minutes at 30 °, before one minute bake on a hotplate were performed to evaporate remaining droplets etc.

Lift off

Given that a lift-off procedure is an important step in both metasurface fabrication processes, the lift-off procedure was specifically optimized for use with CSAR 62.09, with a deposition of 13 nm Cr as the metallic layer, due to the low costs of Cr compared to Ti and Au also used in this theses. The success of a lift-off procedure can be characterized by distinct edges between metallic and non-metallic areas, along with the absence of residual metallic particles on the sample.

A metallic lift-off procedure using chromium was executed on a crystalline silicon wafer. This procedure followed the same steps and layout as those used in the dose test. After exposure and development, the sample was coated with a 13 nm chromium thin film. Subsequently, a lift-off process was performed using the remover AR 700-671, and the results were inspected using Scanning Electron Microscopy (SEM).

Two variations of the lift-off process were tested: one involving only the AR 700-71 followed by a deionized water rinse, and the other involving the AR 700-71 in an ultrasonic bath, followed by rinses with acetone and isopropyl alcohol (IPA).

a-Si and SiO2 deposition

For the deposition of the a-Si and SiO2 thin films, Plasma Enhanced Chemical Vapor Deposition (PECVD) was selected as the method of choice. Several factors contributed to this decision.

Firstly, PECVD is known for producing highly uniform films, which is critical for the performance and reliability of the metasurfaces. The uniformity of the film thickness ensures consistent optical properties across the entire metasurface, leading to predictable and reproducible results.

Secondly, PECVD is relatively easy to use. The process is automated and can be controlled with high precision, reducing the potential for human error and ensuring consistent quality of the deposited films.

Thirdly, PECVD does not involve the use of hazardous chemicals, making it a safer and more environmentally friendly option compared to some other deposition methods. This also simplifies the handling and disposal of waste materials.

Lastly, PECVD offers rapid deposition rates, which can significantly reduce the manufacturing time. This is particularly beneficial for large-scale production, where efficiency and throughput are key considerations.

By the use of PECVD, both a-Si and SiO2 were deposited on crystalline silicone wafers in order to determine the deposition rate. The first step was a conditioning step, where a deposition on a dummy wafer were performed for 5 minutes, such that the system could stabilize, and minimize the chances of contaminating gasses being present.

SiO2 For the SiO2, the datasheet of the PECVD suggested that the deposition rate were approximated to be at least higher than 50 nm/minute. As the target thickness was 50 nm, one film were deposited for one minute, and another were deposited for 90 seconds. The two films were measured using the thin film analyzer of NanoLab. This data was used to calculate the final deposition rate.

a-Si For the a-Si, the datasheet of the PECVD suggested that the deposition rate were approximated to be 25 nm/minute. As the target thickness of the a-Si layer were 715 nm, the two films were grown for 20 minutes and 30 minutes. These films were also measured using NanoLab's thin film analyzer, and the data were used to calculate the deposition rate.

3.2.2 Chromium aperture

The aperture was crated on slides of laboratory glass. A negative resist is used in the lithography, as this requires less time, since the metal will most of the sample. While this leads to an undercut, and following a worse result later from the lift-off, this was not weighted much due to the relative large size and margin of error in the aperture.

As the existing samples were manufacturing with two different sizes in area, one 650 µm x 650 µm and one 550µ x 550µm, apertures to match both these were created on the same substrate, numbered to be able to identify which aperture is which size. Inserting these dimensions into equation 2.48 shows that diffraction from the apertures are negligible, and all rays follows geometric optics.

Lithography

1. **Vapor priming**: The substrate is cleaned in an acetone bath, followed by an isopropanol rinse when the substrate is lifted from the acetone, to prevent the acetone to dry and form a

Figure 3.10: Aperture Layout

thin layer on the sample. The sample is then dried using nitrogen, followed by ozone cleaning by exposure of UV light in an oxygen enriched environment. Finally a 1 minute dehydration on a hotplate at 150 °C is performed to evaporate all remaining humidity on the substrate.

2. **Spin Coating**: The negative resist used is the *ma-D 2405*, which is a negative resist both for UV lithography and electron beam lithography. This provides some challenges, as the EBL is located outside the lithography area of NanoLab which has special lighting to avoid exposure of UV sensitive resist. Bringing the resist to normal light as in the EBL area exposes the entire resist, leading to no pattern transfer. Another issue encountered here was that the substrate used for the testing was SiO2, which is non-conductive and causes a charge build up during the electron beam exposure. This decreases the resolution of the pattern transfer, and may also deflect the electron beam leading to no pattern transfer at all. The solution to both these problems is to add a protective and conductive coating on top of the resist. This both protects the resist from UV light and makes the surface conductive, preventing charge build-up on the surface.

3. The ma-N 2405 was spin-coated at 3000 rpm for 30 s, with an acceleration of 1000 rpm/s, giving a thickness of about 500 nm.

4. The resist is soft baked at 90 °C for 90 seconds on a hotplate.

5. Then the protective coating *Protective Coating Electra 92*(AR-PC 5092)[21] was spin-coated at 2000 rpm for 60s, with an acceleration of 500 rpm/s, followed by a bake at 90 degrees for two minutes.

6. Due to the larger feature size required when using a negative photoresist, the beam current were set to 10 nA, which gives an beam size of 10 nm. The write field were set to 1000

um, with 500 000 dots. The feed pitch and scan pitch were both set to 4, and the dose test revealed and optimal dose of 350 uC/cm^2, giving a calculated dose time of 0.0136 us/dot.

7. **Post exposure bake is not needed**

8. **Development**: Due to the protective coating Electra 92, the development consists of two parts; first to remove the protective coating and then to develop the resist. The coating Electra 92 is removed by one minute bath in DI water. The development of the resist was then determined to one minute in the developer ma-D 332, followed by a 2 minute bath in DI water.

9. **Sample inspection** Again due to the large feature size of the samples, the result could be inspected in an optical microscope.

Metal deposition and lift-off

200 nm of Cr were deposited with the e-beam evaporator. Lift-off were performed with the stripper mr-Rem 700 for 3 minutes, using ultrasonic bath.

Optical imaging

An optical microscope were used to verify a successful fabrication, prior to any measurements. Due to the size of the aperture, inspection without a microscope also gave indication of a successful creation of apertures, as it was possible to see through the apertures.

Measurements

The efficiency of the apertures were measured using spectroscopic ellipsometry (SE). Two beam sizes of the incoming light beam were used, and both apertures were measured, in addition to a free space reference and a glass substrate reference. These measurements were carried out by Professor Kildemo.

3.2.3 GSP Nanostructures

Two 2" crystalline silicone wafers were used as substratea.

First metal deposition

The initial step of creating the GSP structures was depositing 5 nm titanium, followed by 40 nm gold and another 5 nm of titanium. As the accuracy of the e-beam evaporator were within

the accepted range, both for gold and titanium, no measurements were performed on to verify the thickness these layers. Prior to the deposition, the silicon wafers were cleaned with the same procedure as described in the lithography dose-test step. The two wafers both fit in the deposition chamber simultaneously, such that the deposition were performed simultaneously for both wafers. This is also a substantial cost saving, as the prices of high purity gold was around 1000 NOK/gram, and the deposition process in the e-beam evaporator uses about one gram to warm up and stabilize the deposition rate, and another half a gram for the actual deposition.

SiO2 deposition

The samples were again rinsed, as the time between the metal deposition and the SiO2 deposition were substantial such that the samples could have been contaminated. The PECVD were again put through a conditioning step, 5 minute deposition on a dummy wafer, before the first sample were inserted to deposit for 40 seconds, as the deposition rate were found to be 75 nm/minute. The sample were then measured with the thin film analyzer, such that possible adjustments could be done to the deposition time for the second wafer. The second wafer were also measured with the thin film analyzer to verify the thickness of the film.

Lithography

The initial step in the lithography step was the data preparation. An area of approximately 80 µm x 80 µm of the different GSP pattern, as described in **??**, were generated in Python using the open source package Phidl. The code for this generation can be found in appendix **??**. The small areas were expanded using the software Beamer, in order to avoid a single file for each rectangle, and to improve efficiency compared to generating the full MS areas in python. Each MS area were expanded such that the full area covered between 1 mm and 1.5 mm in each direction, as this was a trade off between matching the beam size of the ellipsometer, and the exposure time using EBL. For each number of structures per period, MS1, MS2 and MS3 were aligned with 1 cm between each area, such that the ellipsometer beam would not overlap several MS areas. A total of four different number of periods were designed, with all three metasurfaces for each. The final layout placed two of these periodicities on each wafer, with 1 cm separating the two arrays. Numbers were also added below, such that it would be easier to identify which metasurface is which. This is illustrated in figure 3.13

After designing the full exposure pattern for the two wafers, a proximity effect correction were performed (PEC). This was done using the software Beamer, which again uses an electron trajectory model created with the software Tracer, where electron trajectory for the full stack of materials were simulated. The final step of the data processing were to export the files, using a calculated dose time of 0.0282 mC/cm^2 This was calculated using the dose calculator of ELLIONIX, with

Table 3.3: Parameters for dose calculation of CSAR 62.09

Dose	285μC/cm2
Field size	200 000
Number of dots	50 000
Beam current	500 pA
Pitch	4

the following parameters inserted.

NOTE: No Healing were performed. Healing is the process of removing overlapping structures in the design files, such that no area is exposed twice and thus over-exposed. As there were no overlapping structures, and the healing process for this large amount of structures is very time-demanding, this step was skipped.

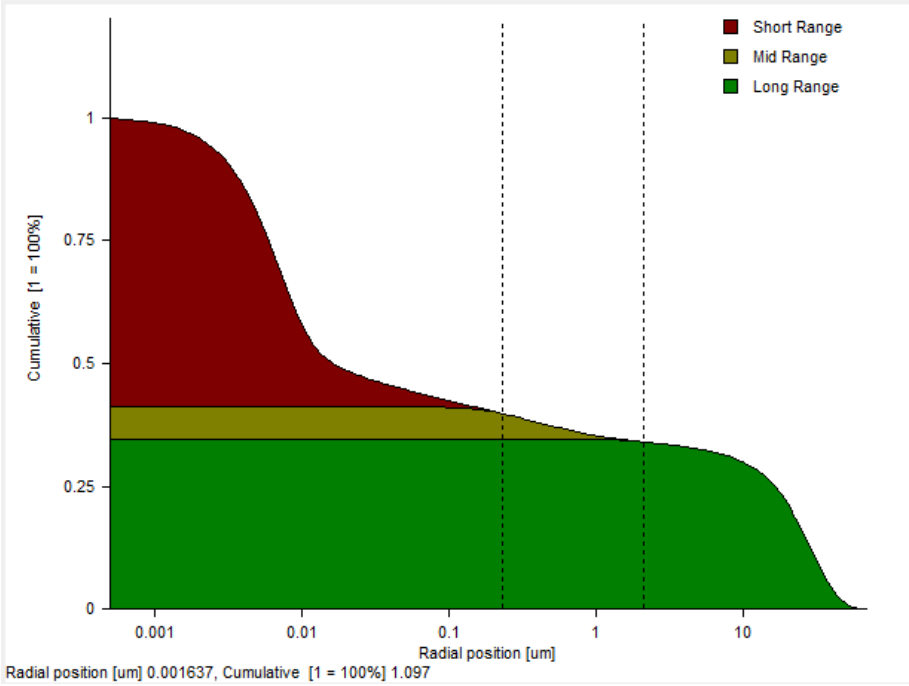

Figure 3.11: Output from Tracer simulations, showing the energy from the electrons scattering in the resist

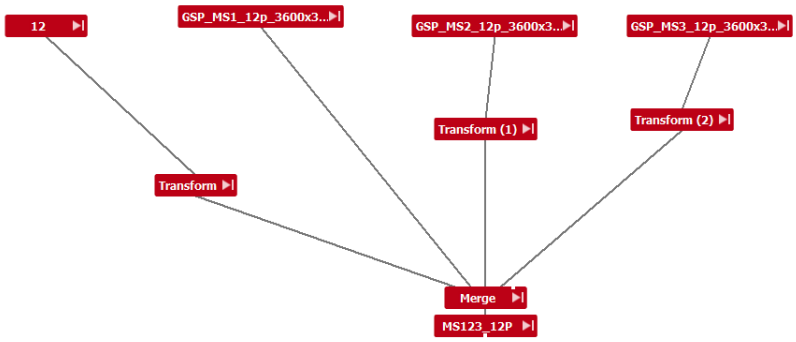

(a) Beamer workflow for creating a metasurface with Ms1, MS2 and MS3

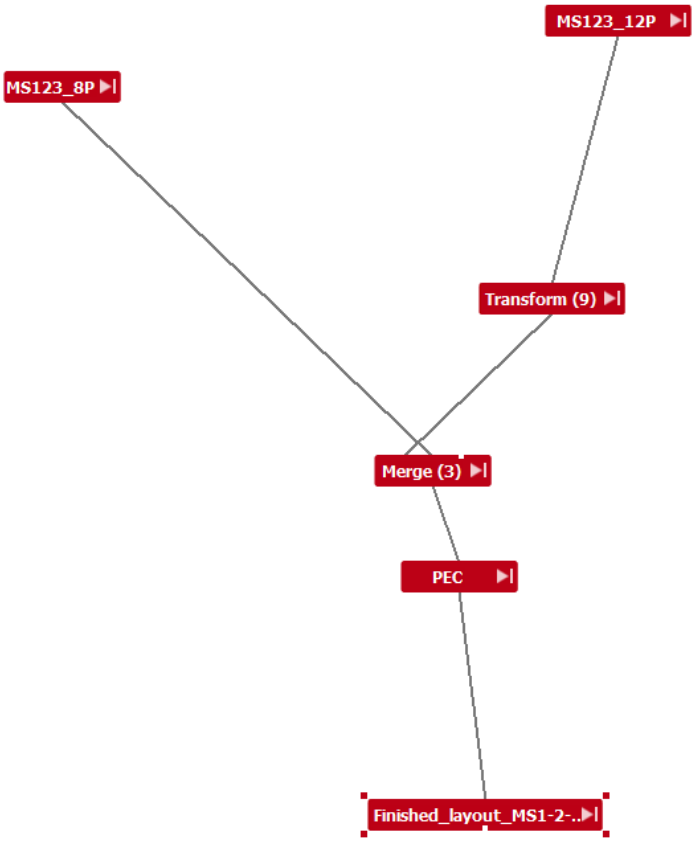

(b) Beamer workflow for merging two metasurfaces, to form the layout shown in figure 3.13

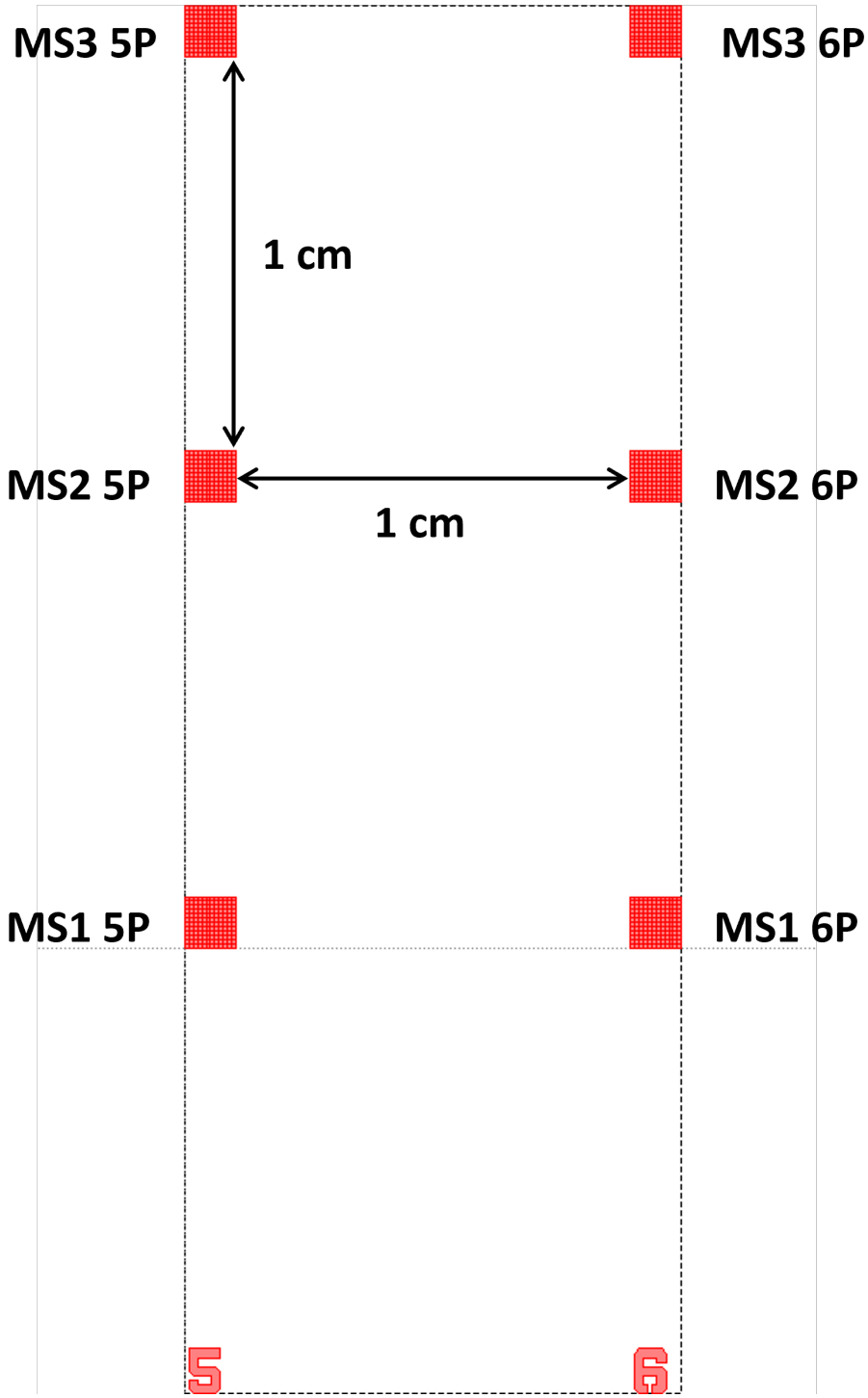

Figure 3.13: Layout of MS1, MS2 and MS3 for 5P and 6P in one combined exposure file

Transferring this data to the lab, the lithography process was performed with the same parameters as in the dose test. This was based on the assumption that the material stack of 5 nm Ti/ 40 nm Au/ 5 nm Ti/ 50 nm SiO2 would have the same adhesion and electrical conductivity as a clean c-Si wafer, such that no charging effect and the spin coat process would be the same:

1. **Vapor priming**: The substrate is cleaned with acetone, followed by isopropanol rinse, and drying using nitrogen. Then the substrate were exposed with UV-light for 3 min at 30 °C, and then 1 minute bake on a hotplate at 150 °C
2. **Spin Coating**: The resist used is the *ALLRESIST AR-P 6200.09*(CSAR 62), which is a positive EBL. The resist was spincoated for 60 seconds, with an acceleration of 1000 rpm/s and a max rotation of 4000 rpm. No conductive layer were used, as the thickness of 40 nm is negligible even though the SiO2 layer is insulating.
3. **Soft bake**:The resist is soft baked at 150 °C for one minute on a hotplate.
4. **Exposure**:The electron beam were set to 500 pA, and the system were allowed to settle with the new beam current. The beam current were measured and modified to an actual value of 500 pA, and the electron beam were focused and the stigmation were adjusted. The CON file were loaded, height set to 6,1 mm, and the tilt of the sample were measured to be? Write field alignment were performed and an estimate of the exposure time were calculated.
5. **Post exposure bake is not needed**
6. **Development**: Using Allresist's developer AR 600-546, one minute development in this followed by 30 sec in DI bath to stop the development. Drying using nitrogen
7. **Sample inspection** The sample were only inspected optically, and such one can only see the overall structure and the general outline of the metasurface areas. Any inspection in an electron microscope would affect the photoresist and possibly damage the structures and affect further processing

Second metal deposition and lift-off

The second metal deposition in the e-beam evaporator were 5 nm of titanium and 100 nm of gold. This was followed by lift-off, which were performed with the remover AR 600-71. The process were performed in an ultrasonic bath for 10 minutes, followed by an acetone bath and IPA rinse.

3.2.4 a-Si pillars fabrication

a-Si deposition

Two 4" wafers of fused silica were used as a substrate, and the deposition of a-Si were performed in two sequential processes. The deposition time were set to 35 minutes and 55 seconds, based on the initially measured deposition rate on c-Si substrates. After the first deposition, the thickness of the a-Si layer were measured using the reflectometer at NanoLab, and the deposition time were adjusted to 33 min and 6 seconds based on this measured thickness. The thickness of the second a-Si layer was also measured with the reflectometer.

Data preparation for EBL

The data preparation for EBL exposure were started, but were not completed due to technical challenges with the software and computer. This lead to a halt here, and the goal of processing until the etch step was not reached. The design is attached.

Highlighted difference from the GSP manufacturing is the need for alignment marks, to align the aperture and the metasurface areas, as these are created i two separate lithography processes.

3.2.5 Facilities and Instruments used

The following instruments were used for the different processes of manufacturing and characterization:

- **Cr, Ti and Au deposition** - Lesker e-beam evaporator at NTNU NanoLab
- **Electron Beam Lithography** - Elionix ELS-G100 at NTNU NanoLab
- **General lab facilities** - NTNU NanoLab
- **SEM** - FEI Apreo at NTNU NanoLab
- **a-Si and SiO2 growth** - PECVD at NTNU NanoLab
- **Reflectometer** - reflectometer F20 at NTNU NanoLab
- **Ellipsometry** - Self assembled setup by Morten Kildemo at NTNU

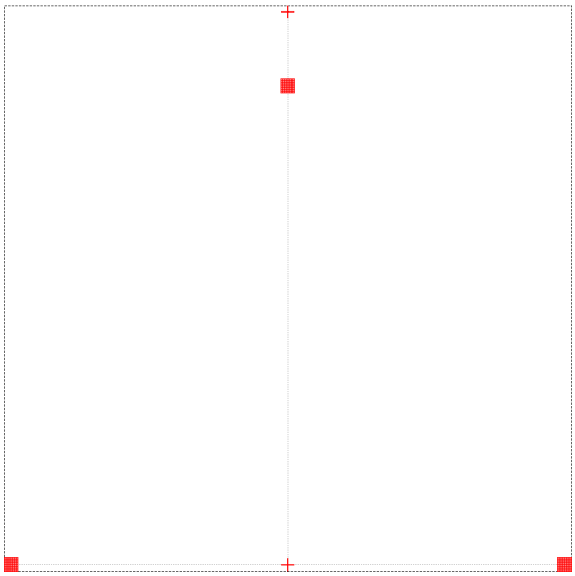

Figure 3.14: Layout of MS1 (left), MS2(right) and MS3(top) with alignment marks for aligning the aperture layer

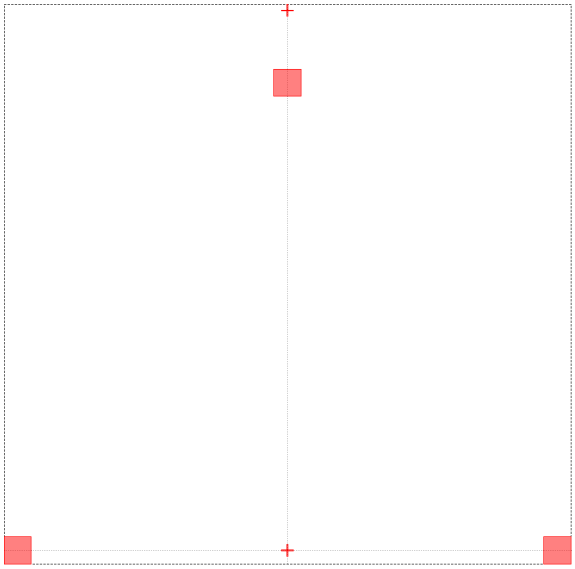

Figure 3.15: Layout for aperture layer with alignment marks. The apertures are significantly bigger than the MS areas, and can efficiency can benefit from a reduction

3.3 Analysis

3.3.1 SEM imaging

Images of the GSP samples were taken with the FEI Apreo. The settings found to give the best images were an acceleration voltage of 5 kV with a current of 0.20 nA, and using the Immersion mode. After loading the sample, the focus is first found to link the working distance to the stage.

Then, Immersion mode was selected, and the working distance were step-wise adjusted to the optimal working distance suggested by the software, which were 5.6 mm in this case.

This allowed for good images with magnification between 5000x and 100000x. Magnification up to 500 000x were reached, but at this point the image became unclear.

Due to the insulating top layer of SiO2 of the GSP samples, the wafer was grounded by applying copper tape on top of the sample, connecting the top layer to the conductive metallic sample holder. However, charging effects are still in place, limiting the quality of the images for the highest magnifications.

3.4 FDTD Simulations in ANSYS

For the FDTD simulation, the ANSYS Optical Analyzer is used. This software has a visual interface to simplify process of creating the designed structures, and achieving greater control of the relative placement and direction of simulation elements such as sources, monitors and simulation regions.

3.4.1 Exploring different monitors and post processing techniques

The first step was to get to know the ANSYS software, and understand what type of output the different built-in monitors and analysis techniques produced. The requirements for the output was a a decomposition of the field in two orthogonal polarization states, across a wide range of frequencies. It also needed to find the resulting field at the different diffracted orders.

3.4.2 Calculating the Jones and Mueller Matrix

A script in ANSYS were created to automatically calculate the Mueller Matrix. This script works as follows:

1. Setup
2. The diffracted angles are first found, by simulating for both x and y polarized light, and finding the peaks in the farfield signal. This is done only in the plane where phi = 0, due to the built in peak finding function includes too much noise in its peak finding function when the entire area is considered. This should be fixed in the future
3. The simulation is reset
4. The light source is set to a plane wave with x-polarized light
5. The simulation is executed

6. The frequency domain signal at the monitor is extracted.
7. A farfield transform is performed in spherical coordinates, resulting in field components perpendicular and parallel to the propagation direction on the far-field sphere, with a distance $r = 1m$. This returns the new s-and p polarization in scatter plane, for each angle θ, ϕ in the farfield sphere
8. Equation 2.29 is used to calculate j_{11} and j_{12}, using E_ϕ/E_{in} and E_θ/E_{in} respectively
9. The simulation is reset, the light-source is changed to y-polarized light
10. Step 4-6 is repeated
11. The remaining entries of the Jones matrix are calculated, j_{21} and j_{22}, using E_ϕ/E_{in} and E_θ/E_{in}
12. Equation 2.32 is used to calculate the Mueller Matrix
13. The data was extracted, and post-processing in Python was performed to plot the resulting Mueller Matrix

The ANSYS script can be found in Appendix A, and the Python script for post-processing and plotting is found in Appendix B.

3.4.3 Verification using simple known test cases

In order to verify the output of the simulation and calculation, the simulation were run on multiple test cases with a known optical response.

Wire grid polarizer

Wire grid polarizers polarises the light perpendicular to the direction of the wires. This will be tested for x-polarized and y-polarized wire grid polarizers. The expected Mueller matrices for perfect x-linear and y-linear polarizators are found in 2.34

Setup

- Source: The source is set by the script, at z = -1 μm, which is inside the substrate.This means that the interface between the air and substrate is not included in the simulation.
- Substrate: The substrate is created with dimensions (2 μm, 2 μm, 2 μm) at position (x = 0 μm, y = 0 μm, z = 0 μm), and the material is set to SiO2
- FDTD region is set with dimensions (2 μm, 2 μm, 3 μm), accuracy 7 and 10 wavelengths

- A frequency domain power monitor is set with dimensions (2 μm, 2 μm) at z = 2 μm. Recording wavelengths from 0.6μm to 1.3μm, with 10 frequency points
- Metallic gold wires: repeated with width 0.2 μm, with 0.2 μm spacing, thus fitting 5 wires in the structure.
- Periodic boundary conditions in x- and y-direction, and PML in z-direction

3.4.4 Simulations of the a-Si pillars

After verifying the results of the simulation, the polarisation beam splitting MS1 metasurface from [4], which splits the x- and y-polarisation states, was simulated.

Setup

- Source: The source is set by the script, at z = -1 μm, which is inside the substrate.This means that the interface between the air and substrate is not included in the simulation.
- Substrate: The substrate is created with dimensions (6 μm, 0.5 μm, 3 μm) at position (x=0μm, y=0μm, z = 0μm), and the material is set to SiO2
- FDTD region is set with dimensions (6 μm, 0.5 μm, 5 μm), accuracy 7 and 141 wavelengths
- Mesh region is set with dimensions (6 μm, 0.5 μm, 0.8 μm), with a maximum mesh size of 0.005μm
- A frequency domain power monitor is set with dimensions (6 μm, 0.5 μm) at z = 4 μm. Recording wavelengths from 0.6μm to 1.3μm, with 141 frequency points
- a-Si pillars: 715 nm, with elliptical radii listed in table 3.4, each separated by 500 nm.
- Periodic boundary conditions in x- and y-direction, and PML in z-direction

All simulations were run on a HP computer with an Intel Xeon CPU E5-2687W, and 32 GB RAM. With this setup, each simulation took approximately 12 hours.

Table 3.4: Elliptical radii of each meta atoms for MS1, MS2 and MS3 in the a-Si pillar metasurface with 12 meta-atoms per super-period, used in the first FDTD simulations

Meta Surface	**Meta Atom**	**X - elliptical radii (nm)**	**Y - elliptical radii (nm)**
12P MS1 & MS2	1	260	237.5
	2	270	235
	3	220	305
	4	210	325
	5	265	160
	6	230	205
	7	205	230
	8	160	265
	9	325	210
	10	305	220
	11	235	270
	12	237.5	260
12P MS3	*	165	250

Results and Discussion

4.1 Nanomanufacturing

4.1.1 Process characterization

Dose test of CSAR 62.09

A dose test pattern of ellipses was created, a nine by nine matrix where the elliptical radii ranged from 50 nm to 250 nm in both directions in an increasing manner. Some straight lines with thickness from 50 nm to 250 nm were also added next to the matrix. Larger rectangles were added in a cross-hair pattern outside of the elements of interest in order to easily identify where the patterns are located when inspecting with an SEM. See figure 4.1 (a).

Following the process parameters described in section 3.2.1, the pattern were applied in a four by four matrix with increasing dose, from 150 μC/cm2 and increasing by 15μC/cm2 to 375 μC/cm2 as the highest dose. The resist thickness goal was 200nm, and by reflectometry the measured thickness was 204 nm, which is within an acceptable range of error.

The SEM image shows that the ellipses are successfully created. The edges of the ellipses are brighter than the rest of the image, which is due to a edge effect of SEM as discussed in section 2.3.1, where more electrons escapes from edges compared to flat surfaces. One can also see a slightly brighter square covering about two thirds of the image. This is due to a previous focus area when doing SEM imaging, as the sample still is covered by a positive resist, which reacts to electrons. This effect is also present in samples other than EBL resists, as there can be a build up of electrons or minor "damage" from the electron beam of the SEM.

Figure 4.1 showcases three out of the 16 doses tested for CSAR 62.09. While several doses could have been suitable, a dose of 285μC/cm2 was selected due to its ability to create well-defined structures, even for the smallest feature sizes. Both higher and lower doses exhibited this capability, but dose ten was chosen as a balanced compromise between exposure time (which is significantly

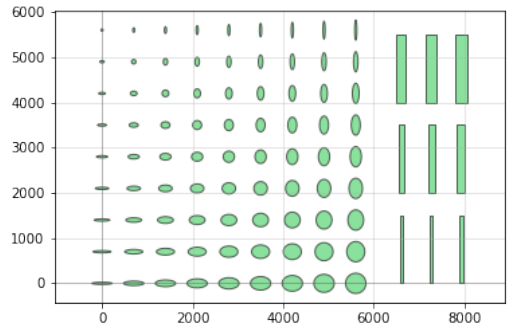

(a) Design layout for the Dose test

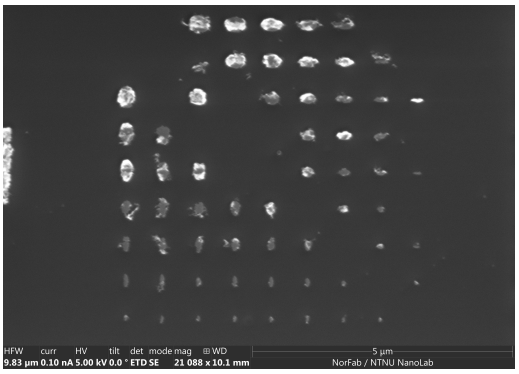

(b) Dose 165 µC/cm2

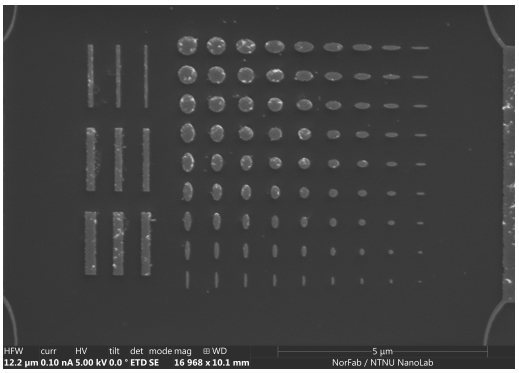

(c) Dose 285 µC/cm2

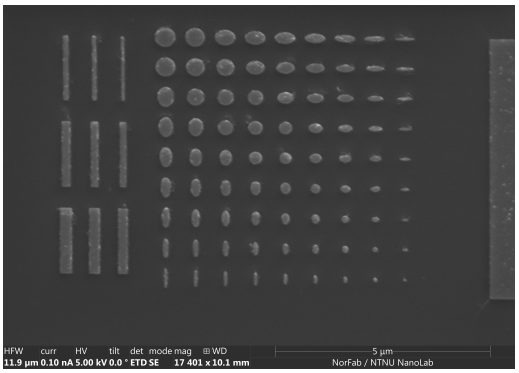

(d) Dose 375 µC/cm2

Figure 4.1: Design and SEM images for the dose test of CSAR 62.09 EBL resist

influenced by the dose) and well defined structures.

The dose test was conducted directly on crystalline silicon (c-Si). Subsequent fabrication of different metasurfaces required lithography on amorphous silicon (a-Si) on silicon dioxide (SiO2), or SiO2 on a titanium/gold/titanium (Ti/Au/Ti) stack on c-Si. The effect of these different substrates was not tested, which could introduce a source of error in the metasurface (MS) fabrication process. However, given that a-Si exhibits similar conduction and adhesion properties to c-Si, and considering the non-negligible thickness of 715 nm, it was assumed that the same process would be applicable. Similarly, a 50 nm layer of SiO2 was deemed negligible, and the electrical conductivity of the c-Si substrate and Ti/Au stack was considered sufficient to utilize the same parameters for this metasurface. Future work could potentially explore the effects of these different substrates on the MS fabrication process to further refine the process parameters.

Dose test of positive resist ma-N 2405

Figure 4.2 shows the dose test using four different doses for aperture manufacturing using the ma-N 2405 positive resist and the Electra 92 protective coating. The images show the result both after development and after metallic deposition with Cr and lift-off. The doses 250 μC/cm2 and 300 μC/cm2 both shows remains of the resist attached outside of the designed aperture, while the dose 400 μC/cm2 shows denting in the aperture edges. Thus, the dose 350 μC/cm2 is chosen as the optimal dose.

(a) Aperture after exposure with dose 250 µC/cm2

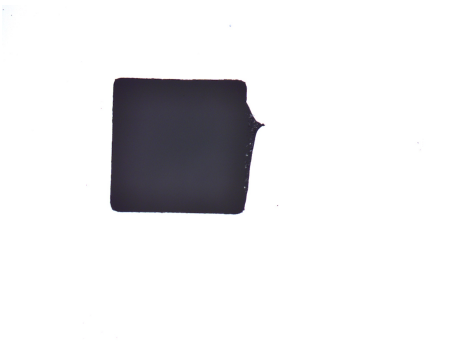

(b) Aperture after exposure and lift-off with dose 250 µC/cm2

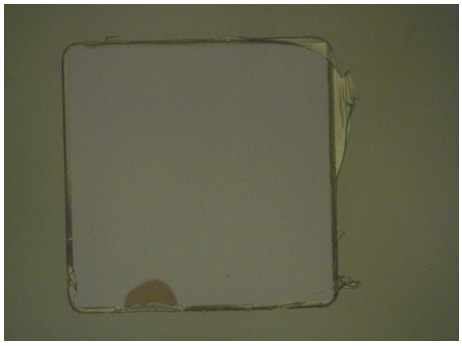

(c) Aperture after exposure with dose 300 µC/cm2

(d) Aperture after exposure and lift-off with dose 300 µC/cm2

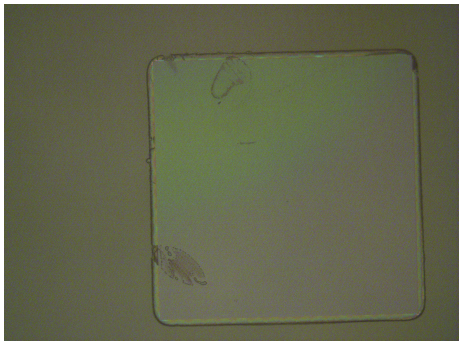

(e) Aperture after exposure with dose 350 µC/cm2

(f) Aperture after exposure and lift-off with dose 350 µC/cm2

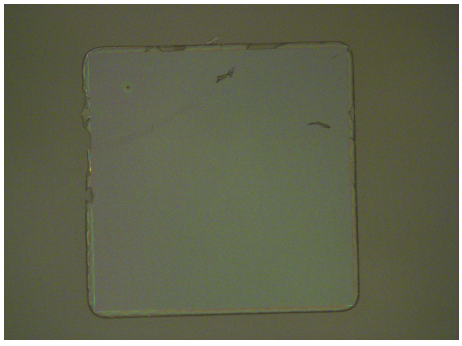

(g) Aperture after exposure with dose 400 µC/cm2

(h) Aperture after exposure and lift-off with dose 400 µC/cm2

Figure 4.2: Optical images of the dose test of the negative photoresist ma-N 2405, before and after Cr deposition and lift-of

Deposition of Cr

Figure 4.3 displays SEM images of a 200 nm Cr layer deposited on a cleaned crystalline silicon wafer. Image a) shows some particle formation on the surface at the edge of the wafer. Image b), which is taken at the center of the wafer, shows no topological roughness. Both images are in focus at a magnification of 500 times, with an acceleration voltage of 1 kV with 0.80 nA current.

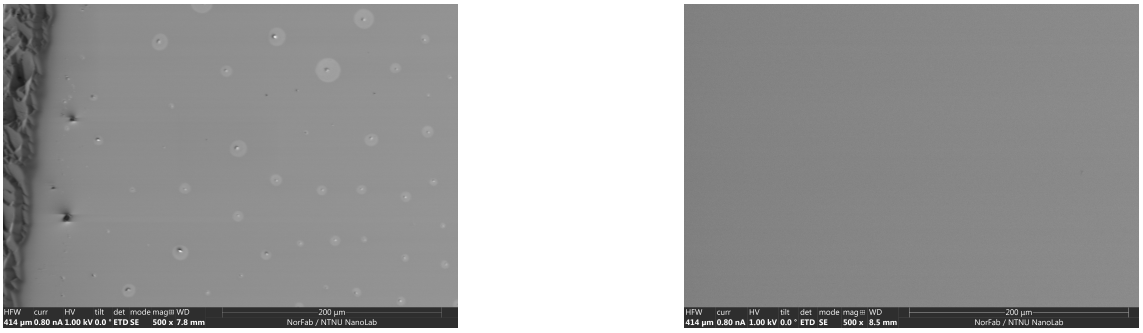

(a) (b)

Figure 4.3: SEM images of the 200 nm thick chromium film. a) shows the fil at the edge of the wafer, while b) shows the film at the center of the wafer

Figure 4.3 displays some surface contamination located on the sample's edges, but no such contamination or surface roughness is observed in the center. This outcome is acceptable, as it is customary to avoid placing any samples on the substrates' edges, which are typically reserved for handling with tweezers or fingers.

Scanning Electron Microscopy (SEM) imaging is particularly adept at revealing topological features such as surface roughness. This is due to the fact that rough surfaces tend to emit more secondary electrons from corners, edges, and peaks, which results in brighter spots in the SEM images. Since no such bright spots are visible in the central area of the sample, the surface is deemed smooth at the scale of investigation, which is at the micrometer scale.

Deposition of SiO2

The tests to find the deposition rate of SiO2 with the PECVD is summarised in figure 4.4. This shows a deposition rate of 67.44 nm/minute, with the reflectometric measurements of the thickness of the two films shown in a) and b). These shows a good fit to the theoretical model, which supports the validity of the measurements.

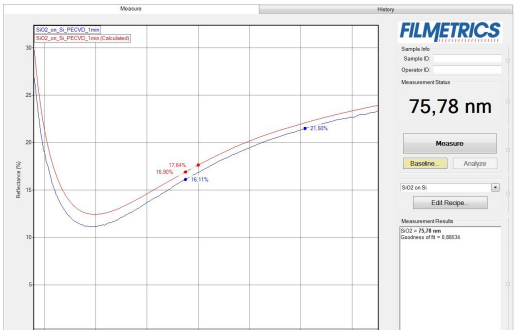

(a) Reflectometer measurements of the film grown for one minute

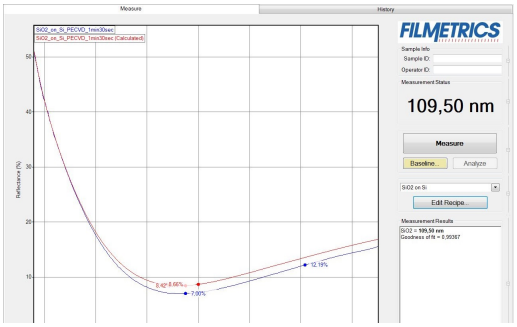

(b) Reflectometer measurements of the film grown for one minute

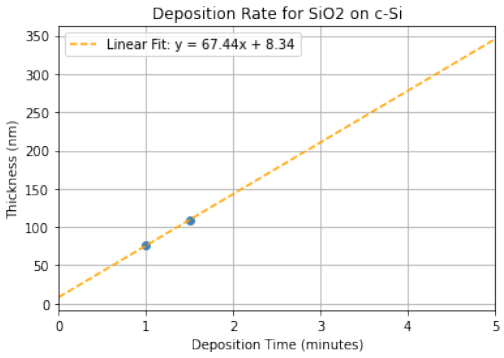

(c) Calculated deposition rate of SiO2 on c-Si

Deposition Time	Thickness
1 min	75.78 nm
1 min 30 sec	109.50 nm

(d) Table with measured thickness and corresponding deposition time

Figure 4.4: Figure a) and b) shows the measurements using the reflectometer, while figure c) shows the deposition rate assuming a linear correlation between time and thickness. The table d) summarises the thickness and deposition time of the two films.

The deposition rates determined with a c-Si wafer as a substrate was used for the metasurface manufacturing. However, as the manufacturing process of the GSP metasurfaces requires growth on a Ti/Au/Ti stack, the deposition rate here can be different, as different adhesion between materials is common. Due to the lack of identical samples with the Ti/Au/Ti stack, and keeping in mind the cost of fabricating such a stack, the found deposition rate were used as a starting point for the deposition in the metasurface fabrication, and measurements were performed between each deposition to verify and or calibrate the deposition time and deposition rate.

Deposition of a-Si

The tests to find the deposition rate of SiO2 with the PECVD is summarised in figure 4.5 and 4.6. This shows a deposition rate of 21.4 nm/minute, with the ellipsometer measurements of the thickness of the two films shown in 4.5. These shows a good fit to the theoretical model, which supports the validity of the measurements.

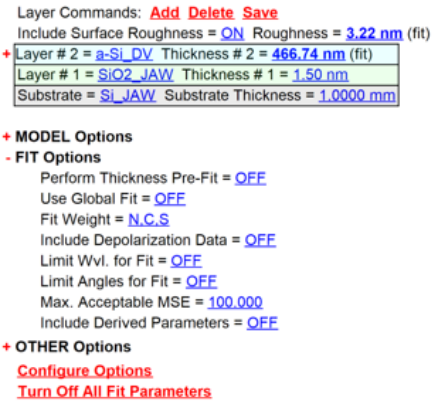

(a) Measured thickness of a-Si on c-Si wafer after 20 minutes deposition time with PECVD

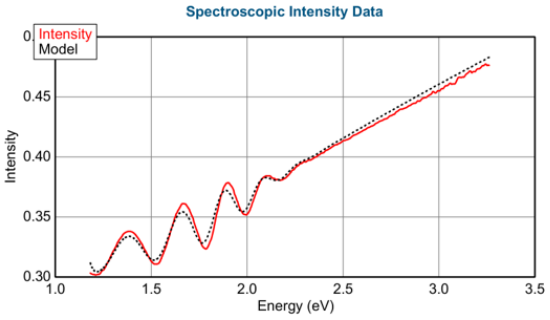

(b) Spectroscopic intensity data for a-Si film on c-Si wafer after 20 minutes deposition with PECVD

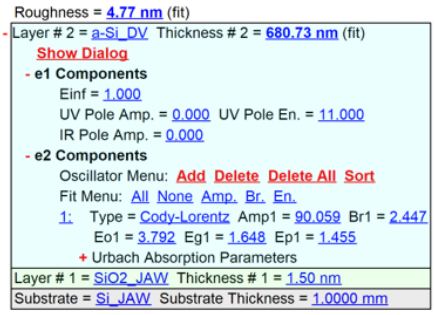

(c) Measured thickness of a-Si on c-Si wafer after 30 minutes deposition time with PECVD

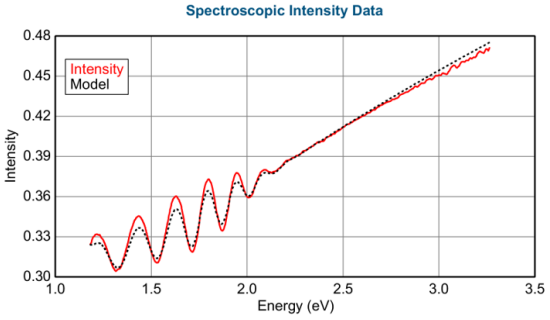

(d) Spectroscopic intensity data for a-Si film on c-Si wafer after 30 minutes deposition with PECVD

Figure 4.5: Summary of the measurements from the grown a-Si thin films

The deposition rates determined with a c-Si wafer was used for the metasurface manufacturing, where a-Si is grown on SiO2. The different adhesion between materials can change this deposition rate. Due to the lack of fused silica substrates, the found deposition rate were used as a starting point for the deposition in the MS fabrication, and measurements were performed between each deposition to verify and or calibrate the deposition time and deposition rate.

The a-Si thin films created on the c-Si substrate were not uniform, as they had a bubbly texture. After some research in the process manual for the PECVD, this is a common flaw for this material combination. However, this should not be a problem for SiO2, and the average thickness of the

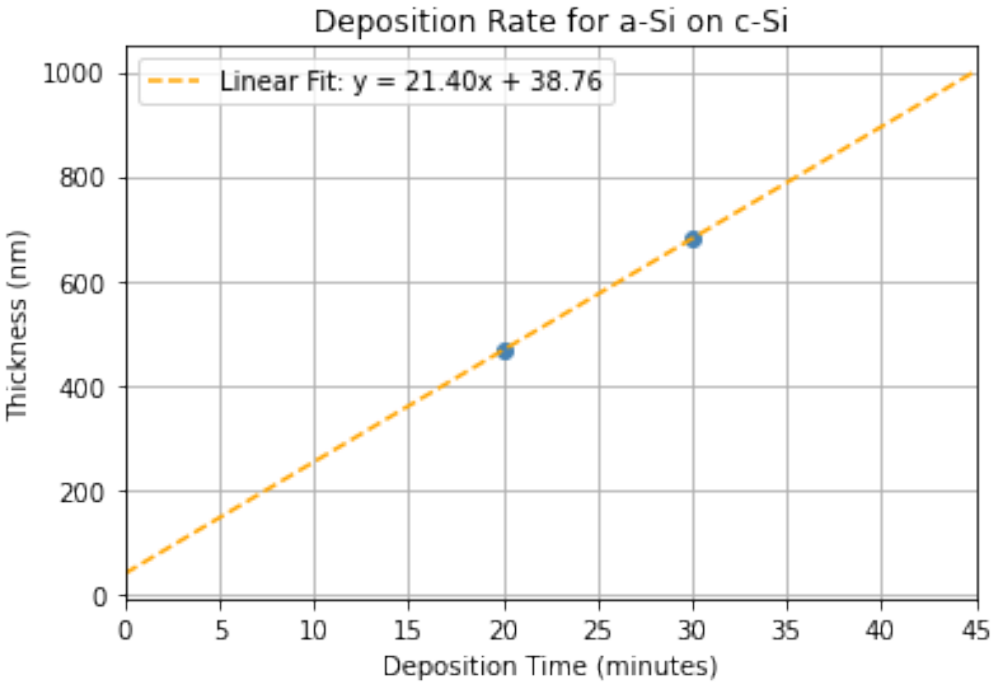

(a) Calculated deposition rate of a-Si on c-Si

Deposition time	Thickness
20 min	466.74 nm
30 min	680.73 nm

(b) Table summarising the deposition time and measured thickness for the two SiO2 films

Figure 4.6: Summary of the deposition and found deposition rate

samples were calculated and used as a starting point for fine tuning the deposition rate with the fused silica substrates, keeping in mind that the first thin-film deposition probably will give a wrong thickness.

Deposition of Au and Ti

Figure 4.7 shows the measurements of the three metallic thin films created, using variable angle spectroscopic ellipsometry (VASE). Subfigures b), d) and f) shows that the measured data fits well with the modelled data, which indicates correct results. The table 4.1 shows the measured thickness compared to the target thickness set in the e-beam evaporator. The measured Au and Ti layers did not match exactly the values, but were within an acceptable range. As the e-beam evaporator uses a built in end point detection, this is an expected result.

Layer Commands: Add Delete Save
Include Surface Roughness = OFF

Layer # 4 = Au_nk1 Thickness # 4 = **23.47 nm** (fit)
Layer # 3 = TiOxBspline Thickness # 3 = 0.00 nm
Layer # 2 = Ti Thickness # 2 = 0.00 nm
Layer # 1 = SiO2_JAW Thickness # 1 = 1.32 nm
Substrate = Si_JAW

- **MODEL Options**
  - Angle Offset = 0.00
  - Include Substrate Backside Correction = OFF
  - Model Calculation = Ideal
- **FIT Options**
- **OTHER Options**

Configure Options
Turn Off All Fit Parameters

(a) Measured thickness for the Au film deposited on c-Si with a target thickness of 20 nm

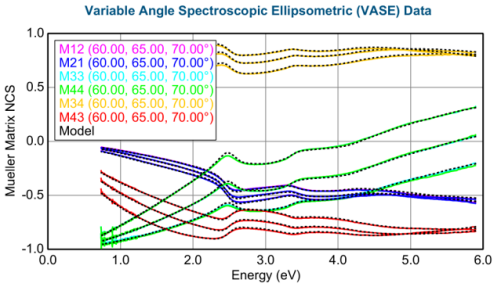

(b) Ellipsometric measurement for Au film

Layer Commands: Add Delete Save
Include Surface Roughness = OFF

Layer # 4 = Au_nk1 Thickness # 4 = 0.00 nm
- Layer # 3 = TiO2 (TaucLor) Thickness # 3 = **0.15 nm** (fit)
Show Dialog
- **e1 Components**
Einf = 1.000
UV Pole Amp. = 137.2000 UV Pole En. = 11.000
IR Pole Amp. = 0.000
- **e2 Components**
Oscillator Menu: Add Delete Delete All Sort
Fit Menu: All None Amp. Br. En.
1: Type = Tauc-Lorentz Amp1 = 256.0833
Br1 = 1.767 Eo1 = 4.002 Eg1 = 3.392
Layer # 2 = Ti Thickness # 2 = **5.58 nm** (fit)
Layer # 1 = SiO2_JAW Thickness # 1 = 1.32 nm
Substrate = Si_JAW

- **MODEL Options**
  - Angle Offset = 0.00
  - Include Substrate Backside Correction = OFF
  - Model Calculation = Ideal
- **FIT Options**
- **OTHER Options**

Configure Options
Turn Off All Fit Parameters

(c) Measured thickness for the Ti film deposited on c-Si with a target thickness of 20 nm

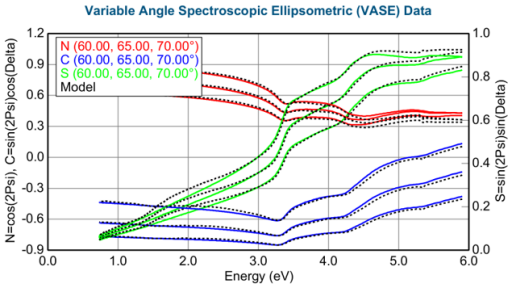

(d) Ellipsometric measurement for Ti film

Layer Commands: Add Delete Save
Include Surface Roughness = OFF

Layer # 4 = Au_nk1 Thickness # 4 = **22.89 nm** (fit)
+ Layer # 3 = TiO2 (TaucLor) Thickness # 3 = 0.00 nm
Layer # 2 = Ti Thickness # 2 = **6.59 nm** (fit)
Layer # 1 = SiO2_JAW Thickness # 1 = 1.32 nm
Substrate = Si_JAW

- **MODEL Options**
- **FIT Options**
- **OTHER Options**

Configure Options
Turn Off All Fit Parameters

(e) Measured thickness for the Ti and Au film deposited on c-Si with a target thickness of 5 nm Ti and 20 nm Au

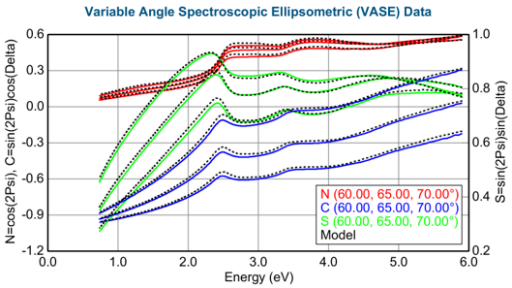

(f) Ellipsometric measurement for Ti + Au film

Figure 4.7: VASE measurements of the metallic thin films

Table 4.1: Measured and target thickness of Ti, Au and Au thin films created with e-beam evaporation.

Thin film	Target thickness	Deposited thickness
Ti	5 nm	5.58 nm
Au	20 nm	23.47 nm
Ti + Au	5 nm + 20 nm	6.59 nm + 22.89 nm

4.1.2 Aperture measurements

Figure 4.8 shows intensity measurements for the two created apertures. Figure 4.8a shows that the transmitted intensity for the two apertures are better than a glass substrate for wavelengths between 450 nm and 900 nm, and that the transmitted intensity of the two apertures decreases with increased wavelength after this point. Figure 4.8b shows that the size of the beam significantly affects the transmitted intensity of the aperture.

The measured intensity of the two apertures, as shown in figure 4.8, shows that the bigger beam size increases the transmitted intensity. This is not how an aperture should work, it should block all light outside of the aperture. Additionally, the intensity measured through the aperture should scale as $I \propto \left(\frac{A}{\lambda z}\right)^2$, where A is the area of the aperture. This means that the aperture of width 550 µm should have approximately 0.7 times the intensity of the 650 µm aperture. However, this is seen as not the case.

This leads to the conclusion that the aperture is optically transparent to a certain degree. This is either due to the 200 nm Cr layer not being optically thick for all wavelengths in question, or there could be microscopic holes in the film. these could have been created if residual resist still were present after the development step, before the Cr deposition, and thus creating holes in the lift-off process. It is recalled that the development process of the aperture is split into removing the protective coating, then developing the resist. This two step development process adds an additional possible error, as both layers needs to be removed completely for the desired result.

As a third option, there could have been holes in the protective coating, or the protective coating needs to be thicker. Errors here would have lead to the exposure of parts of the ma-N 2405 when moving out of the UV-reduced light area in NanoLab to the EBL, resulting in unintentional and undiscovered exposure of the resist, creating microscopic holes in the aperture

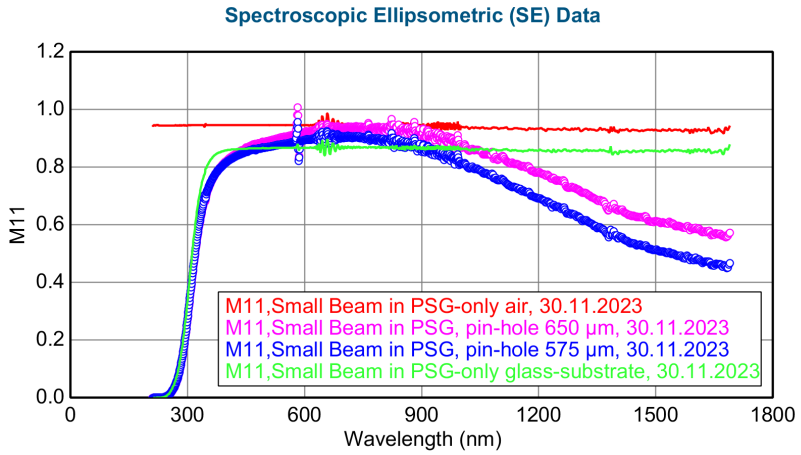

(a) Measurement of aperture efficiency with a small beam size for both apertures, along with reference measurements for air and glass substrate

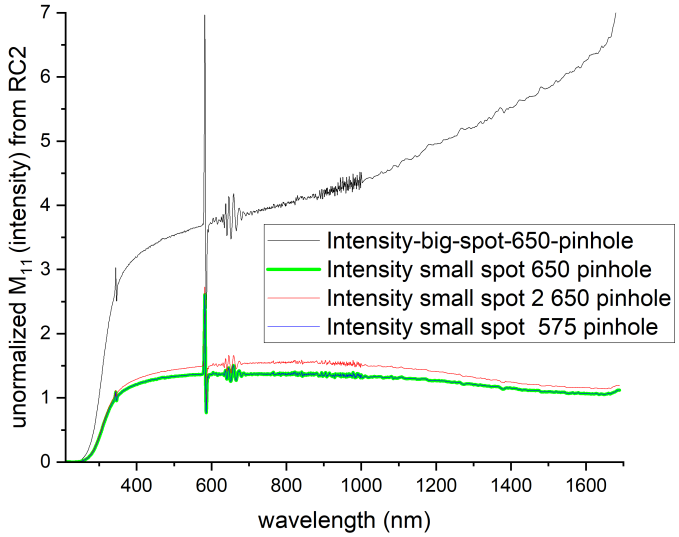

(b) Aperture measurement using both big and small beam size for the aperture with dimension 650 µm. The spikes are nonphysical artifacts from the RC2 ellipsometry system

Figure 4.8: Intensity measurements using spectroscopic ellipsometry of the two manufactured apertures

4.1.3 GSP fabrication

Ti and Au deposition

Due to the verification of the end point detection of the e-beam evaporator, and the verification of the e-beam evaporators accuracy for Ti and Au shown in figure 4.7, the manufactured layers were not further verified. The metal stack was deposited with an assumed thickness of 5 nm Ti, 40 nm

Au and another 5 nm Ti, within a 10 % error. As the function of the Ti layer is an adhesion layer, 10% error is acceptable as this does not change the function of the adhesion layer, nor the optical properties of the film in a significant way. The purpose of the Au layer is to act as a perfect electric conductor, and a 10% error should not be enough to affect this functionality.

SiO2 deposition

The SiO2 layers were measured after the each deposition. These measurements are summarised in figure 4.9. Two substrate were processed in parallel, but in the PECVD only one substrate at a time is possible. The film thickness were measured to be 53.24 nm and 51.94 nm using Ti as the substrate in the modelling software, as this was the most similar preset available. However, there are questions to the accuracy of these measurements, as seen by the difference between the measured intensity and the modelled intensity. A later attempt to model the material stack of the substrate correctly, with a c-Si wafer + 5 nm Ti + 40 nm Au + 5 nm Ti, resulted in a measured thickness of 78.77 nm and 78.82 nm respectively. The goodness of fit parameters for this model is even worse, 0.55-0.60 compared to 0.97 for the previous measurements, which lead to the measurements with the Ti substrate model being used as the resulting thickness. This lead to a new deposition rate of 67.84 nm/minute, with an 8.34 nm offset, as shown in figure 4.10.

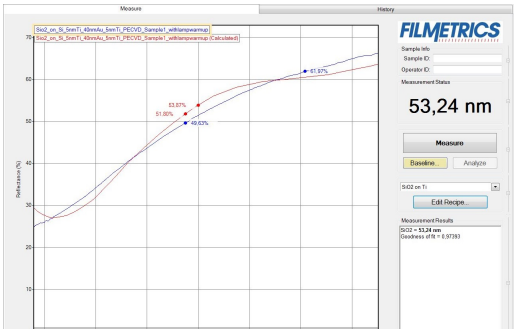

(a) Reflectometer measurements from first SiO2 film,40 seconds deposition with PECVD. Ti set as sub-strate in model

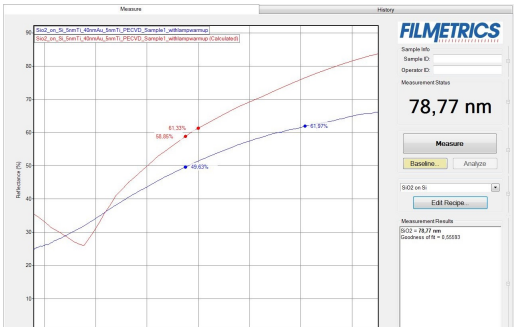

(b) Reflectometer measurements from first SiO2 film, 40 seconds deposition with PECVD. c-Si set as sub-strate in model, with 5 nm Ti, 40 nm Au and 5 nm Ti also in model

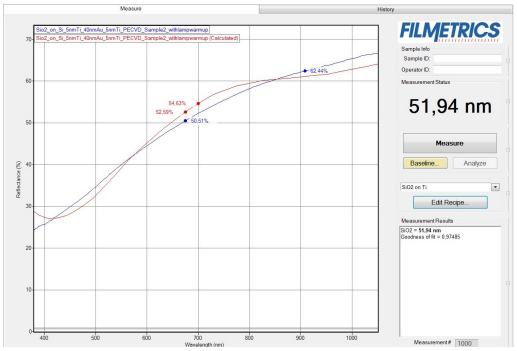

(c) Reflectometer measurements from first SiO2 film,film, 40 seconds deposition with PECVD. Ti set as sub-substrate in model

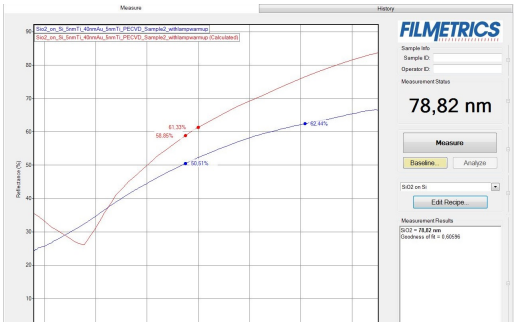

(d) Reflectometer measurements from second SiO2 film, 40 seconds deposition with PECVD. c-Si set as sub-substrate in model, with 5 nm Ti, 40 nm Au and 5 nm Ti also in model

Figure 4.9: SiO2 PECVD Measurements

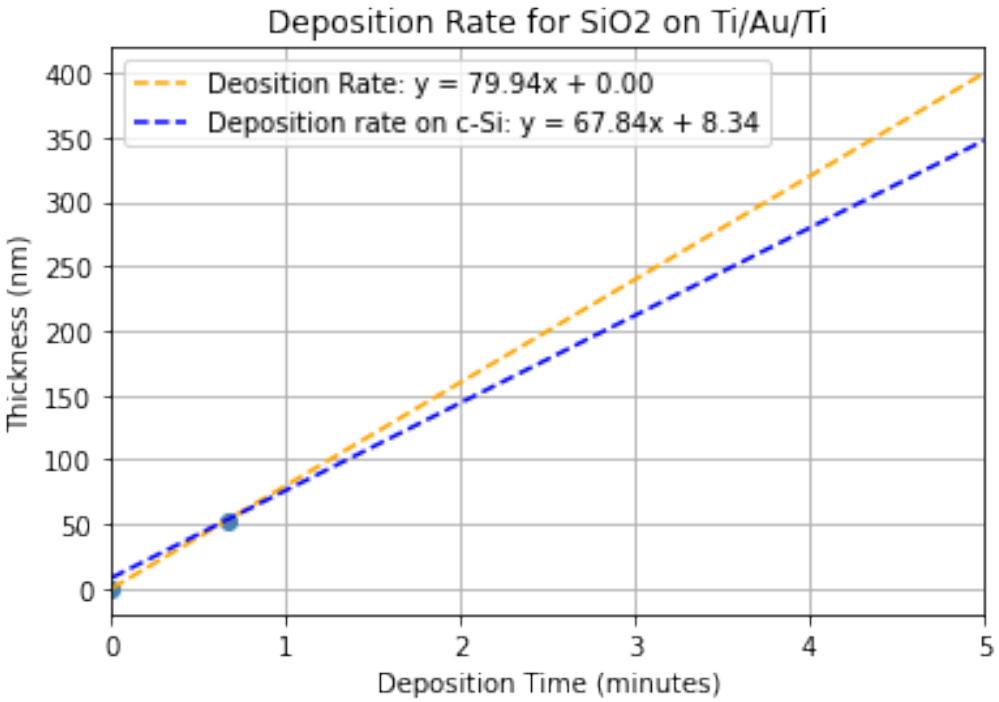

Figure 4.10: Calculated deposition rates for the two cases, along with the previously determined deposition rate

Table 4.2: The table shows the measured thickness of the two films, both with the Ti substrate model (Measured Thickness 1) and the corrected metal stack as a substrate (Measured Thickness 2). Deposition time and expected thickness are also shown.

Deposition time	Expected Thickness	Measured Thickness 1	Measured Thickness 2
40 sec	50 nm	53.24 nm	78.77 nm
40 sec	50 nm	51.94 nm	78.82 nm

Lithography

The lithography process is time-consuming, as the exposure for each substrate ranged from 12 to 16 hours. The two substrates were exposed on two separate days, with the same dose and other EBL parameters. The second substrate took significantly less time to expose compared to the first substrate, even though it had more structures and thus a larger metasurface area. This raises some suspisions to whether the correct dose time were applied in the software

After development, both samples showed visible outlines of the designed metasurface areas.

Ti and Au deposition and Lift-Off

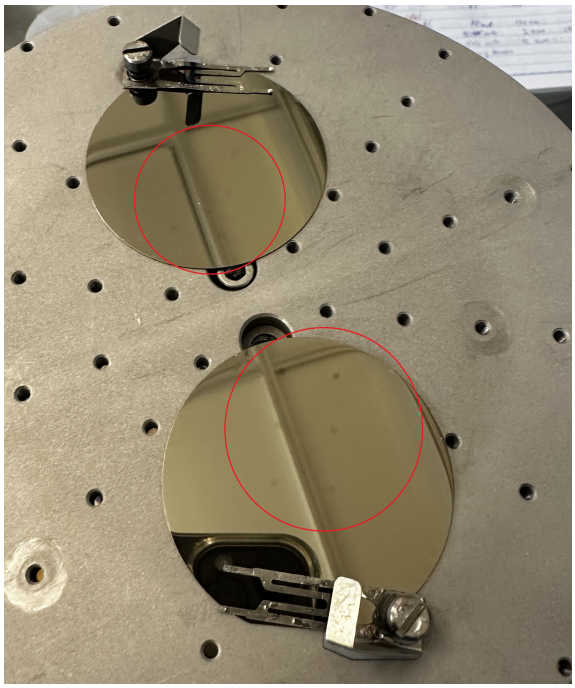

Figure 4.11: Image of the two samples after metal deposition, where the outline of all metasurfaces are visible

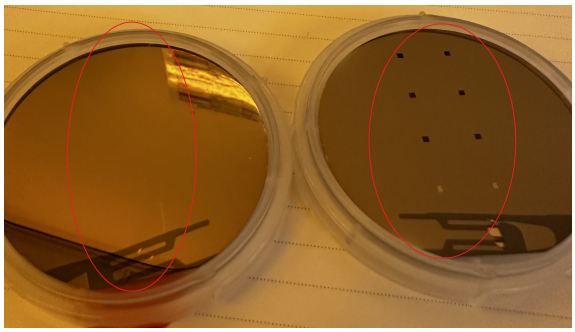

Figure 4.12: Images of the two samples after lift-off, where only one of the samples have a visible outline of the metasurfaces

Both metasurface areas were visible after the metal deposition, as seen in figure 4.11, but after the lift-off of the second substrate, the metasurface areas could not be seen anymore, as seen in figure 4.12. This was not expected, as both samples were treated equally throughout the process. The two substrates were exposed on two separate days, with the same dose and other EBL parameters. The second substrate took significantly less time to expose compared to the first substrate, even though it had more structures and thus a larger metasurface area. This raises some suspicions to whether the correct dose time were applied in the software. A lower dose would have lead to underexposed areas, and after a development the meta-atom structures may not have reached the SiO2 substrate. Thus, the metal deposition would not reach the substrate, but rather deposit in shallow trenches in the resist. This could explain how the metasurface areas were visible after the metal deposition. After the lift-off process, no gold meta atoms would remain, as the gold were only deposited on shallow resist trenches, and not in trenches that went all the way down to the substrate, ensuring contact between the substrate and the gold.

SEM images

Figure 4.13 to 4.18 presents SEM images of the six produced metasurfaces, at 5 000x, 10 000x, 30 000x and 100 000x magnification. The images are taken using the immersion mode of the SEM, using the BSE electrons. The exception is the 5P MS3 metasurface, where the regular mode were used with the SE as the image.

The images reveals that the geometry of the structures were successfully manufactured, however with some defects such as missing meta-atoms and residual gold particles.

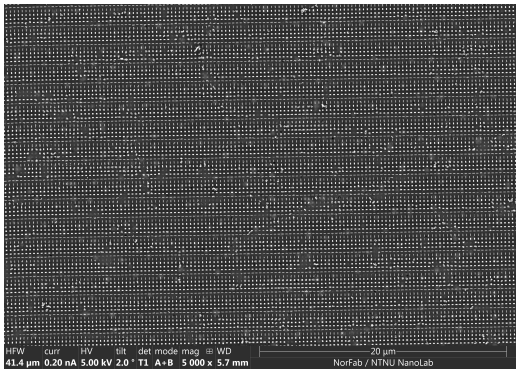

(a) 5P MS1 5 000x magnification

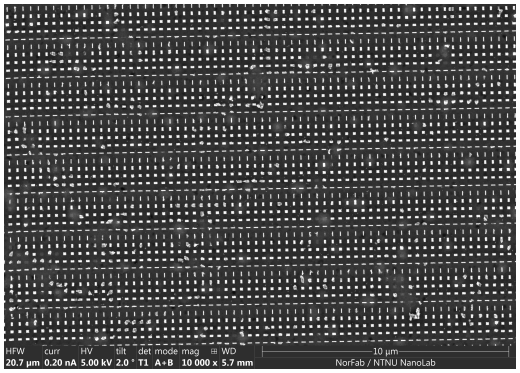

(b) 5P MS1 10 000x magnification

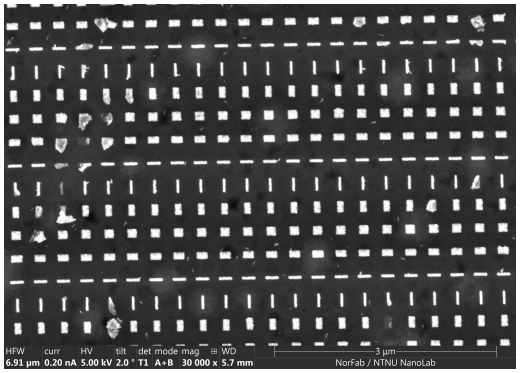

(c) 5P MS1 30 000x magnification

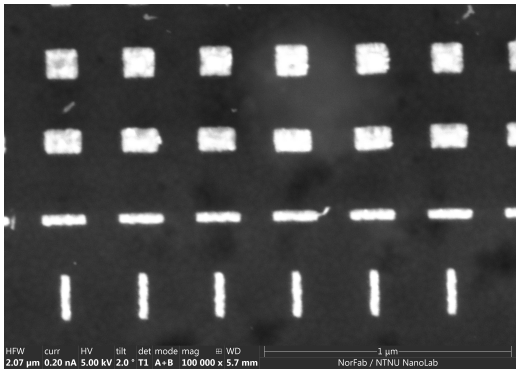

(d) 5P MS1 100 000x magnification

Figure 4.13: SEM images of the 5P MS1 samples

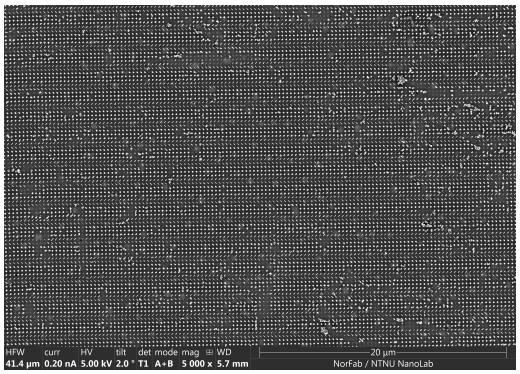

(a) 5P MS2 5 000x magnification

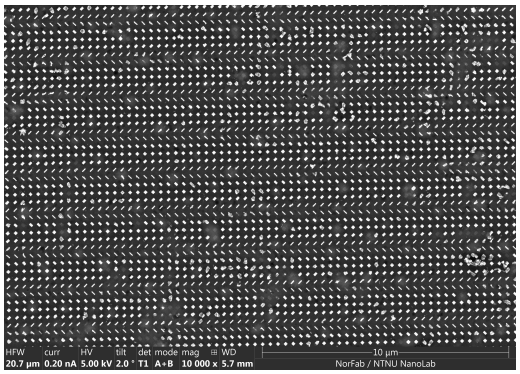

(b) 5P MS2 10 000x magnification

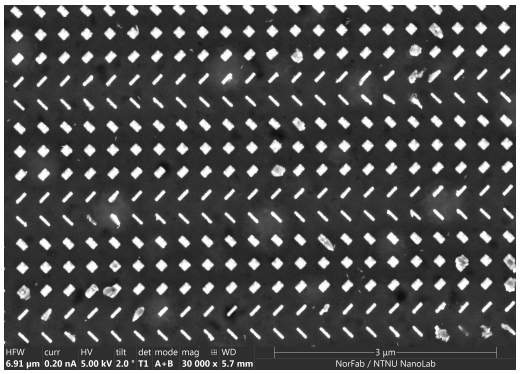

(c) 5P MS2 30 000x magnification

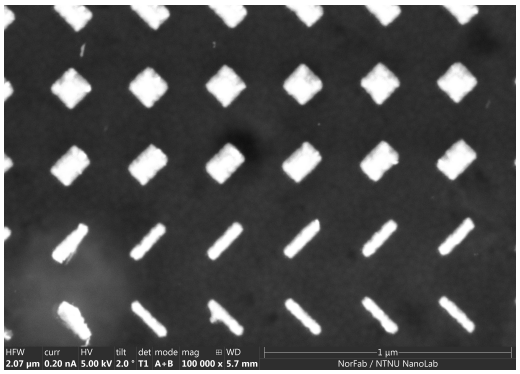

(d) 5P MS2 100 000x magnification

Figure 4.14: SEM images of the 5P MS2 samples

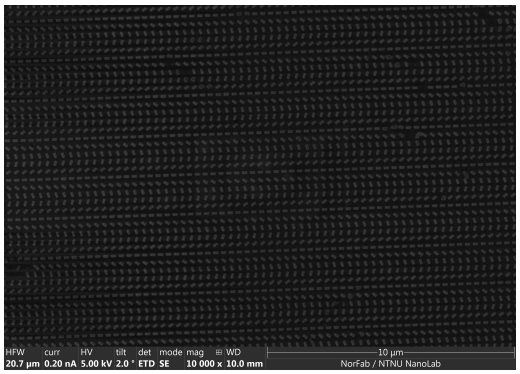

(a) 5P MS3 10 000x magnification

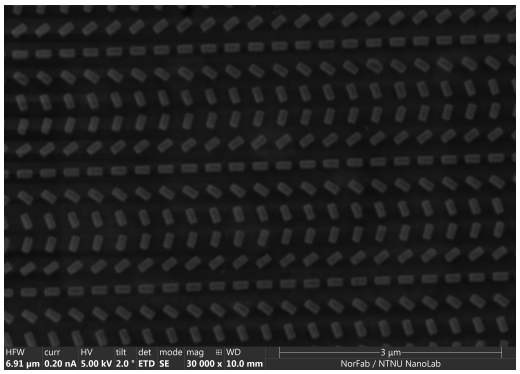

(b) 5P MS3 30 000x magnification

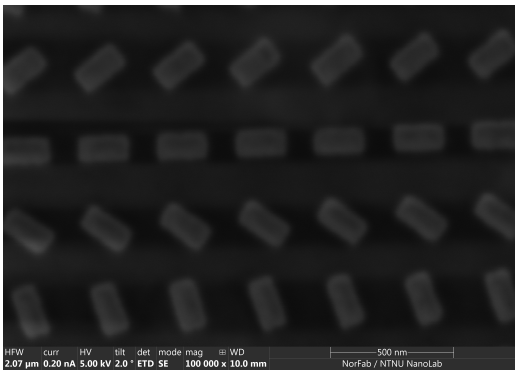

(c) 5P MS3 100 000x magnification

Figure 4.15: SEM images of the 5P MS3 samples

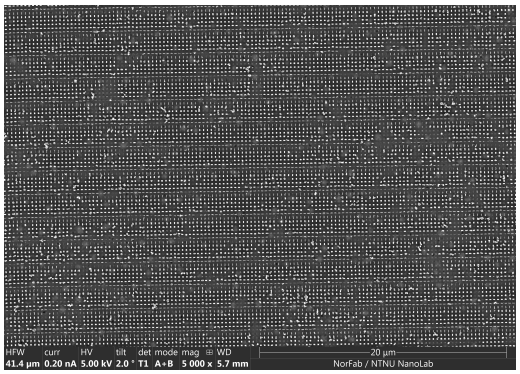

(a) 6P MS1 5 000x magnification

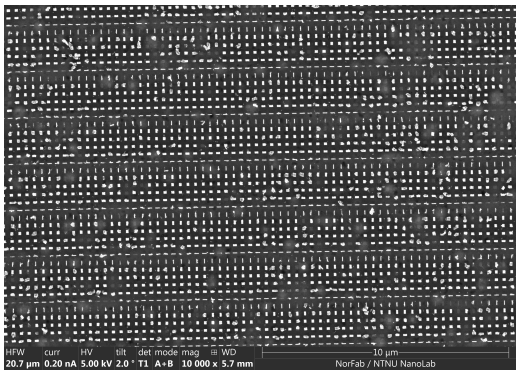

(b) 6P MS1 10 000x magnification

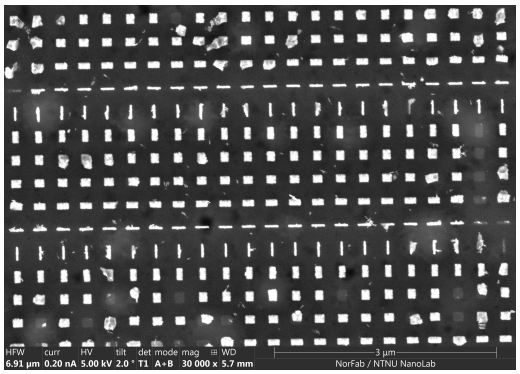

(c) 6P MS1 30 000x magnification

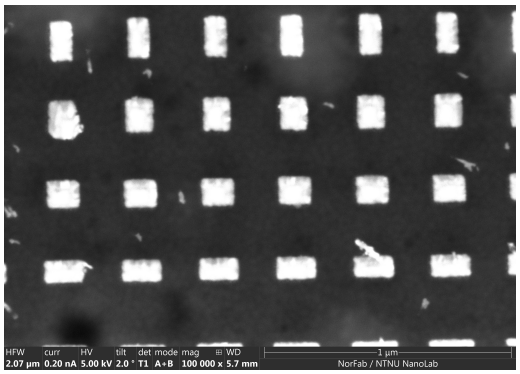

(d) 6P MS1 100 000x magnification

Figure 4.16: SEM images of the 6P MS1 samples

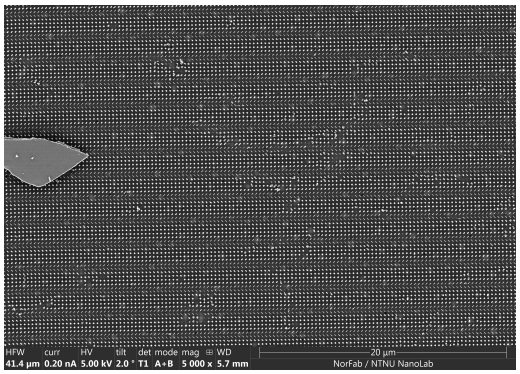

(a) 6P MS2 5 000x magnification

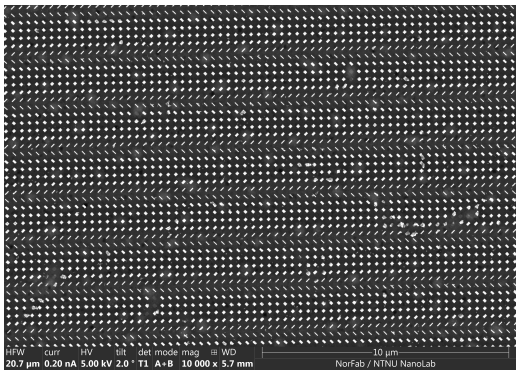

(b) 6P MS2 10 000x magnification

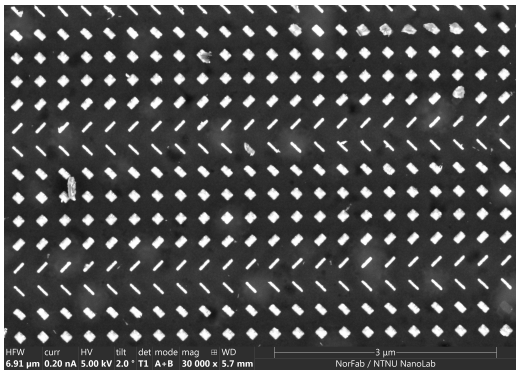

(c) 6P MS2 30 000x magnification

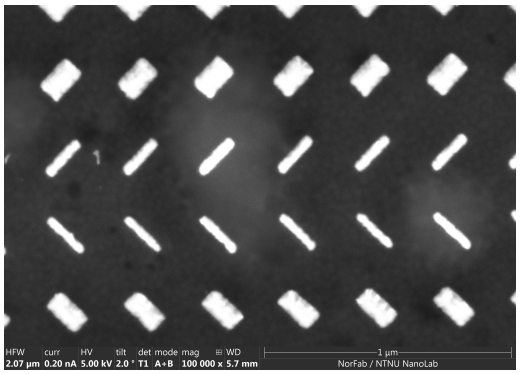

(d) 6P MS2 100 000x magnification

Figure 4.17: SEM images of the 6P MS2 samples

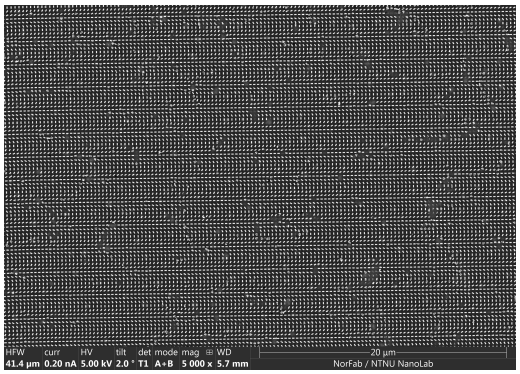

(a) 6P MS3 5 000x magnification

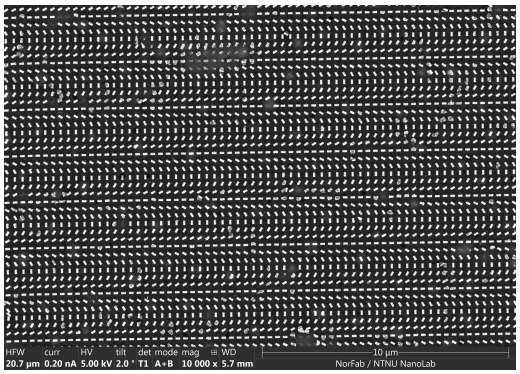

(b) 6P MS3 10 000x magnification

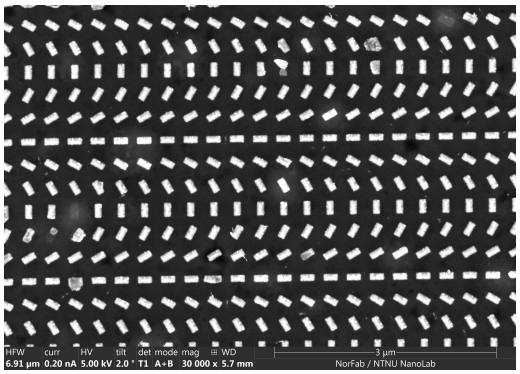

(c) 6P MS3 30 000x magnification

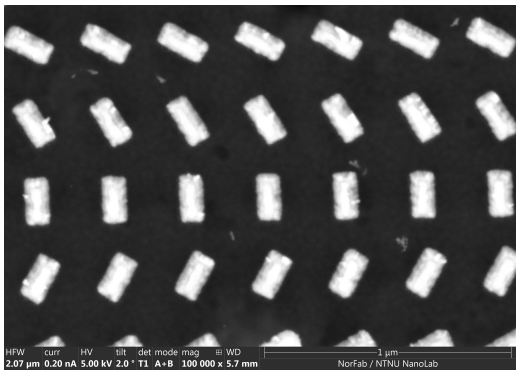

(d) 6P MS3 100 000x magnification

Figure 4.18: SEM images of the 6P MS3 samples

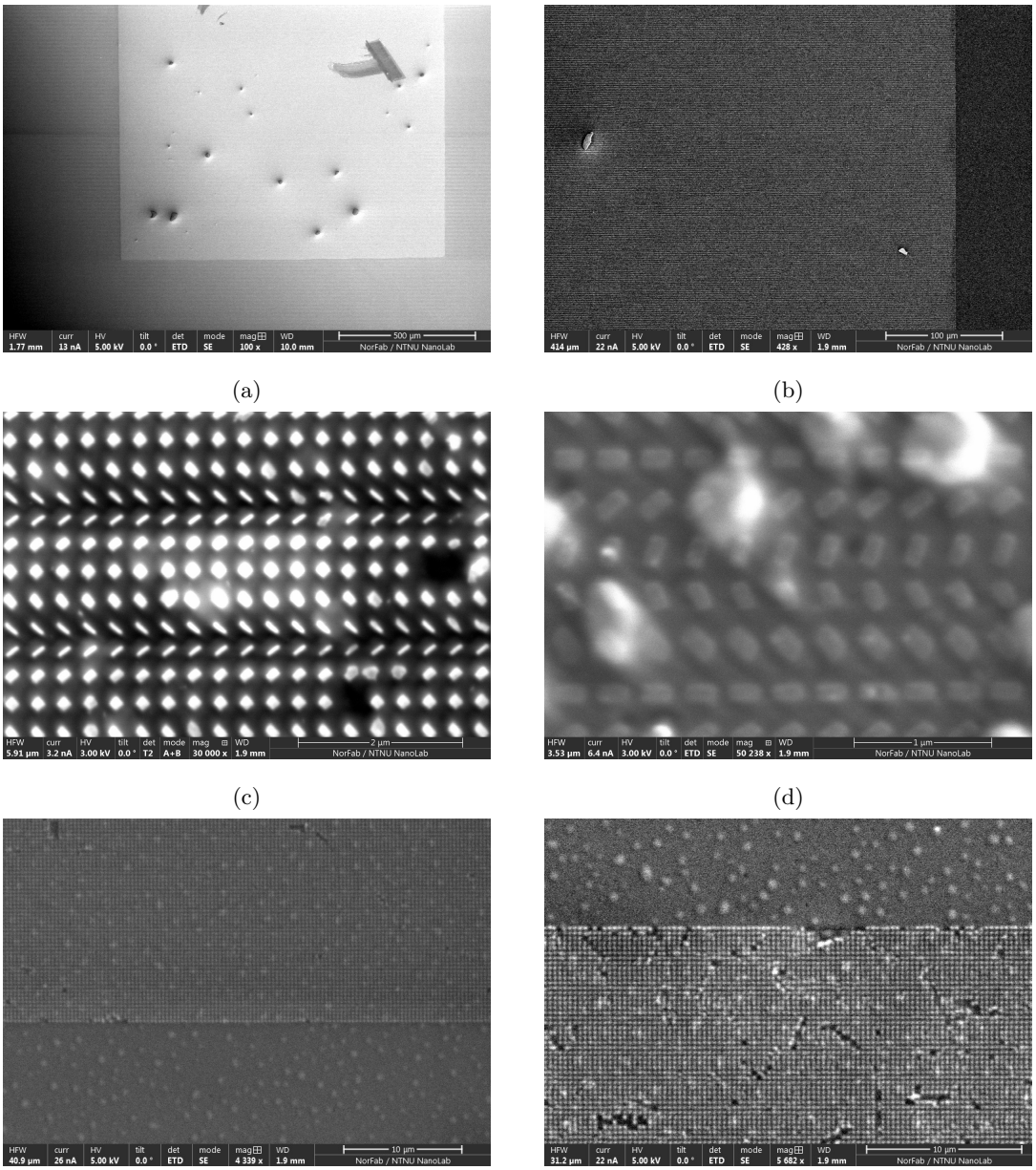

Figure 4.19: These images show different damages of the metasurfaces due to manufacturing faults. a, b and d shows contamination, while c, e and f shows missing meta-atoms

Figure 4.19 reveals some unfortunate defects originating from the fabrication process. Two significant observations can be drawn from this:

1. A substantial number of meta-atoms appear to have vanished. One plausible explanation for this could be the inadequate difference between the resist thickness and the thickness of the deposited metal stack. This discrepancy can potentially create a bridge between the metal deposited in the resist trenches and the metal on top of the resist. As a result, the metal on the resist's surface could inadvertently displace the metal deposited directly on the SiO2. Another possible cause could be a lower adhesion between Ti and SiO2 than initially anticipated. This could lead to the

detachment of the meta-atoms during the fabrication process. Future studies could investigate this aspect more thoroughly, possibly by varying the adhesion layers or by using different materials. A suggested way to mitigate this error is to increase the resist thickness to 525 nm, such that the ratio between the resist and the metallic layer is 5:1 [22].

2. The samples exhibit a significant amount of contamination. The most probable cause for this is the solvated gold forming nanoparticles, which adhere to the samples when they are lifted from the lift-off stripper solution. Some of the contamination may also be the missing meta-atoms from other areas. This contamination persists despite both rinsing in water and a rinse with acetone and Isopropyl Alcohol (IPA). Thus, an improvement in the lift-off process should also be investigated. This may be improved alone by using a thicker resist layer.

4.1.4 a-Si pillars fabrication

a-Si deposition

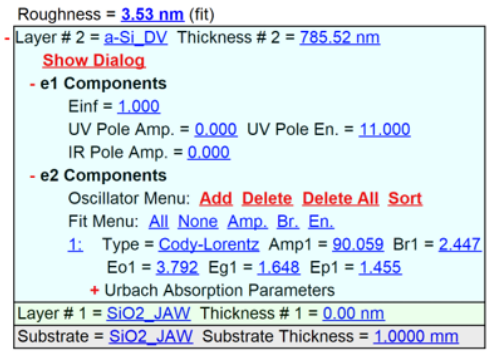

(a) Reflectometer measurements first film

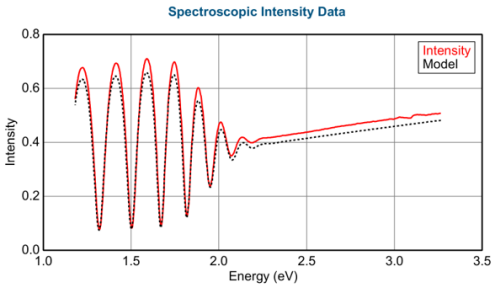

(b) Reflectometer measurements second film

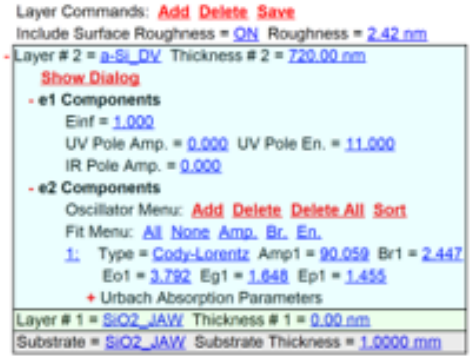

(c) Reflectometer measurements first film

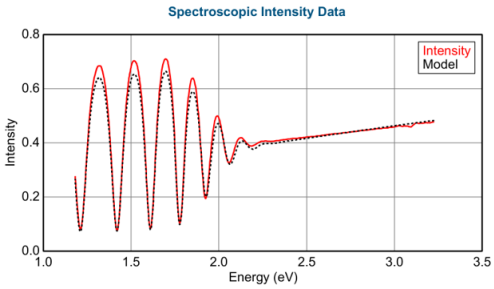

(d) Reflectometer measurements second film

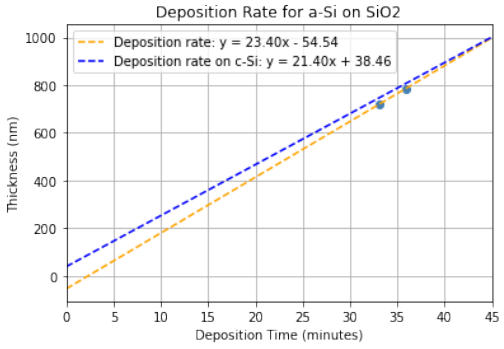

(e) graph with old and new depositon rate (Due to change in substrate)

Deposition time	Expected Thickness	Actual Thickness
24 min	715 nm	530 nm
40 min	715 nm	713 nm

(f) table showing deposition time, along with expected and actual thickness

Figure 4.20: a-Si PECVD step images

The first deposition of a-Si on SiO2 created a thicker layer than expected. After calibrating for this, by calculating a new deposition rate, the target of 715 nm were hit within acceptable range as the resulting layer were measure d to be 720 nm. The

This process did not reach as far as hoped, due to some computer troubles. However, I would like

to highlight some lessons learned if anyone will continue the work in the future:

In order for to add the aperture on top of the structure, two lithography steps are required. In order to align the two exposures, such that the apertures are correctly placed on top of the metasurfaces, alignment marks are needed. This needs to be designed into the metasurface layer, and possibly into the aperture layer if the aperture to metasurface fit wants to be measured. A protective coating on top of the positive EBL resist ma-N 2405 needs to be applied before taking the sample from the lithography finger of Nanolab to the EBL. This is due to the EBL not being in a "yellow light area", and the light will expose the positive resist, as it is UV sensitive. the protective layer used for the dose tests in this thesis also is conductive, such that one is creating that there is no charging effects occurring the EBL exposure Two 4" wafers were prepared with SiO2 growth, one with a thickness of 780 nm and one with 720 nm. Use the first substrate for any testing, and possibly divide it into several parts. Cr deposition is not expensive, so do a test or two of the full layout on the first samples, both for lithography and lift-off verification, but also to use for etch rate determination before creating correct samples on the second sample.

4.2 FDTD Simulations in ANSYS

4.2.1 Mueller matrix from linear polarizers

$$\begin{pmatrix} 1.00 & 0.91 & -1.24e-11 & 5.97e-11 \\ 0.91 & 1.00 & -7.51e-12 & 9.31e-11 \\ -1.24e-11 & -7.51e-12 & 0.42 & -6.82e-3 \\ -5.97e-11 & -9.31e-11 & 6.82e-3 & 0.42 \end{pmatrix} \qquad \begin{pmatrix} 1 & 1 & 0 & 0 \\ 1 & 1 & 0 & 0 \\ 0 & 0 & 0 & 0 \\ 0 & 0 & 0 & 0 \end{pmatrix}$$

(a) Simulated Mueller Matrix for a x-polarising wire grid polarizer

(b) Theoretical Mueller Matrix for a x-polarising wire grid polarizer

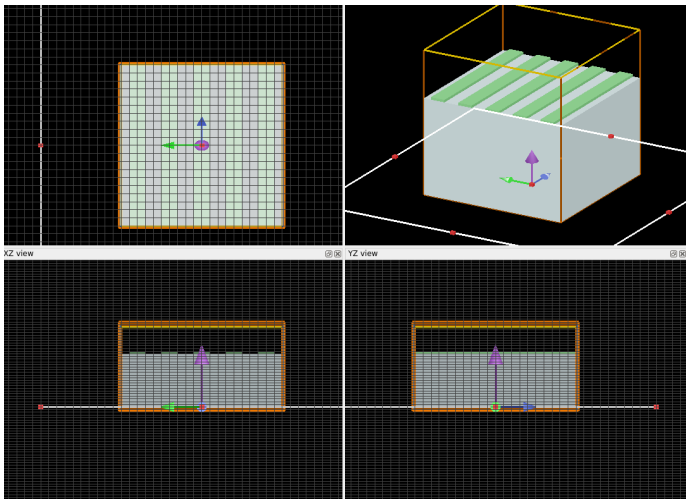

(c) Image of the simulated x-polarising wire grid polarizer in ANSYS

Figure 4.21: Summary of results from FDTD simulation of x-polarizing wire grid polarizers

The simulated Mueller Matrices for the two wire polarizers shown in figure 4.21 and 4.22, along with the theoretical Mueller Matrices of perfect linear polarizers in the x- and y- direction and images of the simulation setup. The simulated Mueller Matrices are close to the ideal linear polarizes for the x and y directions. The exception is in the Mueller Matrix elements mm_{33} ,mm_{34}, mm_{43} and mm_{44}. This could be due to an imperfection in the design, and not necessarily from the simulation. This shows that for the case of no diffraction, the simulation is able to calculate accurate Mueller Matrices.

$$\begin{pmatrix} 1.00 & -0.95 & -6.11e-12 & -9.25e-12 \\ -0.95 & 1.00 & 4.95e-12 & 6.51e-12 \\ -6.11e-12 & 4.95e-12 & -0.16 & 0.26 \\ 9.25e-12 & -6.51e-12 & -0.26 & -0.16 \end{pmatrix} \qquad \begin{pmatrix} 1 & -1 & 0 & 0 \\ -1 & 1 & 0 & 0 \\ 0 & 0 & 0 & 0 \\ 0 & 0 & 0 & 0 \end{pmatrix}$$

(a) Simulated Mueller Matrix for a y-polarising wire grid polarizer

(b) Theoretical Mueller Matrix for a y-polarising wire grid polarizer

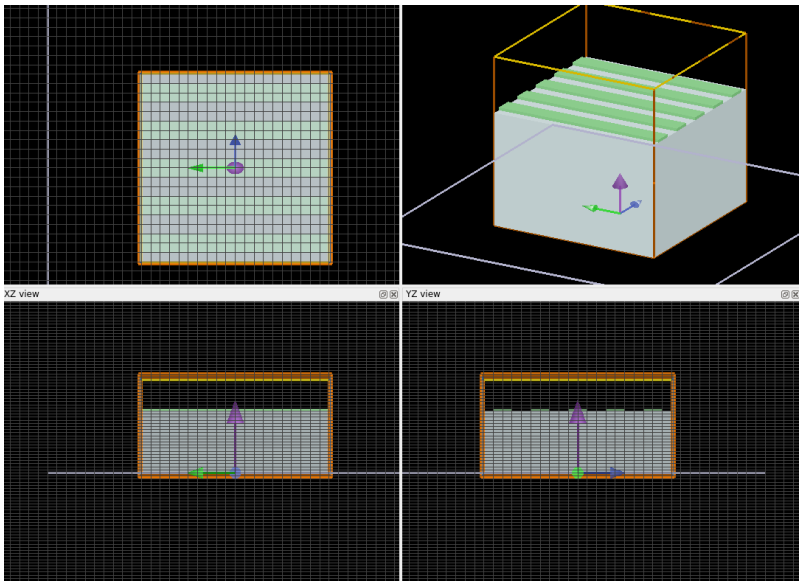

(c) Image of the simulated y-polarising wire grid polarizer in ANSYS

Figure 4.22: Summary of results from FDTD simulation of y-polarizing wire grid polarizers

4.2.2 Mueller matrix from the a-Si metasurface MS1

Figure 4.23 shows the resulting normalised Mueller Matrix from a-Si metasurface MS1 designed for a wavelength of 1000 nm, with dimensions as listed in table **??**, for the first diffracted orders m=1 and m=-1, where mm_{11} shows the normalised intensity of the Mueller Matrix. Figure 4.26 shows the corresponding angles of these diffracted orders, along with the theoretical angle. The Mueller Matrix takes the form of a x- and y-polarization splitting element, functioning from wavelengths of 900 nm and above. The peak intensity is found around 1000 nm, which are the wavelength the metasurface was designed for.

Initially, there was an mix-up between the used dimensions in the simulation, leading to an assumption that this metasurface was designed for a wavelength of 915 nm. However, after finding the shift of peak intensity towards higher wavelengths, this mix-up was clarified, and the simulation was re-run with correct dimensions of the a-Si pillars designed for a wavelength of 915 nm.

Figure 4.24 shows the resulting normalised Mueller Matrix from a-Si metasurface MS1 designed for a wavelength of 915 nm, with dimensions as listed in table 3.2, for the first diffracted orders m=1 and m=-1, where mm_{11} shows the normalised intensity of the Mueller Matrix. Figure 4.27 shows the corresponding angles of these diffracted orders, along with the theoretical angle. Again, the Mueller Matrix takes the form of a x- and y-polarization splitting element, functioning from wavelengths of 850 nm and above. The peak intensity is found around 915 nm, which are the wavelength the metasurface was designed for.

Figure 4.25 shows the Mueller Matrix for the same metasurface, designed for 915 nm, from an earlier COMSOL simulation. Comparing the FDTD Mueller Matrix for MS1 in figure 4.24 to the COMSOL simulations in figure 4.25, it is evident that they have the same shape for wavelengths from 850 nm and above. For the lower wavelengths, the FDTD result fluctuates more in its Mueller Matrix values.

Looking at mm_{11} in figure 4.24, which is the normalised intensity, the resolution around the peak at 915 nm design pops-out. The reason for this lies in the coarse methodology used to extract viable angles. In order to only consider diffracted peaks within a range of the theoretical angles, all frequency points that did not contain a detected peak with an angle within this interval were removed. Thus, in the region between 800 nm and 1000 nm, many frequency points were removed, leaving behind an inaccurate representation of the intensities and Mueller Matrix in this area.

The resolution of the angles are also coarse, with a resolution of 1 °. As the intensity of the diffracted orders drop significantly across fractions of a degree, this should be redone with a resolution of 0.1 or 0.05 °for a better result.

Figure 4.26 and 4.27 shows the theoretical diffracted angles and the found diffracted angles in the two FDTD simulation. The simulated angles are close to the theoretical angles, but does not match

exactly. The process of finding these angles were not elegant either, and needs to be improved. This result could also improve by increasing the resolution of the angels.

In total, the results proves that the used approach is feasible for finding Mueller Matrices in FDTD simulation, and can be used as a basis for future fine-tuning to achieve more accurate Mueller Matrices. The approach also allows for non-periodic metasurfaces to be simulated.

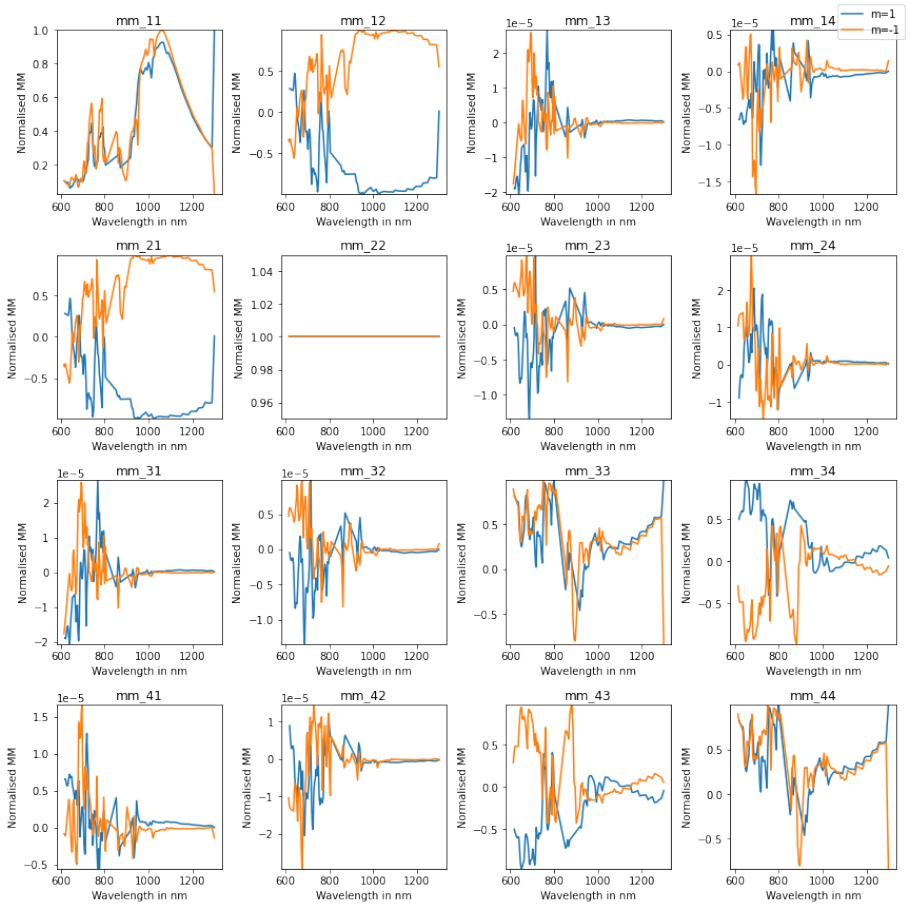

Figure 4.23: Mueller Matrix of a-Si metasurface MS1 designed for a wavelength of 1000 nm, found by FDTD simulation

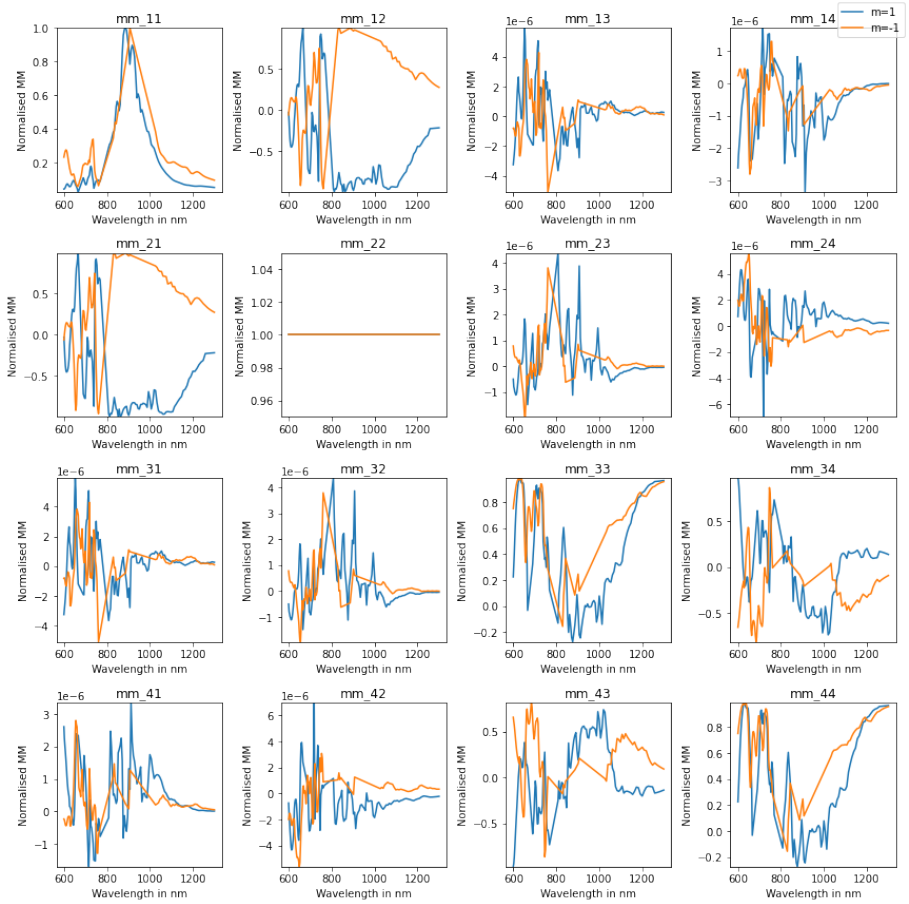

Figure 4.24: Mueller Matrix of a-Si metasurface MS1 designed for a wavelength of 915 nm, found by FDTD simulation

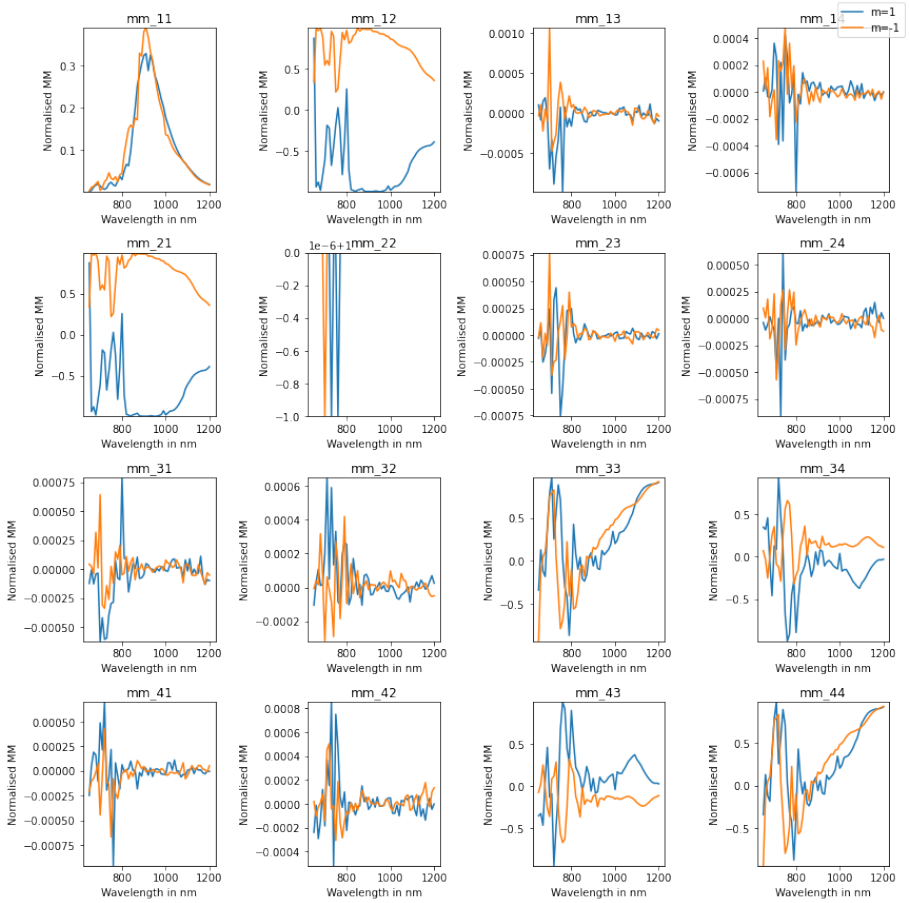

Figure 4.25: MM MS1 COMSOL simulations

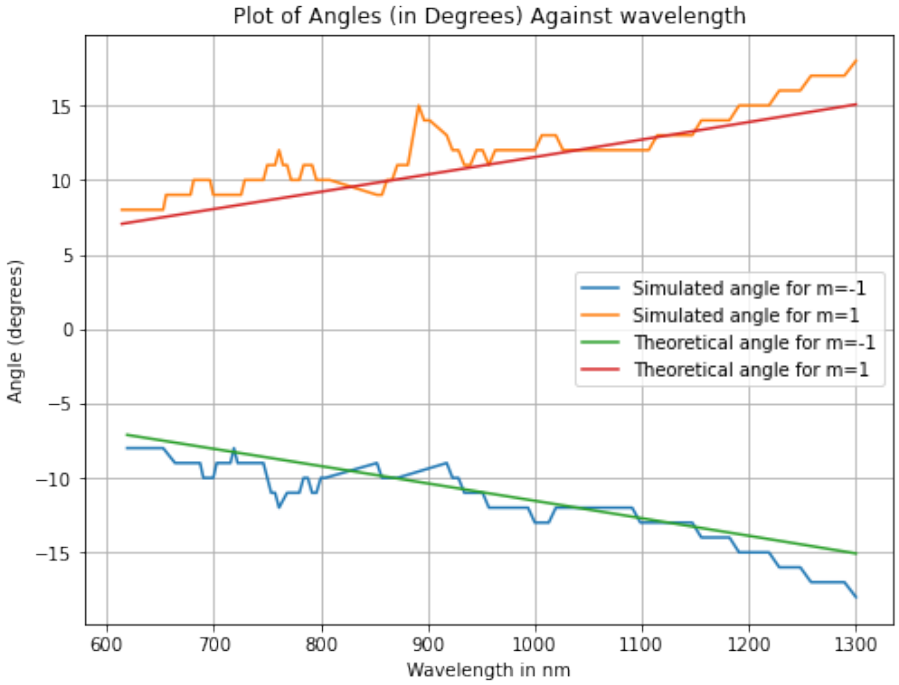

Figure 4.26: Simulated angles of diffraction plotted against the theoretical angles of diffraction, for the metasurface designed for a wavelength of 1000 nm.

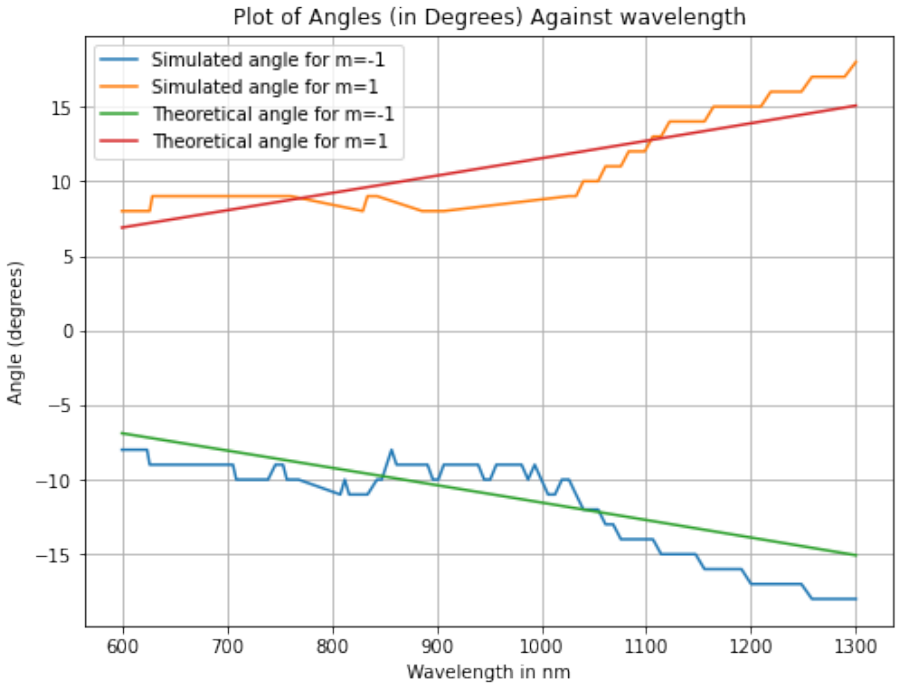

Figure 4.27: Simulated angles of diffraction plotted against the theoretical angles of diffraction, for the metasurface designed for a wavelength of 1000 nm.

Conclusion

In this thesis, the fabrication of Gap Surface Plasmon(GSP) metasurfaces was achieved, designed to reach a high angle of refraction, albeit with a few manufacturing errors. The thickness of the SiO2 layer was not precisely defined, and several meta-atoms were absent from the metasurfaces, likely due to an incorrect ratio between the EBL-resist and the metallic thin-film thickness in the lift-off process. Despite these issues, the majority of the samples were correctly manufactured, suggesting that the metasurfaces should operate as expected, but at a potentially lower efficiency than initially expected.

The process involving amorphous silicon (a-Si) pillars was completed up to the a-Si deposition stage, and design and data-preparations for EBL exposure were performed, with the exception of Proximity Effect Correction. Additionally, investigation and characterization of adding an aperture into the metasurface design was started, with measurements showing the need for further investigation regarding optical thickness or manufacturing steps to avoid micro-level holes in the aperture.

Finally, FDTD simulations through ANSYS were developed to extract Mueller Matrices for the designed metasurface. These Mueller Matrices were validated using simple examples, and the Mueller Matrix for an a-Si pillar based polarimetric beam-splitting metasurface, splitting horizontal and vertical polarization states, was compared with COMSOL simulations for same metasurface, showing comparable results.

Future Work

As the manufactured GSP meta-surfaces had too many missing meta-atoms, the metasurfaces should be redone and perfected. This is not a difficult process, as most process parameters are accounted for. As the probable reason of the missing meta-atoms is the relative thickness between the resist and the deposited metal layer before the lift-off, the lithography step needs to be redone with a thicker resist thickness. I suggest to aim for 525 nm resist thickness, as this should be sufficient for a successful lift-off step with a metallic layer of 105 nm[22]. This can either be done using a lower rotation speed in the spin-coating process, or by using a less diluted version of CSAR 62 witch have a higher viscosity. Consult the datasheet for CSAR 62 for more information regarding parameters for a thicker resist-layer. [19]A new optimal dose must be found by a dose test. The dose test files used in this thesis, along with all metasurface designs are stored in a drive, contact prof. Kildemo for access. Feel free to reuse these.

For the a-Si pillars with an integrated aperture, the steps until the etch process is described. As the aperture created had some microscopic holes in it, an improvement of its manufacturing process is necessary. The two possible reasons for the unexpected high illumination are microscopic holes in the thin film, or that the 200 nm chromium layer is not optically thick. Two further investigate this, two process steps are suggested: A development test, as residual resist - fragments after development would lead to holes from the lift-off as the chromium would adhere to these fragments. This includes both for the ma-N 2405 resist and the protective coating Electra 92. Secondly, a verification of optical transparency of a 200 nm chromium layer, in addition to thicker chromium layers, are suggested.

Furthermore, etch-rate determination needs to be conducted. NanoLab are currently in the process of replacing their ICP-RIE instruments, and are also planning to install other novel etching machines suitable for silicon etching with a high degree of anisotropy. This could help counteract conical shapes from the previous manufacturing as described in [4].

Two wafers of fused silica, with grown layers of 780 nm and 720 nm of a-Si were produced in this work. These should be used for both dose test, etch rate determination and development

test. I recommend to use the wafer with thickness 780 nm for all testing and further process characterisation, and the 720 nm wafer for manufacturing of the final a-Si metasurfaces. Both wafers are of size 4", and to maximise the use of these I recommend to cut the wafers into smaller pieces.

Additionally, all dose tests should be performed again. This is because the resists degrade over time, leading to a change in both viscosity and chemical composition, and a spin coat process with the same parameters will not create the same thickness of the resist, thus requiring a different dose.

As for the FDTD simulations, the resolution used in this work is one degree, which is too small as measurements on real samples shows a significant drop in intensity across the range of one degree. In the attached script in Appendix A, this is done in the line "theta = linspace(-90,90,181);", by increasing the third input parameter. "theta = linspace(-90,90,1801);" would give a 0.1 degree resolution for instance. Additionally, the resolution of the initial far field transform should be increased, by the same factor, i.e. by setting "res = 2001;"

Additionally, the way the angles are extracted are complicated, and leads to lacking data across some ranges of wavelengths. I suggest to extract the Mueller Matrix for all angles, and doing the work of finding the correct angle of the first diffracted order in post-processing in Python, Matlab or similar software. By rewriting the script this way, the initial run of the simulation can be removed, reducing the required runtime by 33%.

Other possibilities to build on this work includes:

Including focusing design: Designing for a phase profile of a lens, it is possible to focus the spitted polarisation states onto different points. The simulation tool implemented in FDTD can be used as a basis, incorporating designs such as those proposed by Groever et. al.[23] or by West et.al. [24]. A possible challenge here is that the focus point may not reside at the farfield sphere at 1m, which is used in the Mueller Matrix calculations.

Build device into fluidic channel, to use as and differential detector: Building a proof of concept use of the technology, to see if it successfully can be used as a sensor. An example of this is the ability to detect chiral molecules in a fluid, as these molecules absorbs left-handed or right-handed circular polarized light, based on their chirality.

Manufacturing processes for industrial manufacturing: In order to efficiently and accurately create such metasurfaces for commercial use, it is unsuitable to use EBL, as one metasurface design takes up to 6 hours to expose alone. Thus, more industrial approach such as nanoimprint lithography, or optical lithography with a mask are possible options for manufacturing in larger batches.

Bibliography

[1] Fei Ding, Anders Pors and Sergey I Bozhevolnyi. 'Gradient metasurfaces: a review of fundamentals and applications'. In: *Reports on Progress in Physics* 81.2 (Dec. 2017), p. 026401. DOI: 10.1088/1361-6633/aa8732. URL: https://dx.doi.org/10.1088/1361-6633/aa8732.

[2] Nanfang Yu and Federico Capasso. 'Optical metasurfaces and prospect of their applications including fiber optics'. In: *Journal of Lightwave Technology* 33.12 (2015), pp. 2344–2358.

[3] Aobo Li, Shreya Singh and Dan Sievenpiper. 'Metasurfaces and their applications'. In: *Nanophotonics* 7.6 (2018), pp. 989–1011.

[4] Victoria M. Bjelland et al. 'Diffractive order Mueller matrix ellipsometry for the design and manufacture of polarization beam splitting metasurfaces'. In: *Opt. Express* 32.1 (Jan. 2024), pp. 703–721. DOI: 10.1364/OE.501709. URL: https://opg.optica.org/oe/abstract.cfm?URI=oe-32-1-703.

[5] Per Magnus Walmsness, Nathan Hale and Morten Kildemo. 'Spectroscopic Mueller matrix ellipsometry of a gap surface plasmon array at conical incidences'. In: *J. Opt. Soc. Am. B* 38.9 (Sept. 2021), pp. 2551–2561. DOI: 10.1364/JOSAB.432466. URL: https://opg.optica.org/josab/abstract.cfm?URI=josab-38-9-2551.

[6] L. Novotny and B. Hecht. *Principles of Nano-Optics*. Cambridge University Press, 2006. ISBN: 9781139452052. URL: https://books.google.no/books?id=Qrf036kThTQC.

[7] H. Arwin. *Thin Film Optics and Polarized Light*. Hans Arwin, 2015. URL: https://books.google.no/books?id=k-6HnQAACAAJ.

[8] Craig F Bohren and Donald R Huffman. *Absorption and scattering of light by small particles*. John Wiley & Sons, 2008.

[9] Nanfang Yu et al. 'Light Propagation with Phase Discontinuities: Generalized Laws of Reflection and Refraction'. In: *Science* 334.6054 (2011), pp. 333–337. DOI: 10.1126/science.1210713. eprint: https://www.science.org/doi/pdf/10.1126/science.1210713. URL: https://www.science.org/doi/abs/10.1126/science.1210713.

[10] J.W. Goodman. *Introduction to Fourier Optics*. McGraw-Hill physical and quantum electronics series. W. H. Freeman, 2005. ISBN: 9780974707723. URL: https://books.google.no/books?id=ow5xs_Rtt9AC.

[11] University of Alberta. 'Interference pattern of the light diffracted on multiple slits'. In: (). URL: https://sites.ualberta.ca/~pogosyan/teaching/PHYS_130/FALL_2010/lectures/lect36/lecture36.html.

[12] Charles Kittel. *Introduction to solid state physics*. John Wiley & sons, inc, 2005.

[13] Liming Ren and Baoqin Chen. 'Proximity effect in electron beam lithography'. In: *Proceedings. 7th International Conference on Solid-State and Integrated Circuits Technology, 2004.* Vol. 1. 2004, 579–582 vol.1. DOI: 10.1109/ICSICT.2004.1435073.

[14] John B. Schneider. *Understanding the Finite-Difference Time-Domain Method*. https://eecs.wsu.edu/ schneidj/uf 2023.

[15] Niklas Schwarz. 'Nanomanufacturing of dielectric metasurfaces supported by spectroscopic Mueller Matrix Ellipsometry'. MA thesis. Norwegian University of Science and Technology (NTNU), 2022.

[16] Anders Pors, Michael G. Nielsen and Sergey I. Bozhevolnyi. 'Plasmonic metagratings for simultaneous determination of Stokes parameters'. In: *Optica* 2.8 (Aug. 2015), pp. 716–723. DOI: 10.1364/OPTICA.2.000716. URL: https://opg.optica.org/optica/abstract.cfm?URI=optica-2-8-716.

[17] Franco Gori. 'Measuring Stokes parameters by means of a polarization grating'. In: *Opt. Lett.* 24.9 (May 1999), pp. 584–586. DOI: 10.1364/OL.24.000584. URL: https://opg.optica.org/ol/abstract.cfm?URI=ol-24-9-584.

[18] Mohammadreza Khorasaninejad et al. 'Visible wavelength planar metalenses based on titanium dioxide'. In: *IEEE Journal of Selected Topics in Quantum Electronics* 23.3 (2016), pp. 43–58.

[19] Allresist. 'E-Beam Resist AR-P 6200 series (CSAR 62)'. In: (). URL: https://www.allresist.com/wp-content/uploads/sites/2/2020/03/AR-P6200_CSAR62english_Allresist_product-information.pdf.

[20] Micro Resist Technology. 'ma-N 2400 series'. In: (). URL: https://www.microresist.de/en/produkt/ma-n-2400-series/.

[21] Allresist. 'Protective Coating Electra 92 (AR-PC 5092)'. In: (). URL: https://www.allresist.com/wp-content/uploads/sites/2/2023/12/Allresist_Product-information-E-beamresist-AR-PC-5092-English.pdf.

[22] University of Michigan LNF. 'Lift-off'. In: (). URL: https://lnf-wiki.eecs.umich.edu/wiki/Lift-off#:~:text=The%20metal%20must%20be%20thinner,than%205%3A1%20are%20preferable.f.

[23] Benedict Groever et. al. 'High-efciency chiral meta-lens'. In: *Scientific Reports* 8 (2018).

[24] Paul R. West et al. 'All-dielectric subwavelength metasurface focusing lens'. In: *Opt. Express* 22.21 (Oct. 2014), pp. 26212–26221. DOI: 10.1364/OE.22.026212. URL: https://opg.optica.org/oe/abstract.cfm?URI=oe-22-21-26212.

Appendix A - ANSYS Script for finding Mueller Matrices

```
    #delete previous source if run several times in succession
switchtolayout;
select("plane_wave");
delete;
#Set input to p-polarized (polarization angle = 0)
addplane;
set("name","plane_wave");
set("injection axis","z");
set("direction","forward");
# I think the x and y span should match the fdtd region's xy-plane, or at least cover it
set("x",0);
set("x span",6e-6);
set("y",0);
set("y span",0.5e-6);
set("z",-1e-6);
set("wavelength start",0.6e-6);
set("wavelength stop",1.3e-6);
set("polarization angle",45);
run;
# specify monitor name, get frequency vector
mname="monitor";
f=getdata(mname,"f");


n = 1; # Number of peaks to consider
```

```
res = 201; # Resolution for far field transform

jones = matrix(2,2,length(f),n); # Matrix to store all Jones vectors
angles = matrix(n,length(f));
A = [ 1,0,0,1; 1,0,0,-1;0,1,1,0;0,1i,-1i,0];
A_inv = [ 1,1,0,0; 0,0,1,-1i; 0,0,1,1i;1,-1,0,0]*0.5; # matricies for Mueller matrix calculation

  # loop over each frequency point
  for (fi=1:length(f)) {

    # Find  diffracetd peaks
    E2 = farfieldpolar3d(mname,fi,res,res);
    ux = farfieldux(mname,fi,res,res);
    uy = farfielduy(mname,fi,res,res);
    theta = linspace(-90,90,181);
    phi = linspace(0,90,91);
    Theta = meshgridx(theta,phi);
    Phi = meshgridy(theta,phi);
    Etheta_angle = farfieldspherical(E2(:,:,2),ux,uy,Theta,Phi);
    Etheta_angle = reshape(Etheta_angle, [length(theta), length(phi)]);
    Ephi_angle = farfieldspherical(E2(:,:,3),ux,uy,Theta,Phi);
    Ephi_angle = reshape(Ephi_angle, [length(theta), length(phi)]);



    Ephi_2 = abs(Ephi_angle)^2;
    Etheta_2 = abs(Etheta_angle)^2;
    E2_spherical = sqrt(Etheta_2 + Ephi_2);
    peaks = findpeaks(E2_spherical(:,1),n);

    angles(:,fi)=peaks;
    angles(:,fi) = sort(angles(:,fi));
    # At each peak, Find the Jones matrix contribution
   }
#delete previous source if run several times in succession
switchtolayout;
select("plane_wave");
delete;
#Set input to p-polarized (polarization angle = 0)
addplane;
```

```
set("name","plane_wave");
set("injection axis","z");
set("direction","forward");
# I think the x and y span should match the fdtd region's xy-plane, or at least cover it
set("x",0);
set("x span",6e-6);
set("y",0);
set("y span",0.5e-6);
set("z",-1e-6);
set("wavelength start",0.6e-6);
set("wavelength stop",1.3e-6);
set("polarization angle",0);
run;
# specify monitor name, get frequency vector
mname="monitor";
f=getdata(mname,"f");
# Find transmission through monitor for future scaling
T_temp = getresult(mname,"T");
T = T_temp.T;

  # loop over each frequency point
  for (fi=1:length(f)) {

    # Find  diffracetd peaks
    E2 = farfieldpolar3d(mname,fi,res,res);
    ux = farfieldux(mname,fi,res,res);
    uy = farfielduy(mname,fi,res,res);
    theta = linspace(-90,90,181);
    phi = linspace(0,90,91);
    Theta = meshgridx(theta,phi);
    Phi = meshgridy(theta,phi);
    Etheta_angle = farfieldspherical(E2(:,:,2),ux,uy,Theta,Phi);
    Etheta_angle = reshape(Etheta_angle, [length(theta), length(phi)]);
    Ephi_angle = farfieldspherical(E2(:,:,3),ux,uy,Theta,Phi);
    Ephi_angle = reshape(Ephi_angle, [length(theta), length(phi)]);



    Ephi_2 = abs(Ephi_angle)^2;
    Etheta_2 = abs(Etheta_angle)^2;
```

```
    E2_spherical = sqrt(Etheta_2 + Ephi_2);
    # At each peak, Find the Jones matrix contribution

    for (p_i=1:length(angles(:,fi))){
        ?angles(p_i,fi);
        jones(1,1,fi,p_i)=Etheta_angle(angles(p_i,fi),1);
        jones(2,1,fi,p_i)=Ephi_angle(angles(p_i,fi),1); }
    }

    #delete previous source if run several times in succession
switchtolayout;
select("plane_wave");
delete;
#Set input to p-polarized (polarization angle = 0)
addplane;
set("name","plane_wave");
set("injection axis","z");
set("direction","forward");
# I think the x and y span should match the fdtd region's xy-plane, or at least cover it
set("x",0);
set("x span",6e-6);
set("y",0);
set("y span",0.5e-6);
set("z",-1e-6);
set("wavelength start",0.6e-6);
set("wavelength stop",1.3e-6);
set("polarization angle",90);
run;
# specify monitor name, get frequency vector
mname="monitor";
f=getdata(mname,"f");
# Find transmission through monitor for future scaling
T_temp = getresult(mname,"T");
T = T_temp.T;


MM = matrix(4,4,length(f),n);
  # loop over each frequency point
  for (fi=1:length(f)) {
```

```
    # Find  diffracetd peaks
    E2 = farfieldpolar3d(mname,fi,res,res);
    ux = farfieldux(mname,fi,res,res);
    uy = farfielduy(mname,fi,res,res);
    theta = linspace(-90,90,181);
    phi = linspace(0,90,91);
    Theta = meshgridx(theta,phi);
    Phi = meshgridy(theta,phi);
    Etheta_angle = farfieldspherical(E2(:,:,2),ux,uy,Theta,Phi);
    Etheta_angle = reshape(Etheta_angle, [length(theta), length(phi)]);
    Ephi_angle = farfieldspherical(E2(:,:,3),ux,uy,Theta,Phi);
    Ephi_angle = reshape(Ephi_angle, [length(theta), length(phi)]);



    Ephi_2 = abs(Ephi_angle)^2;
    Etheta_2 = abs(Etheta_angle)^2;
    E2_spherical = sqrt(Etheta_2 + Ephi_2);
    # At each peak, Find the Jones matrix contribution

    for (p_i=1:length(peaks)){
        jones(2,1,fi,p_i)=Etheta_angle(angles(p_i,fi),1);
        jones(2,2,fi,p_i)=Ephi_angle(angles(p_i,fi),1);

        # Create Mueller Matrix
J = jones(:,:,fi,p_i);
J=pinch(J);
Jstar = ctranspose(J);
#Code for kroenecker product, improve later if neccesary
temp = matrix(4,4);
           temp(1,1)=J(1,1)*Jstar(1,1);
           temp(1,2)=J(1,1)*Jstar(1,2);
           temp(1,3)=J(1,2)*Jstar(1,1);
           temp(1,4)=J(1,2)*Jstar(1,2);
           temp(2,1)=J(1,1)*Jstar(2,1);
           temp(2,2)=J(1,1)*Jstar(2,2);
           temp(2,3)=J(1,2)*Jstar(2,1);
           temp(2,4)=J(1,2)*Jstar(2,2);
           temp(3,1)=J(2,1)*Jstar(1,1);
```

```
            temp(3,2)=J(2,1)*Jstar(1,2);
            temp(3,3)=J(2,2)*Jstar(1,1);
            temp(3,4)=J(2,2)*Jstar(1,2);
            temp(4,1)=J(2,1)*Jstar(2,1);
            temp(4,2)=J(2,1)*Jstar(2,2);
            temp(4,3)=J(2,2)*Jstar(2,1);
            temp(4,4)=J(2,2)*Jstar(2,2);

            MM(:,:,fi,p_i)= mult(A,temp,A_inv);
        }
    }


visualize(jones);

visualize(MM);
?angles;
```

Appendix B - Python script for post-processing and plotting Mueller Matrices

In [ ]:
```
json_file_mueller_matrix_name = "MS1_corrected.json"
json_file_angles_name = "MS1_corrected_angle.json"
json_file_frequencies_name = "MS1_corrected_freq.json"
```

In [ ]:
```
import json
import numpy as np
import matplotlib.pyplot as plt

# Function to read data from a JSON file
def read_json(file_name):
    try:
        with open(file_name, 'r') as json_file:
            data = json.load(json_file)
        return data
    except FileNotFoundError:
        print(f"Error: File '{file_name}' not found.")
        return None
    except Exception as e:
        print(f"Error: {e}")
        return None

# Example usage (replace 'your_data.json' with your actual file name)
json_file_name = json_file_mueller_matrix_name
json_data = read_json(json_file_name)

if json_data is not None:
    # Convert the JSON data into a 4-dimensional NumPy array
    four_dimensional_matrix = np.array(json_data["MM"]["_data"])
    four_dimensional_matrix = four_dimensional_matrix[::2]
    result_matrix = four_dimensional_matrix.reshape(11,141,4,4)
```

In [ ]:
```
normalized_matrix = np.zeros((11,141,4,4))
for i in range(11):
    for j in range(141):
        normalized_matrix[i,j:,:] = result_matrix[i,j,:,:]/result_matrix[i,j,0,0]
```

In [ ]:
```
json_file_name = json_file_angles_name
json_data = read_json(json_file_name)["angles"]["_data"]
result = np.array(json_data).reshape(141,11)
```

In [ ]:

```
import numpy as np

# Define the 2D array with 141 frequency points and 11 angles
freq_points = 141
angles = 11
data = result

# Define lower and upper limits for angles
lower_limit = 73  # Example lower limit
upper_limit = 83  # Example upper limit

# Initialize arrays to store results
valid_angles_indices_lower = [5]
invalid_freq_indices_lower = []
valid_freq_imdices_lower = [0]
angles_lower = [73]
# Loop through each frequency point
for freq_index in range(1,freq_points):
    angle_index = None
    for angle_index in range(angles):
        angle = data[freq_index, angle_index]
        if (lower_limit <= angle <= upper_limit) and (angle>=(angles_lower[-1]-1)):
            valid_angles_indices_lower.append(angle_index)
            valid_freq_imdices_lower.append(freq_index)
            angles_lower.append(angle)
            break
    else:
        invalid_freq_indices_lower.append(freq_index)

# Convert lists to arrays
valid_angles_indices_lower = np.array(valid_angles_indices_lower)
invalid_freq_indices_lower = np.array(invalid_freq_indices_lower)

# Trim the 4D array using invalid_freq_indices
trimmed_four_d_array_lower = np.delete(normalized_matrix, invalid_freq_indices_lower,
trimmed_angles = np.delete(result,invalid_freq_indices_lower,axis=0)
```

In [ ]:
```
import numpy as np

# Define the 2D array with 141 frequency points and 11 angles
freq_points = 141
angles = 11
data = result

# Define lower and upper limits for angles
lower_limit = 99  # Example lower limit
upper_limit = 109  # Example upper limit

# Initialize arrays to store results
valid_angles_indices = [7]
invalid_freq_indices = []
valid_freq_imdices_upper = [0]
angles_upper = [109]

# Loop through each frequency point
for freq_index in range(1,freq_points):
    angle_index = None
    for angle_index in range(angles):
        angle = data[freq_index, angle_index]
        if (lower_limit <= angle <= upper_limit) and (angle<=(angles_upper[-1]+1)):
            valid_angles_indices.append(angle_index)
            angles_upper.append(angle)
            valid_freq_imdices_upper.append(freq_index)
            break
    else:
        invalid_freq_indices.append(freq_index)

# Convert lists to arrays
valid_angles_indices = np.array(valid_angles_indices)
invalid_freq_indices = np.array(invalid_freq_indices)

# Example 4D array
four_d_array =normalized_matrix

trimmed_four_d_array_upper = np.delete(four_d_array, invalid_freq_indices, axis=1)
trimmed_angles = np.delete(result,invalid_freq_indices_lower,axis=0)
```

In [ ]:
```
speed_of_light = 299792458
freq_file_name = json_file_frequencies_name
freq_data = np.array(read_json(freq_file_name)["freq"]["_data"])
freq_lower = np.delete(freq_data,invalid_freq_indices_lower,axis=0)
freq_upper = np.delete(freq_data,invalid_freq_indices,axis=0)
wavelengths_lower = speed_of_light / freq_lower
wavelengths_upper = speed_of_light/freq_upper
```

In [ ]:
```
mm_11 = np.zeros((len(valid_angles_indices_lower),4,4))
mm11 = np.zeros((len(valid_angles_indices),4,4))
for i in range(len(valid_angles_indices_lower)):
    mm_11[i,:,:] = trimmed_four_d_array_lower[valid_angles_indices_lower[i],i,:,:]
for i in range(len(valid_angles_indices)):
    mm11[i,:,:]=trimmed_four_d_array_upper[valid_angles_indices[i],i,:,:]
```

In [ ]:
```
trimmed_data_lower = np.delete(result_matrix, invalid_freq_indices_lower, axis=1)
trimmed_data_upper = np.delete(result_matrix, invalid_freq_indices, axis=1)
```

In [ ]:
```
mm11x = np.zeros((len(valid_angles_indices_lower),4,4))
mm11y = np.zeros((len(valid_angles_indices),4,4))
for i in range(len(valid_angles_indices_lower)):
    mm11x[i,:,:] = trimmed_data_lower[valid_angles_indices_lower[i],i,:,:]
for i in range(len(valid_angles_indices)):
    mm11y[i,:,:]=trimmed_data_upper[valid_angles_indices[i],i,:,:]
```

In [ ]:
```
# Extract the elements matrix[:,0,0]
array = mm11x[:, 0, 0]
array2 = mm11y[:,0,0]
# Normalize the array with respect to the largest entry
max_value = np.max(array)
max_value2 = np.max(array2)
normalized_array = array / max_value
normalized_array2 = array2 / max_value2
```

In [ ]:
```
# Create a 4x4 subplot grid
fig, axs = plt.subplots(4, 4, figsize=(12, 12))
x_data = wavelengths_lower*1e9
x_data2 = wavelengths_upper*1e9
# Iterate through rows and columns to create subplots
for i in range(4):
    for j in range(4):
        if(j==0 and i==0):
            axs[i, j].plot(x_data, normalized_array)
            axs[i, j].plot(x_data2, normalized_array2)
            axs[i, j].set_title(f'mm_{i + 1}{j + 1}')
            axs[i, j].set_xlabel('Wavelength in nm')
            axs[i, j].set_ylabel('Normalised MM')
            axs[i, j].set_ylim([np.minimum(np.min(normalized_array),np.min(normalize
        # Extract normalized data for the current subplot
        else:
            y_data = mm_11[:,i,j]
            y_data2 = mm11[:,i,j]

            # Plot the data
            axs[i, j].plot(x_data, y_data)
            axs[i, j].plot(x_data2, y_data2)
            axs[i, j].set_title(f'mm_{i + 1}{j + 1}')
            axs[i, j].set_xlabel('Wavelength in nm')
            axs[i, j].set_ylabel('Normalised MM')
            axs[i, j].set_ylim([np.minimum(np.min(y_data),np.min(y_data2)),np.maximur

# Adjust layout for better spacing
plt.tight_layout()
fig.legend(['m=1', 'm=-1'], loc='upper right')

# Show the plots
plt.show()
```

In [ ]:

```
# Convert angles to degrees
angles1_deg = [e-91 for e in angles_lower]
angles2_deg = [e-91 for e in angles_upper]

x1 = wavelengths_lower*1e9
x2 = wavelengths_upper*1e9

theoretical_angles1 = [- np.degrees(np.arcsin(e/5e3)) for e in x1]
theoretical_angles2 = [+ np.degrees(np.arcsin(e/5e3)) for e in x2]

# Plotting
plt.figure(figsize=(8, 6))
plt.plot(x1,angles1_deg, label='Simulated angle for m=-1')
plt.plot(x2,angles2_deg, label='Simulated angle for m=1')
plt.plot(x1,theoretical_angles1, label='Theoretical angle for m=-1')
plt.plot(x2,theoretical_angles2, label='Theoretical angle for m=1')
plt.xlabel('Wavelength in nm')
plt.ylabel('Angle (degrees)')
plt.title('Plot of Angles (in Degrees) Against wavelength')
plt.legend()
plt.grid(True)
plt.show()
```

Appendix C - AI declaration

NTNU
Fakultet for naturvitenskap

Declaration of AI aids and -tools

Have any AI-based aids or tools been used in the creation of this report?

[ ] No

[x] Yes

If *yes*: please specify the aid/tool and area of use below.

Text

[X] **Spell checking**. Are parts of the text checked by:
Grammarly, Ginger, Grammarbot, LanguageTool, ProWritingAid, Sapling, Trinka.ai or similar tools?

[X] **Text generation**. Are parts of the text generated by:
ChatGPT, GrammarlyGO, Copy.AI, WordAi, WriteSonic, Jasper, Simplified, Rytr or similar tools?

[ ] **Writing assistance**. Are one or more of the reports ideas or approach suggested by:
ChatGPT, Google Bard, Bing chat, YouChat or similar tools?

If *yes*, use of text aids/tools apply to this report - please specify usage here:

After writing the text myself, parts of the text have been rewritten by ChatGPT, to enhance flow and professional language. The ouput from chatGPT has not been directly copied, but suggested features have been implemented with personal variation by myself.
The thesis is written in Overleaf, which has a spell-checking feature, presumably AI powered.

Codes and algorithms

[X] **Programming assistance**. Are parts of the codes/algorithms that i) appear directly in the report or ii) have been used to produce results such as figures, tables or numerical values been generated by: *GitHub Copilot, CodeGPT, Google Codey/Studio Bot, Replit Ghostwriter, Amazon CodeWhisperer, GPT Engineer, ChatGPT, Google Bard* or similar tools?

ChatGPT generated parts of the code for reading json-files and plotting data

If *yes*, use of programming assistance aid/tools apply to this report - please specify usage here:

Images and figures

[ ] **Image generation**. Are one or more of the reports images/figures generated by:
Midjourney, Jasper, WriteSonic, Stability AI, Dall-E or similar tools?

If *yes*, use of image generator aids/tools apply to this report – please specify usage here:

[ ] **Other AI aids or tools**. Have you used other types of AI aids or -tools in the creation of this report?
If yes, please specify usage here:

[x] I am familiar with NTNU's regulations: *Submitting a report generated with the assistance of AI tools and claiming the work to be partially or fully my own, is not permitted. I therefore declare that any use of AI aids or tools are explicitly stated i) directly in the report or ii) in this declaration form.*

Torbjørn Bøyan-Storø 19.02.2024/Trondheim

Signature/Date/Place